

Double Skin Facades Integrating Photovoltaic Panels, Motorized Shades and
Controlled Air Flow

Zissis Ioannidis

A Thesis
in
The Department
of
Building, Civil and Environmental Engineering

Presented in Partial Fulfillment of the Requirements
for the Degree of Master of Applied Science (Building Engineering) at
Concordia University
Montréal, Québec, Canada

September 2016

© Zissis Ioannidis 2016

CONCORDIA UNIVERSITY

CONCORDIA UNIVERSITY
School of Graduate Studies

This is to certify that this thesis prepared

By: Ioannidis Zissis

Entitled: Double Skin Facades Integrating Photovoltaic Panels, Motorized Shades and Controlled Air Flow

and submitted in partial fulfillment the requirements for the degree of

Master of Applied Science (Building Engineering)

complies with the regulations of the University and meets the accepted standards with respect to originality and quality.

Signed by the final Examining Committee:

Dr. A. Bagchi Chair

Dr. M. Paraschivoiu Examiner
External (to program)

Dr. L. Wang Examiner

Dr. A. Athienitis Supervisor

Dr. T. Stathopoulos Supervisor

Approved by _____
Chair of Department or Graduate Program Director

Dean of Faculty

Date _____

Abstract

A Double Skin Façade (DSF) with photovoltaic panels and automated roller shading devices aims at the reduction of the energy consumption of the building and at the on-site generation of electricity while allowing for the possibility of admitting ventilation air from outside without the direct noise and wind-induced direct inflow from open windows.

A detailed transient finite difference model has been developed aiming at analyzing the thermal and electrical performance of an innovative DSF integrating photovoltaics and roller blinds (DSF-P). The model takes into account the effects of wind and the daylight provisions to the adjacent zone of the DSF-P. The energy balance of the system is described by a thermal network and a nodal flow network capable of assessing the wind effects on the cavity along with a daylighting model. In the modeling of the DSF-P the thermal behavior of an adjacent perimeter zone as well as the shading that the photovoltaics and the roller blind provide to the interior skin of the building are also simulated.

The model developed was used for the numerical investigation of various flow rates and shading configurations for a south facing three-storey double skin façade considering a typical year in Montreal (Canada). Different flow rates inside the cavity and shading configurations were considered and simulated. It was concluded that the optimal cavity width, in which the electricity consumption of the DSF-P system is minimized is between 0.2m and 0.6m (0.07 and 0.21 L/H); the electricity generated from the photovoltaics integrated on the exterior skin may cover the total electricity consumption of the adjacent zone; and for some cases an energy positive DSF-P can be generated.

Acknowledgement

Throughout my studies I had the privilege to be surrounded by many exceptional persons who taught me a lot and were always there for me.

First and foremost, I want to thank my parents for being supportive in my decision to pursue a master's degree in another continent. I would also like to thank my brother and my grandmothers for their unconditional love.

I would like to thank my supervisors Prof. Andreas K. Athienitis and Prof. Ted Stathopoulos for giving me the privilege to work with them and for giving me the opportunity to learn more than what is contained in this thesis, thanks to the conferences and workshops I attended. I also want to express my gratitude to my professors for giving me the opportunity to work with many highly educated and motivated scientist.

I want to specially thank Dr. Annamaria Buonomano for her guidance and help, for sharing my frustration and for always coming up with the appropriate solutions. Annamaria was there not only as a supervisor but also as a highly skilled colleague and without her contribution, this thesis would not have been the same.

Working so many hours at the office, I had the opportunity to meet-collaborate and discuss with many interesting people whose assistance and critical view was and still is very appreciative. Thank you Edvinas Bigaila, Yuxiang Chen, Jennifer Date, Vasken Dermadiros, Shahriar Hossain, Olesia Kruglov, Tasos Papachritsou, Stratos Rounis, Ali Saberi, Harry Vallianos, Tingting Yang, Sam Yip, Sophie Yuan. I also want to thank Costa Kapsis because when I was leaving the office I could continue my work from home with his guidance and help.

Finally, I would like to thank my friends and my girlfriend Georgina, who tolerates my passion for what I am doing.

To the memory of my grandparents,

Γιάννη και Ζήση

Contents

Abstract	iii
Acknowledgement	iv
List of Figures	viii
List of Tables	xii
Nomenclature	xiii
1. Introduction.....	1
1.0 Overview	1
1.1 Solar technologies	3
1.2 Double Skin Facades	4
1.3 Main objective.....	6
1.4 Thesis outline	7
2. Literature Review.....	8
2.0 Double Skin Facades	8
2.1 Experimental Studies.....	11
2.2 Modeling of DSFs	13
2.2.1 Flow modeling on DSFs using Computational Fluid Dynamics (CFD).....	16
2.2.2 Flow modeling of DSF using Nodal approaches	18
2.3 Daylighting on DSFs.....	19
2.4 Building Integrated Photovoltaics and Building integrated photovoltaics thermal (BIPV, BIPV/T).....	20
2.4.1 BIPV	20
2.4.2 BIPV/T	21
2.5 DSF integrating PV	24
2.6 Conclusion.....	28
3. DSF Integrating Photovoltaics (DSF-P) Modeling.....	30
3.0 Model description.....	30
3.1 Thermal Network	34
3.1.1 Modeling of the Photovoltaics	41
3.1.2 Longwave radiation heat transfer and view factors in the DSF-P	41
3.1.3 Radiosity method inside the cavity	44

3.1.4	Heat transfer coefficients	45
3.2	Shading.....	47
3.2.1	Positioning of the PV on the Exterior Skin.....	47
3.2.2	Transmittance of STPV and Glazing	50
3.2.3	Shading Calculation	51
3.3	Flow Network.....	52
3.4	Daylighting.....	56
3.4.1	Calculation of electricity consumption for lighting	61
3.5	Developed control strategies	62
3.6	Model Validation.....	63
4.	Simulations and Results.....	66
4.0	Introduction	66
4.1	Daily Analysis for a case with and without roller shade.....	67
4.1.1	Case I: Winter day (January 1st) without roller blind ($v=0.5\text{m/s}$).....	67
4.1.2	Case II: Winter day (January 1st) with roller blind ($v=0.5\text{m/s}$).....	68
4.2	Typical weeks for winter and summer	69
4.2.1	Case I: Winter Week (January 27-31)	69
4.2.2	Case II: Summer Week (June 29 to July 2)	71
4.2.3	Wind effects on the DSF-P cavity for Case I: Winter Week (January 27-31).....	72
4.3	Annual Shading Effect.....	76
4.3.1	Annual incident solar radiation on the interior skin.....	77
4.4	Annual Energy Consumption.....	78
4.4.1	Energy consumption by the fans.....	79
4.4.2	Energy Consumption for Lighting	84
4.5	Parametric analysis.....	88
4.6	Energy Balance	92
4.6.1	Energy Balance and Consumption by Parameters	95
5.	Summary and Conclusions	97
5.0	Thesis Summary and Conclusions	97
5.1	Contribution	98
5.2	Future work	99
Appendix A: Specifications about the Heat Pump		106

Appendix B: Temperature and Velocity Profiles.....	108
Appendix C: Shading.....	114
Appendix D: Annual pressure difference and velocity within the cavity.....	119
Appendix E: Daylight.....	124
Appendix F: Electricity consumption for the heating and cooling.....	138

List of Figures

Figure 1.1: Solar facades classification. BIST (building-integrated solar thermal), BIPV, BIPV/T (building-integrated photovoltaic/thermal), TSW (thermal storage wall), SCH (solar chimney), MVF (mechanically ventilated façade), STBIPV, STBIPV/T (semi-transparent building-integrated photovoltaic–thermal) and NVF (naturally ventilated façade) (Quesada et al., 2012a)	2
Figure 1.2: DSF implication in a new office building in Netherlands (Design, n.d.).....	3
Figure 1.3: Classification of DSF (Barbosa and Ip, 2014).....	5
Figure 1.4: Diagram of different function modes of a DSF (Saelens, 2002).....	5
Figure 2.1: The three different operating modes of a DSF tested: (a) external air curtain, (b) preheating mode, (c) exhaust mode. (Larsen et al., 2014a).....	12
Figure 2.2: Vliet test building in Leuven, Belgium (Saelens, 2002).	13
Figure 2.3: View of the office building studied by Gratia and De Herde.....	15
Figure 2.4: (a) Temperature field with blinds, (b) air flow field with blinds at 45 degrees (Ji et al., 2007).	18
Figure 2.5: Architect's original proposal for the refurbishment of the Centre International Rogier (Viljoen et al., 1997).....	19
Figure 2.6: The four different categories of BIPV reviewed: (a) foil products, (b) BIPV tile products, (c) BIPV module products, (d) Solar cell glazing products (Jelle and Breivik, 2012) .	21
Figure 2.7: Schematic of a control volume in the BIPV/T integrated on the Eco Terra (Chen et al., 2010a).....	22
Figure 2.8: Eco Terra demonstration house (Chen et al., 2010a).....	23
Figure 2.9: BIPV/T demonstration project in a Concordia University building in Montreal (Athienitis et al., 2010).....	23
Figure 2.10: Concept schematic for BIPV/T system (Athienitis et al., 2010).....	24
Figure 2.11: (a) sensor location, (b) cavity figure, (c) view of the DSF (Joe et al., 2014).....	25
Figure 2.12: Prototype pleated PV double facade installed in Toulouse, France (Gaillard et al., 2014b).....	26
Figure 2.13: Prototype building envelopes installed on individual houses in Moret sur Loing, France (Gaillard et al., 2014a).....	26
Figure 2.14: The structure of the ventilated PV-DSF system (Peng et al., 2015).....	27
Figure 2.15: Two outdoor test facilities, one with PV façade (left) and one with internal curtain (right) (Han et al., 2013).	28
Figure 3.1: Sketch of the double façade section (one floor).....	32
Figure 3.2: Schematic of a control volume in the DSF-P.....	34

Figure 3.3: A façade schematic indicating the major nodes	35
Figure 3.4: Thermal Network for the control volume that does not have a shading device, having one airflow	36
Figure 3.5: Thermal Network for the control volume that has a shading device, having two airflows	36
Figure 3.6: Velocity profiles inside the channel for blind and porous media for a tilt angle of 0° (Safer et al., 2005).....	37
Figure 3.7: Discretization of typical surface to obtain view factors between them.....	43
Figure 3.8: Obstructed view of the each strip	44
Figure 3.9: Three section façade.....	48
Figure 3.11: The semi-transparent photovoltaics integrated on the exterior skin act as an equivalent overhang.....	49
Figure 3.11: Wind pressure coefficients for 12 wind angles on a DSF (Lou et al., 2012)	54
Figure 3.12: Shadows from the exterior skin to the interior. Fully shade from the opaque and semi-shade from the semi-transparent photovoltaic	55
Figure 3.13: Examples of points chosen to calculate the illuminance on the work plane. (a) three points on the y-direction, (b) three points on the x-direction, (c) three points on the x and y direction.	56
Figure 3.14: Sketch of rectangle perpendicular plates used in the view factor calculation.....	57
Figure 3.15: Strips on the wall of the building used for the view-factors	59
Figure 3.16: Schematic of the distances used to calculate the configuration factors	60
Figure 3.17: Sketch representing the values verified.....	64
Figure 4.1: Schematic of the DSF-P simulated.....	67
Figure 4.2: Temperature at the middle of the cavity of the DSF-P for a winter day for the case without roller blind	68
Figure 4.3: Temperature at the middle of the cavity of the DSF-P for a winter day for the case with roller blind.....	69
Figure 4.4: Simulated temperatures and incident solar radiation for a winter week	70
Figure 4.5: Simulated temperatures and incident solar radiation for a summer week.....	71
Figure 4.6: Wind and cavity velocities for four winter days for 0.50m cavity width.....	73
Figure 4.7: Thermal, wind and mechanical pressure drop within the cavity for the case of L=0.25m for four winter days.....	74
Figure 4.8: Comparison of the mechanical pressure drop for the two cases examined.....	75
Figure 4.9: Comparison of the thermal pressure drop for the two cases examined.....	75
Figure 4.10: Three section façade.....	76
Figure 4.11: Shading of the exterior skin on the interior for a top (a) and a middle floor (b).....	77
Figure 4.12: The shading effects that the different elements integrated on the exterior skin have on the interior one.	78
Figure 4.13: Wind direction and velocity distribution for which the velocity of the air within the cavity reaches the set-point without the assistance of a fan for 0.25m and 0.50m cavity widths	80
Figure 4.14: Electricity consumption by the fans for different cavity widths and velocities for strategy #1	82
Figure 4.15: Electricity consumption by the fans for different cavity widths and velocities for strategy #4.....	83

Figure 4.16: Points for which illuminance levels are calculated and their distance from the window.....	85
Figure 4.17: Average illuminance inside the room for January.....	86
Figure 4.18: Average illuminance inside the room for June.....	86
Figure 4.19: Daylight autonomy at 300lx for all the different shading configurations	87
Figure 4.20: Electricity consumed to light the work plane at 500lux for a year for the different shading configurations	88
Figure 4.21: Electricity consumption of the DSF-P system for different shading configurations for different cavity aspect ratios	89
Figure 4.22: Electricity consumption of the DSF-P system for different velocity set-points for different cavity aspect ratios	90
Figure 4.23: Electricity consumption of the DSF-P system for different cavity aspect ratios with different shading configurations and different velocity set-points.	92
Figure 4.24: Electricity balance of the DSF-P system for different STPV transmittances for different zone areas for a narrow cavity (L=0.25m)	94
Figure 4.25: Electricity balance of the DSF-P system for different STPV transmittances for different zone areas for a narrow cavity (L=0.50m)	95
Figure 4.26: Electricity consumption of the DSF-P and the adjacent room for the case of V=0.5m/s and with 0% shading.....	96
Figure B.1: Temperature at the middle of the cavity of the DSF-P for a winter day for the case without roller blind for V=1.5m/s.....	108
Figure B.2: Temperature at the middle of the cavity of the DSF-P for a winter day for the case with roller blind V=1.5m/s.....	108
Figure B.3: Temperature at the middle of the cavity of the DSF-P for May 1 st for the case without roller blind for V=0.5m/s.....	109
Figure B.4: Temperature at the middle of the cavity of the DSF-P for May 1 st for the case with roller blind for V=0.5m/s	109
Figure B.5: Temperature at the middle of the cavity of the DSF-P for May 1 st for the case without roller blind for V=1.5m/s.....	109
Figure B.6: Temperature at the middle of the cavity of the DSF-P for May 1 st for the case with roller blind for V=1.5m/s	109
Figure B.7: Temperature at the middle of the cavity of the DSF-P for August 1 st for the case without roller blind for V=0.5m/s.....	110
Figure B.8: Temperature at the middle of the cavity of the DSF-P for August 1 st for the case with roller blind for V=0.5m/s	110
Figure B.9: Temperature at the middle of the cavity of the DSF-P for August 1 st for the case without roller blind for V=1.5m/s.....	110
Figure B.10: Temperature at the middle of the cavity of the DSF-P for August 1 st for the case with roller blind for V=1.5m/s.....	110
Figure B.11: Simulated temperatures and incident solar radiation for a spring week	111
Figure B.12: Velocity of the air within the cavity with a set-point of 0.5m/s for the cases of L=0.25m and L=0.50m	112
Figure B.13: Wind and cavity velocities for four summer days for 0.50m cavity widths.....	113
Figure C.1: Different shading configurations examined.....	114

Figure A.14: Shading of the exterior skin on the interior for a top (a) and a middle floor (b) 25%	115
Figure A.15: Shading of the exterior skin on the interior for a top (a) and a middle floor (b) 50%	115
Figure A.16: Shading of the exterior skin on the interior for a top (a) and a middle floor (b) 75%	116
Figure A.17: Shading of the exterior skin on the interior for a top (a) and a middle floor (b) 100%	116
Figure A.18: Incident solar radiation on the interior skin for 25% shading	117
Figure A.19: Incident solar radiation on the interior skin for 50% shading	117
Figure A.20: Incident solar radiation on the interior skin for 75% shading	118
Figure A.21: Incident solar radiation on the interior skin for 100% shading	118
Figure D.1: Pressure difference inside the cavity caused by mechanical and natural means for constant velocity of 0.5m/s	119
Figure D.2: Pressure difference inside the cavity caused by thermal, wind and mechanical means for constant velocity of 0.5m/s	119
Figure D.3: Pressure difference inside the cavity caused by mechanical and natural means for constant velocity of 1.0m/s	120
Figure D.4: Pressure difference inside the cavity caused by thermal, wind and mechanical means for constant velocity of 1.0m/s	120
Figure D.5: Pressure difference inside the cavity caused by mechanical and natural means for constant velocity of 1.5m/s	121
Figure D.6: Pressure difference inside the cavity caused by thermal, wind and mechanical means for constant velocity of 1.5m/s	121
Figure D.7: Velocity of the air inside the cavity set to be 0.5m/s	122
Figure D.8: Velocity of the air inside the cavity set to be 1.0m/s	122
Figure D.9: Velocity of the air inside the cavity set to be 1.0m/s	122
Figure D.10: Exterior convective heat transfer coefficient	123
Figure E.1: Illuminance levels on the work-plane throughout the year (25% shading)	124
Figure E.2: Illuminance levels on the work-plane throughout the year (50% shading)	124
Figure E.3: Illuminance levels on the work-plane throughout the year (75% shading)	124
Figure E.4: Monthly illuminance as a function of the distance from the window (0% shading)	125
Figure E.5: Different levels of daylight autonomy inside the room (25% shading)	126
Figure E.6: Monthly illuminance as a function of the distance from the window (25% shading)	127
Figure E.7: Different levels of daylight autonomy inside the room (25% shading)	128
Figure E.8: Monthly illuminance as a function of the distance from the window (50% shading)	129
Figure E.9: Different levels of daylight autonomy inside the room (50% shading)	130
Figure E.10: Monthly illuminance as a function of the distance from the window (75% shading)	131
Figure E.11: Different levels of daylight autonomy inside the room (75% shading)	132
Figure E.12: Monthly illuminance as a function of the distance from the window (100% shading)	133

Figure E.13: Different levels of daylight autonomy inside the room (100% shading).....	134
Figure F.1: Heating demand per month for different velocities and shading configurations	141
Figure F.2: Heating demand per month for different velocities and shading configurations.....	141

List of Tables

Table 2.1: Fields of studies on DSF.....	10
Table 3.1: Input parameters for the numerical model.....	31
Table 3.2 Available strategies for the use or not of the fan	62
Table 3.3 Available strategies for the roller blind with shading (100%) or without (0%)	63
Table 3.4: Comparison of experimental and predicted temperatures under quasi-state conditions	65
Table 4.1: The number of times and the average wind velocities for witch the velocity of the air within the cavity reaches the set-point without the assistance of a fan for 0.25m and 0.50m cavity widths (m/s)	80
Table 4.2: Maximum and minimum wind velocities for witch the velocity of the air within the cavity reaches the set-point without the assistance of a fan for 0.25m and 0.50m cavity widths (m/s)	81
Table 4.3: Electricity consumption by the fans for different cavity widths and velocities for strategy #1 and strategy #4 and the differences between them (kWh)	83
Table 4.4: Illuminance Categories as described by IESNA.....	84
Table 4.5: Comparison of the energy consumed to artificially light the work-plane between different shading configurations	88
Table 4.6: Equivalency between the cavity width and the aspect ratio for a 2.8m high floor.....	89
Table 4.7: Electricity consumption of the DSF-P and the adjacent room for a year	95
Table A.1: PLR and EER map for the chiller	106
Table A.2: PLR and COP map for the heat pump	107
Table D.1: Interior and exterior pressure coefficients for different wind direction.....	123
Table E.1: The View Factor matrix for the room for a case of 8 control volumes.....	135
Table E.2: Configuration factors for the case of 5 points on the work-plane and 12 strips on the façade. 8 of the strips are above the work-plane level.....	136
Table E.3: The View Factor matrix for the cavity for a case of 12 control volumes and the roller blind extends at 3 of them.....	137
Table F.1: Electricity consumption for the heating of the adjacent zone for every floor	138
Table F.2: Electricity consumption for the cooling of the adjacent zone for every floor.....	138
Table F.3: Electricity consumption for the heating of the adjacent zone per month	139
Table F.4: Electricity consumption for the cooling of the adjacent zone per month.....	139
Table F.5: Difference between the electricity consumed for the heating of the adjacent zone for the different cases examined (%).....	140

Nomenclature

A :	Area (m^2)	r :	distance (m)
C :	thermal capacitance (J/K)	Re :	Reynolds number (-)
C_d :	orifice discharge coefficient (-)	R_{int} :	internal convective resistance (K/W)
C_f :	configuration factors (-)	S :	Total solar beam radiation (W/m^2)
c_p :	specific heat capacity of the air (kJ/kgK)	T :	temperature (K)
C_p :	pressure coefficients (-)	T_m :	average temperature (K)
D :	hydraulic diameter (m)	V :	velocity (m/s)
d :	profile angle ($^\circ$)	W :	width (m)
E :	illuminance (lx)	x :	distance in x direction (m)
F :	view factor (-)	y :	distance in y direction (m)
G :	Gravitational constant ($9.81 m/s^2$)	z :	distance in z direction (m)
h :	heat transfer coefficient (W/m^2K)		
H :	height (m)	Greek Letters	
I :	solar radiation flux (W/m^2)	α :	absorption factor (-)
J :	Radiosity (W/m^2)	α_s :	surface azimuth ($^\circ$)
K :	thermal conductivity (W/mK)	β_{pv} :	photovoltaic module temperature coefficient (-)
K_e :	extinction coefficient of STPV (m^{-1})	β_s :	solar altitude ($^\circ$)
L :	length (m)	ΔP :	Pressure drop (Pa)
m :	strip surface of the side walls (-)	ΔT :	Temperature difference ($^\circ C$)
M :	final luminous exitance matrix (lx)	Δt :	time step (s)
\dot{m} :	mass flow rate (kg/s)	ε :	emissivity (-)
M_o :	initial luminous exitance matrix (lx)	η :	photovoltaic efficiency (-)
n :	Number of subsections (-)	μ :	dynamic viscosity (Ns/m^2)
n_{lamps} :	Luminous efficacy of the lamps (lm/W)	ν :	Air kinematic viscosity (m^2/s)
Nu :	local Nusselt number (-)	ρ :	reflectance matrix (-)
P :	Power (W)	ρ_{air} :	air density (kg/m^3)
\dot{Q} :	thermal load (W)	σ :	Stefan-Boltzmann constant ($5.67 \cdot 10^{-8} W/m^2K^4$)
R :	thermal resistance (K/W)	τ :	transmittance (-)

Subscripts

air :	air of the channel
ca :	cavity
el :	electricity
fl :	floor
g :	glazing
i :	vertical surface
in :	indoor air
int :	internal
j :	horizontal surface
mech :	mechanical
N :	Number of subsections
nat :	natural
OPV :	opaque photovoltaic
out :	ambient
ov :	overhang
rad :	radiation
rol :	roller blind
sky :	sky vault
sp :	spandrel
stc :	standard test conditions
th :	thermal
u :	total number of surfaces inside the room
usp :	upper spandrel

wd :	window
wi :	interior wall section
wl :	wall
wo :	exterior wall section

Abbreviations

BIPV	Building Integrated Photovoltaic
BIPV/T	Building Integrated Photovoltaic/Thermal
BIST	building-integrated solar thermal
CFD	Computational Fluid Dynamics
COP	Coefficient of performance
DSF	Double Skin Façade
DSF-P	DSF Integrating Photovoltaics
HVAC	heating, ventilating, and air conditioning
Mvent	mechanically developed flow
Nvent	naturally developed flow
OPV	opaque photovoltaic
PV	photovoltaic
PV/T	Photovoltaic Thermal
SHCG	solar heat gain coefficient
STPV	semi-transparent photovoltaic
UTC	unglazed transpired collector

Chapter 1

1. Introduction

1.0 Overview

High-rise buildings with large glazing/window areas are becoming more commonplace in modern cities as part of modern building design. Even if high energy performance glazing is used, these buildings, have high energy consumption, caused by high heat losses during the heating season and high solar gains through during the cooling season. These types of glazing usually provide the building with less than half of the insulation that opaque materials could provide but at the same time, appropriate window to wall ratio, increase the useful solar heat gains and daylight transmitted into the building.

Despite the evident turn of the research community towards renewable energies and innovative ways to reduce energy consumption, energy inefficient buildings are still built. Although much work has been performed on ways to design buildings that consume as much energy as they produce, net-zero energy buildings (NZEB), such buildings are still not very common.

Regulations that compel the building sector to take measures towards energy efficient buildings are becoming a reality nowadays through new building codes and standards. This transition towards net-zero energy buildings or near net-zero energy buildings becomes easier to achieve due

to the development of low cost photovoltaic panels that can be integrated in the building envelope. More precisely solar facades, opaque or transparent can integrate some of these technologies capable to co-generate thermal and electrical energy on site such as the building integrated photovoltaics (BIPV) and building integrated photovoltaics/thermal (BIPV/T) systems. Another type of technologies are the semi-transparent photovoltaics (STPV) windows that can allow solar radiation to partly pass through them and at the same time generate electricity.

One example of transparent solar façades that combine the active and passive features is the DSF. A DSF normally consists of an external and an internal skin separated by a cavity that is used as an air channel (Figure 1.2) (Saelens et al., 2003). If designed properly, DSFs can contribute to the reduction of the energy consumption of buildings by interacting with the adjacent zones and the environment.

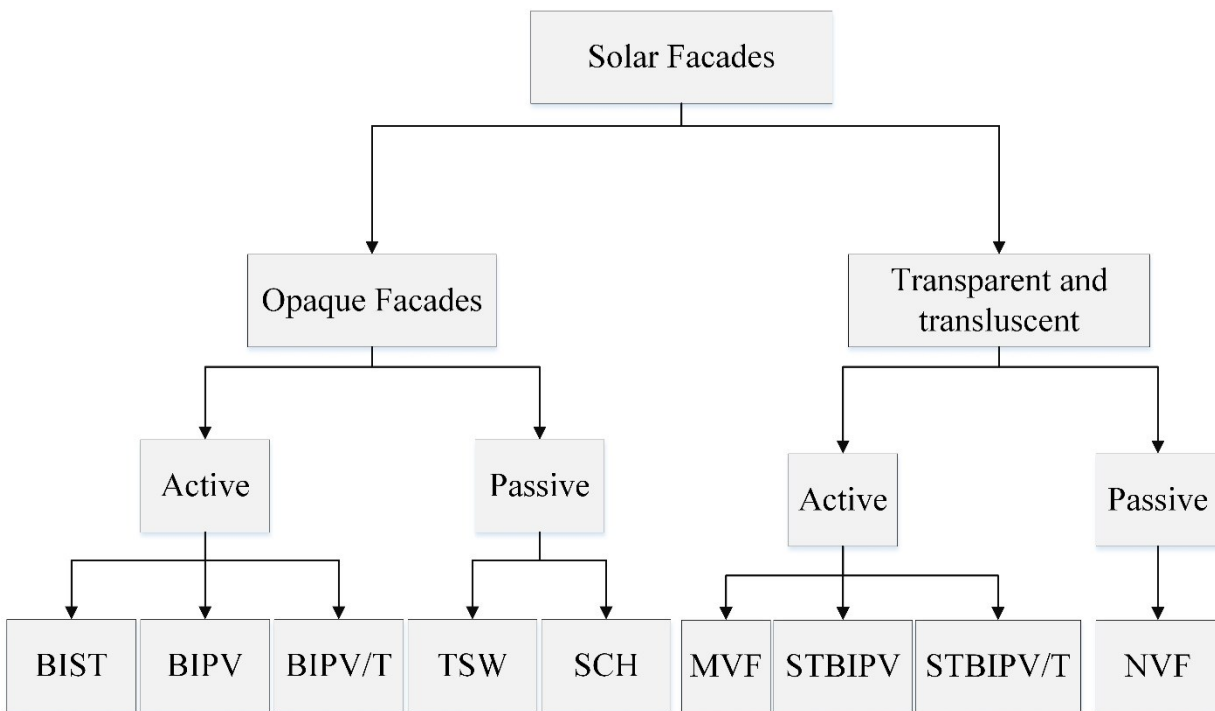


Figure 1.1: Solar facades classification. BIST (building-integrated solar thermal), BIPV, BIPV/T (building-integrated photovoltaic/thermal), TSW (thermal storage wall), SCH (solar chimney), MVF (mechanically ventilated façade), STBIPV, STBIPV/T (semi-transparent building-integrated photovoltaic–thermal) and NVF (naturally ventilated façade) (Quesada et al., 2012a)



Figure 1.2: DSF implication in a new office building in Netherlands
(<https://facadeworld.com/2014/03/15/solarlux-nijverdal/>)

1.1 Solar technologies

Some of the solar technologies that are used in buildings are the different solar thermal collectors (STC). Air or water based solar thermal collectors are being used for many years as a mean to heat the air or the water that is then used for domestic heating.

The rapid drop of the price of the photovoltaics over the last 10 years, led to a significant growth of the photovoltaic industry. Different technologies are presently used in the photovoltaics such as the crystalline silicon cells, the thin film cells and the multi-junction cells. Some of the emerging technologies are the perovskite solar cells, the quantum dots, the organic solar cells and others.

Building integrated photovoltaics are photovoltaics that are used as parts of the buildings, integrating in this way, new technologies to the aesthetics of the building. This integration can be done on the envelope of the building such as the façade or its roof. Another way to incorporate

photovoltaics on the envelope of the building is the integration of semi-transparent photovoltaics (STPV). This can be done with the addition of semi-transparent photovoltaics on the windows or skylights.

A concept that combines building integrated photovoltaics with the solar thermal collectors is the building integrated photovoltaic/thermal (BIPV/T). Integrated on the exterior layer of the building, the photovoltaics generate electricity and the air that passes behind them captures and removes the heat from them. In this way, the photovoltaics are cooled down, their efficiency is increased and at the same time the opportunity to use this preheated air for domestic reasons is given.

1.2 Double Skin Facades

Double skin facades consist of an exterior and an insulated interior skin. Between these two skins a cavity is formed where air can flow according to the desired strategy. This cavity is a buffer zone and in this way, DSF can create a microclimate around the building adding climate resilience to it and assisting it to adapt to ambient temperature fluctuations. Temperature differences inside the cavity can be controlled in order to recover heat from it or facilitate natural ventilation, while the exterior skin can be used to integrate photovoltaics.

Also DSF has significant potential for daylight control and energy savings through the use of controlled louvers or roller shades (Gratia and De Herde, 2007a; Manz, 2004; Saelens et al., 2008). In addition, DSF can improve acoustic comfort, protect the building from wind or rain penetration while it reduces the heating or cooling loads of the building (Gratia and De Herde, 2007b; Quesada et al., 2012b; Shameri et al., 2011). In particular, to avoid rain penetration, one type of DSF, also named rainscreen wall, applies pressure equalization for which airflow and pressures inside the cavity are important (Kala et al., 2008). DSF also provide the opportunity to use operable windows and at the same time extend the usable indoor space area near the window. Furthermore, DSF can be a suitable source for natural or hybrid ventilation for the building (Gratia and De Herde, 2007b).

There are different types of DSF with the most important to be classified as follows:

- a) Box-window: A single storey DSF with one air inlet at the bottom and one air outlet at the top.
- b) Shaft-box double skin façade: A variation of a box façade that extends in multiple floors. Vertical shaft are used to draw the air from the adjacent box-window.

- c) Corridor façade: A single story DSF that is open along the intermediate space between the two skins.
- d) Multi storey double skin façade: The cavity is not separated in either vertical or horizontal way facilitating stack effect and natural ventilation.

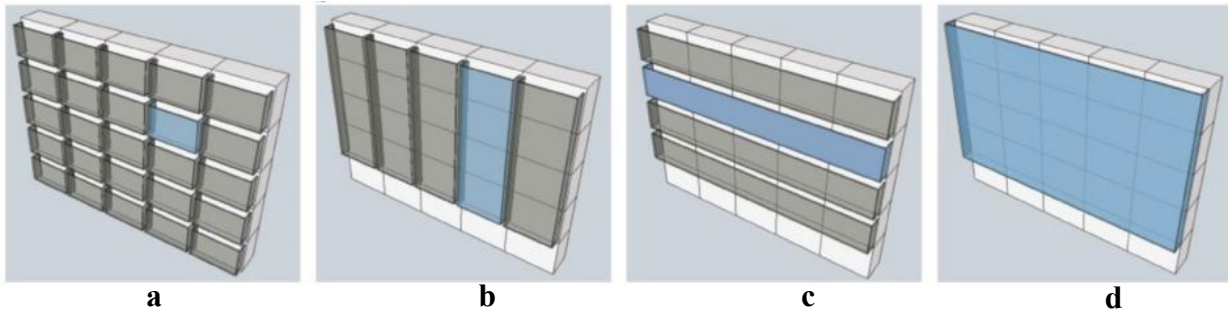


Figure 1.3: Classification of DSF (Barbosa and Ip, 2014)

The basic working modes of DSF are:

- a) Supply: fresh outside air flows inside the building after is preheated inside the cavity.
- b) Exhaust: the warmer air inside the cavity draws the air from the building outside.
- c) Exterior air curtain: naturally ventilated cavity.
- d) Interior air curtain: air from the room is heated at the cavity and then is introduced again to the building.

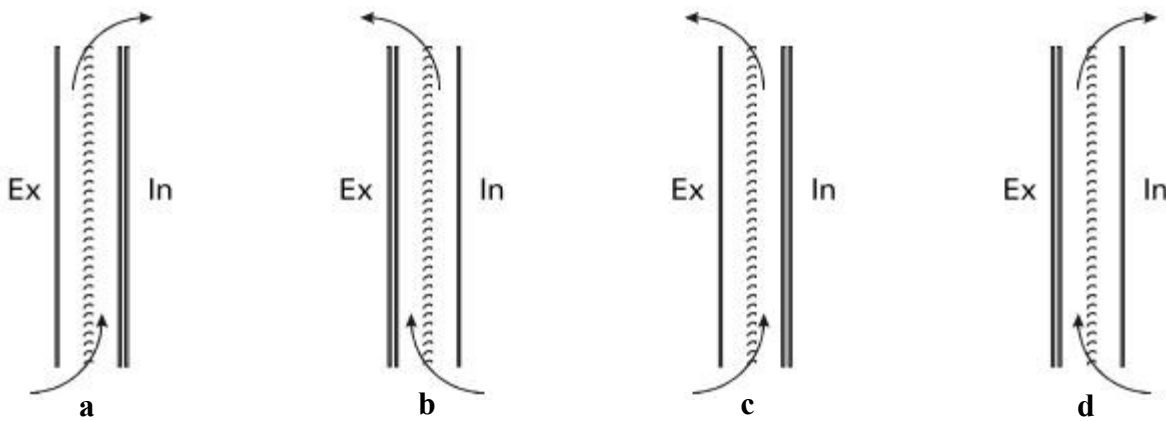


Figure 1.4: Diagram of different function modes of a DSF (Saelens, 2002)

The integration of photovoltaics on the exterior skin, along with the implementation of controlled shading devices in the middle of the cavity of a DSF, gives the opportunity to design an energy positive DSF. This can be achieved by combining three different features of the DSF:

- Electricity generation from the integrated opaque or semi-transparent photovoltaics;
- Solar heat gains and daylight control through the use of shading devices located between the exterior and interior skin of a DSF;
- Extraction of heat from the photovoltaics and the shading device which is recovered by the air flowing inside the cavity.

The creation of a numerical model that is capable to assess the energy and thermal performance of a DSF-P system that combines the simulation of an adjacent zone, along with the daylight and wind effects has not been created yet. A numerical model like that will also help at the optimal design and control of such a technology.

1.3 Main objective

The key research objective of this study is to develop a numerical model that will enable the design of energy positive active building double skin façades that integrate photovoltaic panels. At the same time the DSF-P facade should provide outdoor ventilation air preheated by the facade. This preheated air can also be introduced into the HVAC in order to increase the efficiency of the heat pump used to heat the adjacent zones. Another design objective is to increase the occupants' comfort by avoiding direct noise and wind effects and at the same time to increase the working space close to the window in which the occupants can be without feeling uncomfortable due to drafts and glare. In this way the possibility is given to the occupants to introduce fresh air to the building in high-rise buildings without the noise associated with direct air flow through open windows. DSF-P can be used in newly built buildings or in retrofit projects.

For this reason, the purpose of this study is to create an interactive model capable to describe and simulate the behaviour of a double skin façade integrating photovoltaics and actively controlled shading plus controlled airflow that integrates wind effects. This flexible model can allow the users to simulate many possible configurations of photovoltaics and glazing integrated on the exterior skin and many possible configurations of opaque or transparent elements on the interior skin.

Meteorological data can be input to the model and different geometries can be tested through parametric analyses, as well as different air velocities within the cavity and different semi-transparent photovoltaic transmittances, helping in this way the users to decide which is the appropriate configuration of DSF-P needed for their cases.

This tool will be used by engineers, architects, builders and scientists in order to evaluate the energy performance of a double skin façade integrated with photovoltaics. The advantage would be that a tool like this one could be used for feasibility studies at the early stages of the design of buildings. It also gives the freedom to select the elements of the façades making in this way a helpful tool for retrofit projects.

1.4 Thesis outline

In chapter 2, a literature review of DSFs is presented focusing on the thermal, flow and daylight modeling of DSFs along with their experimental evaluation. Part of this chapter is also the presentation of BIPV and BIPV/T technologies available and the integration of photovoltaics on DSFs. In chapter 3, the development of a mathematical model that describes and simulates the behaviour of a DSF integrating photovoltaics is presented while in chapter 4 a parametric analysis of a DSF integrating photovoltaics and its performance is presented. At the same chapter, the conditions under which net-zero energy performance can be achieved for a perimeter zone is also presented. Finally, chapter 5 summarizes the main findings and conclusions of this study.

Chapter 2

2. Literature Review

2.0 Double Skin Facades

Double Skin Façade is a technology that started to be applied mainly in Europe back in the 80s. Driven by aesthetic and some practical reasons, such as the ability to bring fresh air into the building without strong wind effects and noise, architectural firms applied an additional skin of glazing at the exterior of the buildings (Poirazis, 2007). This unconventional for the time envelope design led many scientists to investigate the performance of the double skin façades and develop strategies to optimize their performance. The cavity that is created between the exterior skin of the building and the interior envelope of the building creates many opportunities for regulating the climate around the building and therefore the energy consumption of the building. These

opportunities needed much investigation and for these reason a great number of scientific studies have been published.

The DSFs have been widely reviewed in the past, concluding that the main research was focused on the ventilation of the DSF, whereas daylighting, have not been extensively studied yet (Shameri et al., 2011). Shameri et al, also answers the question about the cost-effectiveness of a DSF, concluding that is a long lasting structure and creates an eco-friendly office environment that reduces the cost of maintenance and decreases the energy consumption of the building. In this study it is also noted the different names under which DSFs are often encountered in the bibliography; solar façades, climate facades, ventilated or active façades are some of the names used to describe DSFs.

Quesada et al. (2012b) reviews many possible configurations of solar façades, naturally or mechanically ventilated, integrating or not photovoltaic panels. The advantages that the implementation of a DSF have, are presented. The protection provided to the building from the extreme weather phenomena and the high noise levels, along with the reduction of the heating and cooling loads are mentioned as some of the most important advantages of such technology. Concerning semi-transparent photovoltaic technology, it is stated that is yet at its early stages but their building integration can be the future of net-zero energy buildings and thus it should be further reviewed.

From the literature it is also concluded that natural ventilation is the most common means of ventilation in existing DSFs and the most studied and researched field. The need for extensive research, especially on the interior adjacent zone with the DSF is highlighted by Barbosa et al. (2014). According to the author, this will provide the academic community with information about the thermal comfort of the occupants. After reviewing different cases, Barbosa et al. (2014), concluded that narrower cavity depths are preferred in order to enhance the stack effect, but also shading devices implemented within the cavity can contribute in the same direction. Buoyancy force increases if a single glazing is selected to be placed at the exterior skin and if bigger opening areas at the top of the DSF are created. It is also concluded that shaft-box and multi-storey DSFs are most suitable for natural ventilation but in some cases mechanical systems are required to assist the natural ventilation. A review on ventilated façades was held for a climate zone in China (Zhou and Chen, 2010).

Table 2.1 present all different studies on DSF after 1997. Studies are presented in a chronological order so that the trend that the trend of findings can be followed.

More studies are getting published recently involving opaque and semi-transparent photovoltaics, while there are no studies that combine semi-transparent photovoltaics, roller blinds with both natural and mechanical ventilation and the daylighting of interior space.

Table 2.1: Previews studies on DSF

Source	Experimental	Ventilation		Flow		Shading	PV	Daylight
		Natural	Mechanical	CFD	Nodal			
Viljoen et al., 1997								✓
Zöllner et al., 2002	✓		✓					
Gratia and De Herde, 2004a		✓		✓		Blinds		
Safer et al., 2005								
Asfour and Gadi, 2006		✓		✓	✓			
Charron and Athienitis, 2006	✓	✓	✓		✓	✓	OPV	
Ji et al., 2007	✓	✓		✓				
Kim and Song, 2007	✓							✓
Liao et al., 2007	✓	✓	✓	✓			OPV	
Coussirat et al., 2008		✓	✓	✓		Screen		
Saelens et al., 2008	✓	✓	✓			Roller		
Xu and Yang, 2008		✓		✓		Blinds		
Fuliotto et al., 2010	✓	✓	✓	✓				
Gavan et al., 2010	✓		✓			Blinds		
Serra et al., 2010		✓	✓	✓		Blinds		
Lou et al., 2012	✓	✓						
Pasut and De Carli, 2012		✓		✓				
Zeng et al., 2012		✓		✓		Blinds		
Han et al., 2013	✓	✓			✓		STPV	
Joe et al., 2013	✓	✓	✓		✓	Blinds	OPV	
Peng et al., 2013	✓	✓					STPV	
Shameri et al., 2013								✓
Gaillard et al., 2014b	✓	✓			✓		STPV	
Larsen et al., 2014a, 2014b	✓	✓	✓					
Andelkovic et al., 2015	✓	✓				Blinds		
Marques da Silva et al., 2015	✓	✓			✓	Blinds		

2.1 Experimental Studies

Many experimental studies of DSFs have been performed in the past, investigating the improvement of the performance of a DSF by changing its key-parameters, such as, the airflow inside the cavity, the shading device implemented within the cavity and the type of the internal and external glazing. A decoupling method that separates the airflow model from the thermal model is presented, along with the experimental data collected on a full scale test room with DSF (Fuliotto et al., 2010). It is concluded that the mean thermal field could be analyzed in two-dimensions, having a good agreement with a more complex, three-dimensional model.

Naturally-ventilated multi-storey DSFs have also been experimentally researched by Andelkovic et al (2015); an office building in Belgrade, Serbia with a multi-storey DSF was tested taking into account the enthalpy change of the air inside the cavity. It is shown that the airflow in a naturally ventilated DSF cavity is complex and therefore it is difficult to describe. Also, a naturally-ventilated DSF during the cooling season tends to overheat, resulting in higher energy consumption.

A full-scale test facility in Aalborg, Denmark, named “The Cube” was used for experiments, testing three different operating modes of a DSF (Larsen et al., 2014a, 2014b). The first mode is called “external air curtain”, in which the ambient air is introduced to the DSF from the bottom and then is released to the outdoors. “The preheating mode” is the second one, where the air is preheated inside the cavity and then is introduced into the room. The last is the “exhaust mode”, where the hot air inside the cavity assists the natural ventilation of the room, removing the warmer air from it.

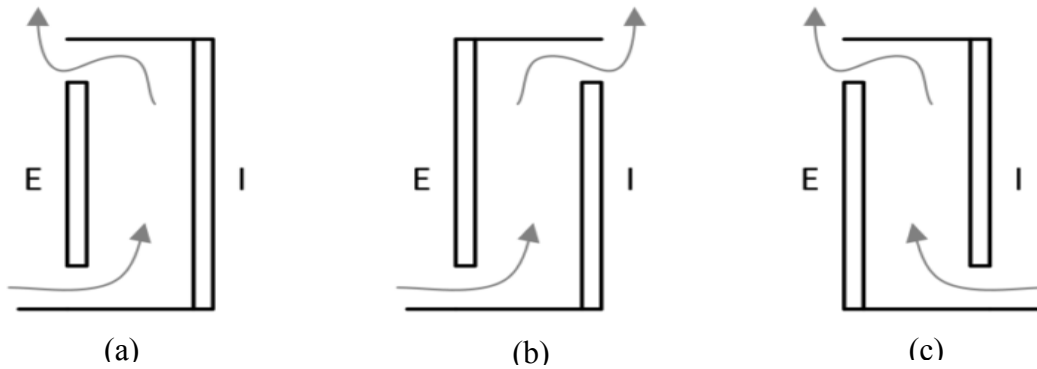


Figure 2.1: The three different operating modes of a DSF tested: (a) external air curtain, (b) preheating mode, (c) exhaust mode. (Larsen et al., 2014a)

The airflow in a naturally ventilated façade is measured and estimated by da Silva et al. (2015). The stochastic nature of the wind is an important parameter to assess the natural airflow inside the cavity, because it might assist or oppose the buoyancy forces. From the experimental results and in order to characterize the DSF behavior, the discharge coefficients were estimated for different angles of the venetian blind implemented within the cavity.

Experimental work was also done in a naturally and mechanically ventilated DSF at the Vliet test building in Leuven, Belgium (Saelens, 2002). Three different systems were examined: a typical cladding system with external shading device (a), a mechanically ventilated double skin façade (b) and a naturally ventilated double skin façade (c). It is concluded that natural ventilation during the cooling season is not preferable because it results into overheating of the DSF. In addition, for the experiments held in Vliet test building in Leuven, Belgium it was observed that during the summer months, the thermal buoyancy caused by the pressure difference between the inlet and the outlet of the DSF drives the airflow inside the cavity. On the contrary, during the winter months, the wind effect is the dominant force in the natural ventilation.



Figure 2.2: Vliet test building in Leuven, Belgium (Saelens, 2002).

Experiments on a mechanical ventilated DSF focusing on the turbulent mixed convection of the air inside the cavity DSF have been held (Zöllner et al., 2002). Average local Nusselt number as a function of the average Archimedes number are presented for different gap widths showing that free convection dominates the flow for the cases examined. Two different models; the channel model and the plate model, explained in this study, should be followed if the cavity widths are smaller and bigger than 0.6m respectively.

The energy efficiency and the thermal comfort performance of a mechanically ventilated DSF was experimentally evaluated at the TWINS (Testing Window Innovative Systems) test facility (Serra et al., 2010). The performance of a DSF is also investigated when the design parameters in a DSF change. Manz et al. (2004) studied the airflow patterns and the thermal behavior of a mechanical ventilated DSF. It is shown that inaccurate results may resolve if piston flows are assumed in a simple model.

Experimental research under controlled climatic conditions have been performed by Gavan et al. (2010). Different airflows and venetian blind angles are examined for a summer case creating a database that will be useful for the validation of numerical models.

2.2 Modeling of DSFs

The façade design, the building and the site parameters are identified to be some of the most important parameters on the performance of the DSF (Barbosa and Ip, 2014). De Gracia et al.

(2013) raised the matter that there is no standard way on reporting results among the researchers and suggested that further research is required to compare all models with the same experimental test. Six groups of models have been used in order to study the performance of DSFs; analytical and lumped models, non-dimensional, network, control volume, zonal approach and computational fluid dynamics (CFD).

In order to analyze the performance of DSFs under different configurations, different simulation software have been used. The TAS software package was used by Gratia and De Herde (2004a) to simulate the natural ventilation in a multi-storey DSF defining the impact that the orientation of the building and the wind direction have on the behavior of the DSF.

More specific the achievement of daytime natural ventilation with the use of a DSF is examined for different wind speeds and orientations (Gratia and De Herde, 2004b). It is easier to apply strategies for natural ventilation if the DSF is placed on the south of the building. Different strategies in order to achieve natural cooling for buildings are examined (Gratia and De Herde, 2004c). For a multi-storey DSF, simulations were realized with TAS software concluding that night ventilation is more effective than day ventilation for middle-sized office buildings with offices aligned on two facades for a summer period in Belgium. The same software was also used for a comparative analysis of a building with and without a DSF (Gratia and De Herde, 2004d). The authors state that energy savings can be observed, even if the air temperature inside the cavity is always some degrees higher than the outside temperature.

The factors that influence the greenhouse effect in DSFs are examined (Gratia and De Herde, 2007c). The impact that the different parameters have on the mean air temperature of the cavity is simulated and it is shown that the greenhouse effect is favorable in south oriented DSF with a clear glazing on the interior façade for Belgian standard days.

Some strategies that should be followed in order to achieve natural day-time ventilation through a DSF are also evaluated by Gratia and De Herde (2007d). The great influence that the position and the color of the shading device implemented within the cavity is simulated using the TAS software and discussed (Gratia and De Herde, 2007a) and the results show that for a sunny summer day (24 July) the mean colored blinds placed at the middle of the cavity is the more efficient shading configuration.

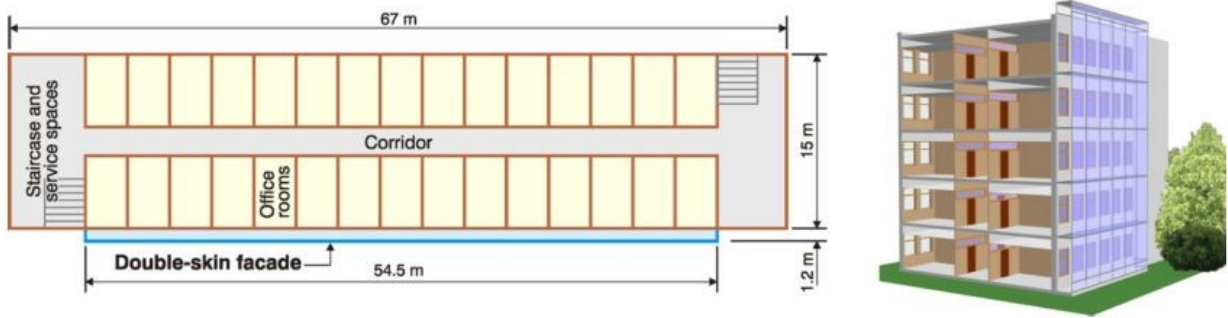


Figure 2.3: View of the office building studied by Gratia and De Herde

The Energy-Plus simulation program is used by Chan et al. (2009) to evaluate the energy performance of a DSF with various glazing types and orientations. Comparing the annual electricity consumption of a building with and without a DSF it is found that cooling savings can be achieved for a year but the author raise his concern about the long payback period of a DSF. In addition, the limitations that Energy plus has when simulating the thermal and the airflow behavior of a DSF are described (Kim and Park, 2011). Although guidelines about what should be considered when simulating DSF with the Energy plus are stated.

Different simulation models are coupled in order to describe the complex physical phenomena encountered on DSFs. The thermal simulation tool TRNSYS is linked with the nodal airflow network COMIS in order to simulate the performance of a DSF for hot and humid climates (Haase et al., 2009). It is highlighted that a careful design of a DSF can have a lot of potentials on the energy efficiency of the building.

A method is demonstrated of how to combine a spectral optical model, a CFD model and a building simulation tool in order to analyze the performance of a DSF (Manz and Frank, 2005). However a full scale experiment has not been performed in order to validate this method.

Other numerical models are developed achieving good agreements with the experimental data. A simple model to study the energy performance of a DSF is presented by Balocco (2002). The physical model created is used to simulate a DSF with different cavity widths, concluding that maximum stack effect can be encountered at cavity widths between 0.2m and 0.3m.

A cell-centered finite volume method describing the performance of a DSF (Saelens, 2002) is used for three different typologies of multi-skin facades, including a DSF (Saelens et al., 2003). It is

underlined that there was no way to improve both the heating and cooling demand with the addition of a DSF and that a sophisticated control mechanism should be applied in order to improve the energy efficiency of the building. The strategies to do that are described in another paper by the same author (Saelens et al., 2008). A single-storey DSF is compared with a traditional window façade with an interior and exterior roller shade. It is shown that the implemented control strategies can improve significantly the heating and cooling demand of the building.

In addition, occupants' preferences are linked with a mathematical model in order to optimize the performance of a DSF (Park, Augenbroe, Messadi, Thitisawat, & Sadegh, 2004). The validated model was proven to be accurate and reliable to perform energy, comfort and lighting design studies.

Furthermore, several papers are published assessing the energy performance of double skin facades with integrated thermal mass. Phase change materials (PCM) are implemented in a DSF, testing its performance (de Gracia et al., 2015). During the heating season, a DSF integrating PCM presents a lot of potential about lowering the energy consumption of the building, in the contrary to the cooling season in which a lot of benefits were not reported. For this reason a numerical model is created in order to accomplish the system to operate for cooling purposes.

Concrete thermal mass configurations for natural and mechanical ventilations were developed in an effort to study the integration of thermal mass within a DSF (Fallahi et al., 2010). The simulations showed the integrated thermal mass in a mechanically-ventilated DSF can increase the savings for both heating and cooling.

2.2.1 Flow modeling on DSFs using Computational Fluid Dynamics (CFD)

The majority of the studies, focus on the airflow inside the cavity and perform computational fluid dynamics (CFD) analysis. CFD tools are used to predict the airflow and the temperature inside the DSF (Pasut and De Carli, 2012). A discussion about which factors increase model complexity without improving the accuracy of the model is presented, concluding that the k- ϵ RNG model should be preferred and that detailed ambient modeling improves significantly the accuracy of the simulation. The same conclusion is drawn by Coussirat et al (2008) where CFD simulations of free and forced convection are performed showing that k- ϵ RNG model yields the smallest errors for all cases examined

In most cases, CFD simulations are held in order to characterize the airflow around the shading devices implemented inside the DSF. The most studied shading device implemented on a DSF is the venetian blinds. CFD modelling is used to investigate the airflow and heat transfer in a DSF equipped with this type of shading device (Safer et al., 2005).

A parametric analysis is presented, changing the position of the blinds, their slat tilt angle and the position of the air outlet of the DSF. It is found that the slat tilt angle has only a small influence on the airflow. The same is stated by Ji et al (2007). The two-dimensional model which investigates the coupled convective, conductive and radiative heat transfer coefficient within a DSF cavity, shows that the venetian blinds enhance the natural convection airflow.

Another study that comprises an optical model with CFD and a heat balance model is presented by Xu and Yang (2008). In this case, a reliable tool to analyze natural ventilation in a DSF with venetian blinds was validated with experimental data.

A CFD method utilizing a porous media model was presented in order to simulate natural ventilation on a DSF implemented with venetian blinds (Zeng et al., 2012). The computational time saved using this method is notable. Good agreement between the measured and the simulated results has been found.

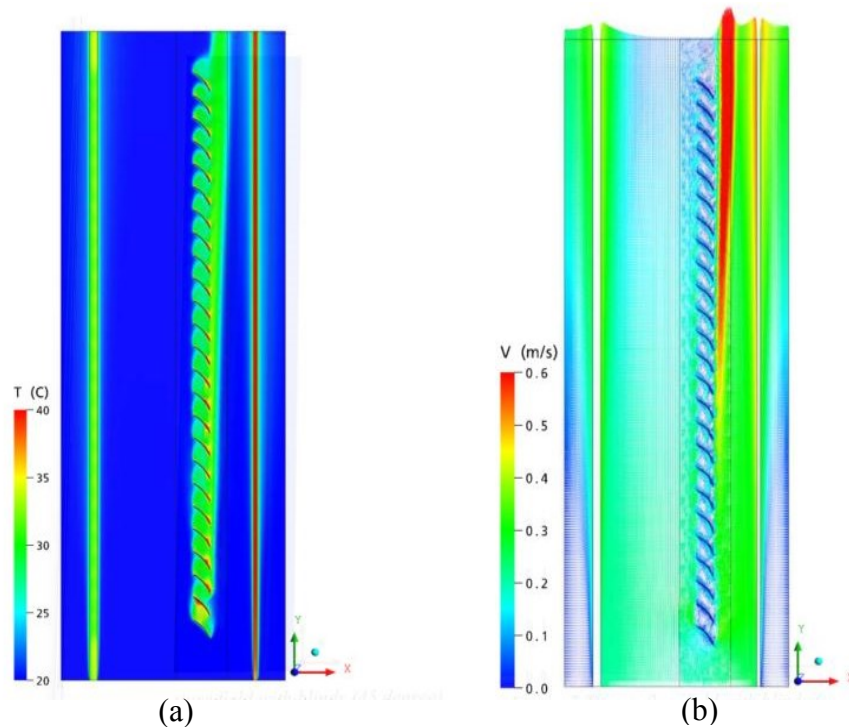


Figure 2.4: (a) Temperature field with blinds, (b) air flow field with blinds at 45 degrees (Ji et al., 2007).

2.2.2 Flow modeling of DSF using Nodal approaches

Apart from computational fluid dynamics, nodal flow networks have been used to model the flow inside closed cavities. The pressure drop between different points of the cavities is connected with the velocity of the air between these points, using the Bernoulli equation, the orifice equation and other empirical relationships.

A comparison between CFD and network model results for the estimation of airflow rates in buildings was presented (Asfour and Gadi, 2006). The predicted and simulated airflow rates are compared and suggested to use as a validation method.

The possibility of integrating trickle ventilators at office buildings is studied through air flow network simulations (Karava et al., 2003). Also a full scale experimental investigation of trickle ventilators has examined the validity of the orifice equation for two types of ventilators and showed

that pressure controlled ventilators have generally superior performance in comparison to slot ventilators.

An airflow zonal model for DSFs is developed and validated with wind-tunnel experiments (Lou et al., 2012). For different DSF widths and lengths, the wind pressure distribution is investigated. It was concluded that the zonal approach is an accurate tool and a good alternative of wind tunnel experiments and CFD analysis, in order to investigate the performance of DSF in tall buildings.

2.3 Daylighting on DSFs

The daylight characteristics of buildings with integrated DSFs have not been extensively reviewed yet. RADIANCE computer modelling package along with scale-model measurements are used to analyze a building in Brussels with two DSF, one on the west and one on the east side of the building (Viljoen et al., 1997).

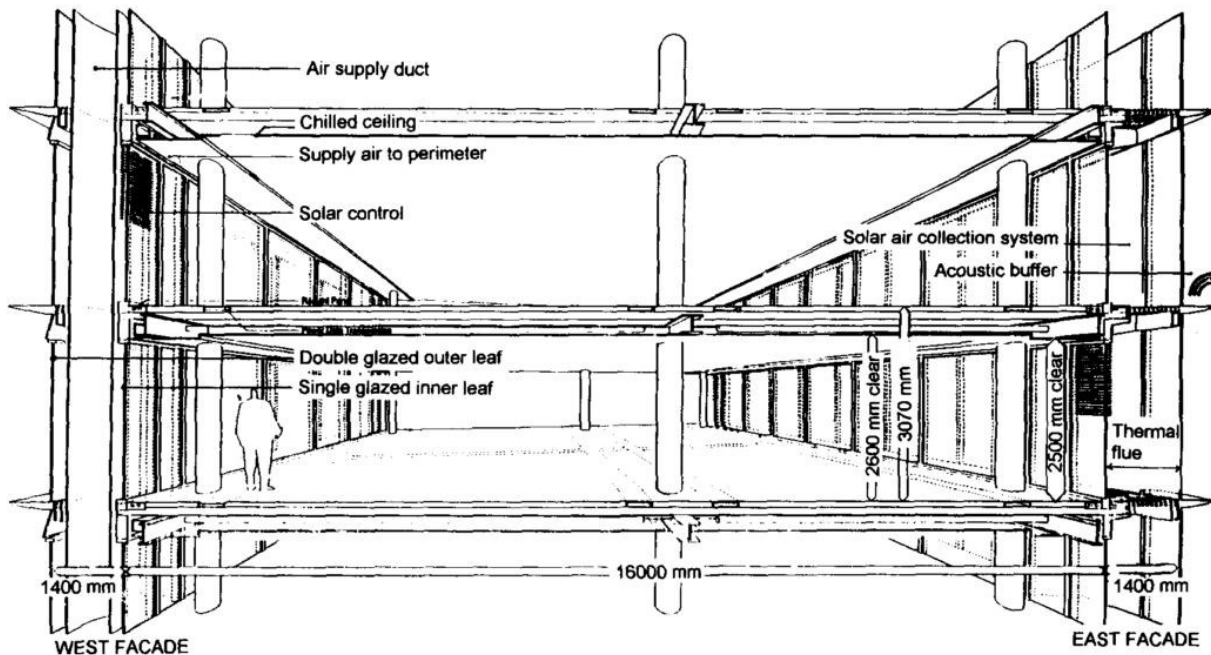


Figure 2.5: Architect's original proposal for the refurbishment of the Centre International Rogier (Viljoen et al., 1997)

A responsive to daylight dimming control system is analyzed in an office building with DSFs (Kim and Song, 2007). For both north and south facing DSFs, computer simulations are performed for different shading device configurations. The photo-sensor signals and work-plane illuminance are

paired together with linear prediction models. However, but it was stated that depending on the type of photo-sensor, the models present different accuracy.

IES simulation software was used to evaluate 12 existing DSFs exposed to different climatic conditions (Shameri et al., 2013). It was found that all models failed to meet the illuminance level requirement for the 75% of the space area and that these 12 DSFs did not follow daylight strategies.

2.4 Building Integrated Photovoltaics and Building integrated photovoltaics thermal (BIPV, BIPV/T)

2.4.1 BIPV

Driven by the need to integrate photovoltaic panels on the architectural design of the building, BIPV are getting more and more into becoming an architectural element of the building. Towards the direction of net-zero or near-net zero energy buildings, BIPV are used. By replacing parts of conventional buildings, photovoltaics become part of the active envelope of buildings, by being mounted on roofs or façades (Jelle and Breivik, 2012).

Four different categories of BIPV products or systems have been reviewed:

- BIPV foil products
- BIPV tile products
- BIPV module products
- Solar cell glazing products

All these new and innovative products become common nowadays, in an effort to reduce the energy consumption of buildings.

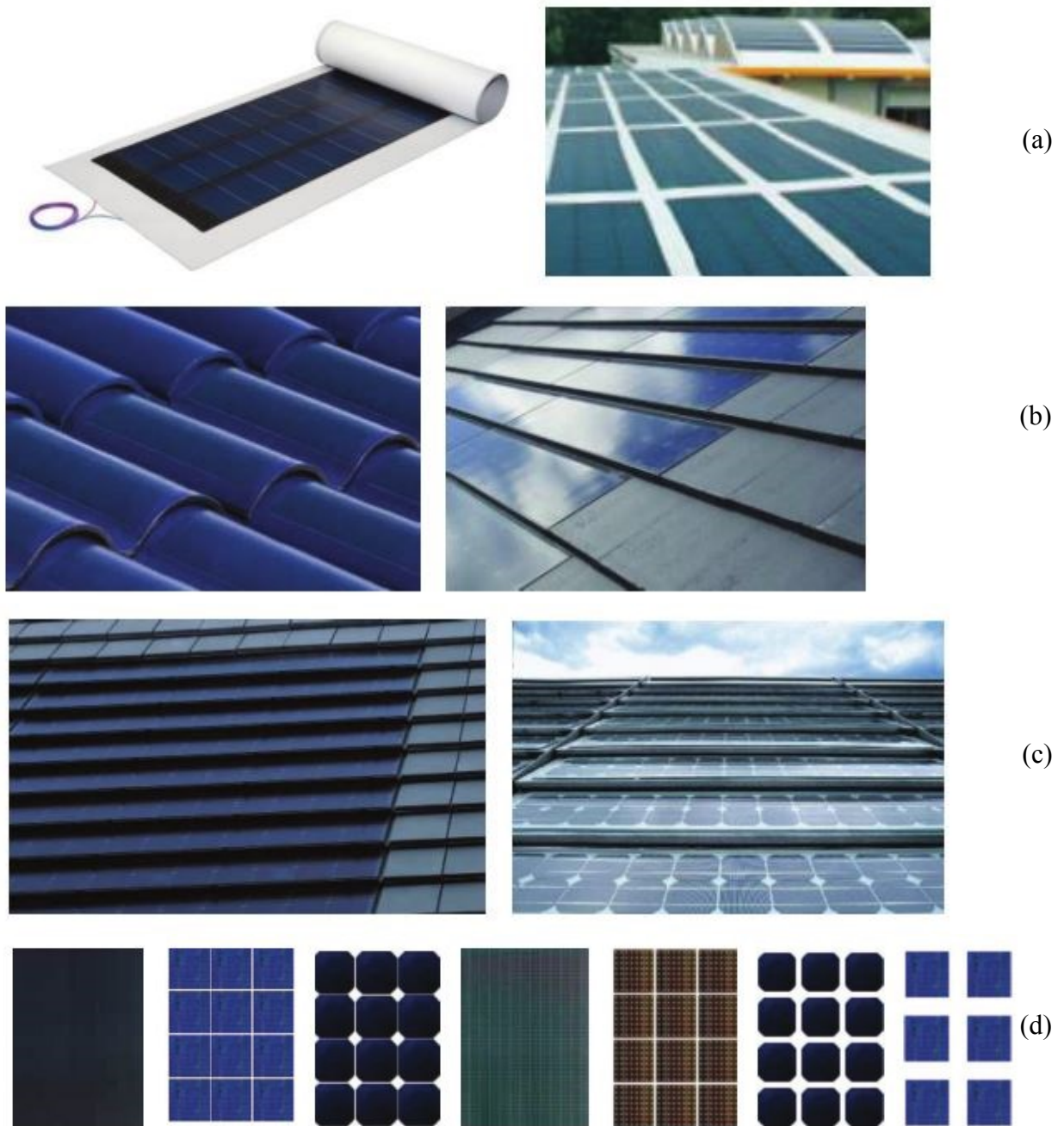


Figure 2.6: The four different categories of BIPV reviewed: (a)Foil products, (b) BIPV tile products, (c) BIPV module products, (d) Solar cell glazing products (Jelle and Breivik, 2012)

2.4.2 BIPV/T

Building Integrated Photovoltaic/ Thermal (BIPV/T) is an emerging technology, combining electricity production, heat production and the integration of photovoltaics on the architectural

design of the building. BIPV/T consist of a photovoltaic panel integrated at the exterior of the building envelope, creating a small cavity between the photovoltaic and the envelope of the building. In this way the air that flows inside this cavity removes heat from the photovoltaic, cooling it down. This serves the system in two ways:

- Increases the efficiency of the photovoltaics, which is sensitive to the increase of their temperature.
- Preheats the air that can be introduced in the HVAC system, thus reducing the energy consumption of the building.

An air-based open-loop BIPV/T system installed in a near net-zero energy building in Quebec (Canada) was extensively studied (Chen et al., 2010a, 2010b) (Figure 2.7). An explicit finite difference model with the use of control volumes was used to simulate the BIPV/T performance (Figure 2.8). It is concluded that BIPV/T systems may reduce the energy consumption of the building significantly.



Figure 2.7: Eco Terra demonstration house (Chen et al., 2010a)

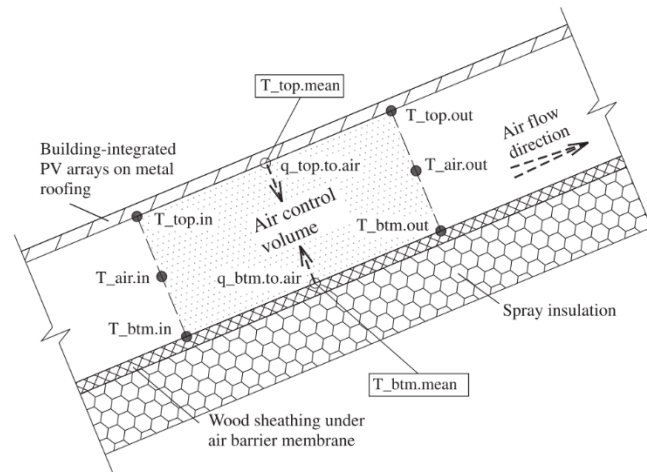


Figure 2.8: Schematic of a control volume in the BIPV/T (Chen et al., 2010a)

A prototype hybrid BIPV/T system is presented by Athienitis et al. (2010) (Figure 2.9 and 2.10). This prototype is constructed with the 70% of the unglazed transpired collector (UTC) covered with photovoltaics modules. Taking into consideration that electric energy is approximately four times more important than heat, it is concluded that this prototype system can generate up to 17% more energy than a typical UTC.



Figure 2.9: BIPV/T demonstration project in a Concordia University building in Montreal (Athienitis et al., 2010)

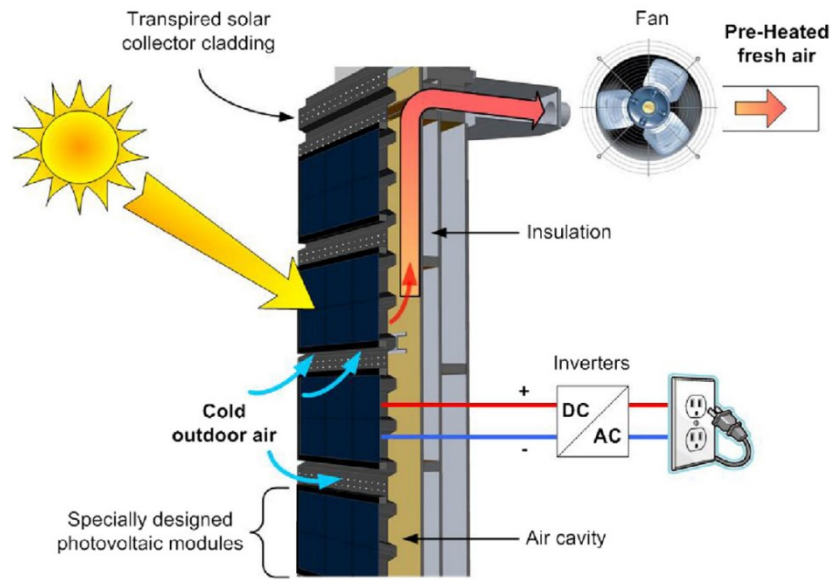


Figure 2.10: Concept schematic for BIPV/T system (Athienitis et al., 2010)

2.5 DSF integrating PV

Although, DSFs and BIPV/T are fields extensively reviewed in the past, DSFs that integrate Photovoltaics/Thermal is a field that has not been studied in detail yet. The heat transfer phenomena in an airflow window with BIPV/T were extensively studied (Liao et al., 2007). A two-dimensional CFD model with k- ϵ model is used to simulate the turbulent flow inside the cavity and correlations of heat transfer coefficients are generated in order to simulate BIPV/T and DSF with a numerical model.

The electrical, thermal and daylight performance of a DSF with integrated opaque photovoltaics and motorized blinds is optimized (Charron and Athienitis, 2006). Integrating the photovoltaics in the middle of the cavity, the combined thermal and electrical efficiency of the system can increase up to 25% and the average annual efficiency of the optimal configuration can reach 55%.

The behavior of a naturally ventilated multi-storey DSF integrating opaque photovoltaics is studied by Joe et al. (2013). This DSF integrated photovoltaics can be seen in Figure 2.11 along with the sensor location within the cavity. The simulation model was verified and different operation strategies were applied. The model showed a reduction to the heating energy consumption, when

the strategies are applied, in comparison to a DSF that is working without them. Subsequently a parametric analysis changing the window glazing and the cavity width was carried out suggesting that a good initial design can result into a further energy reduction (Joe et al., 2014).

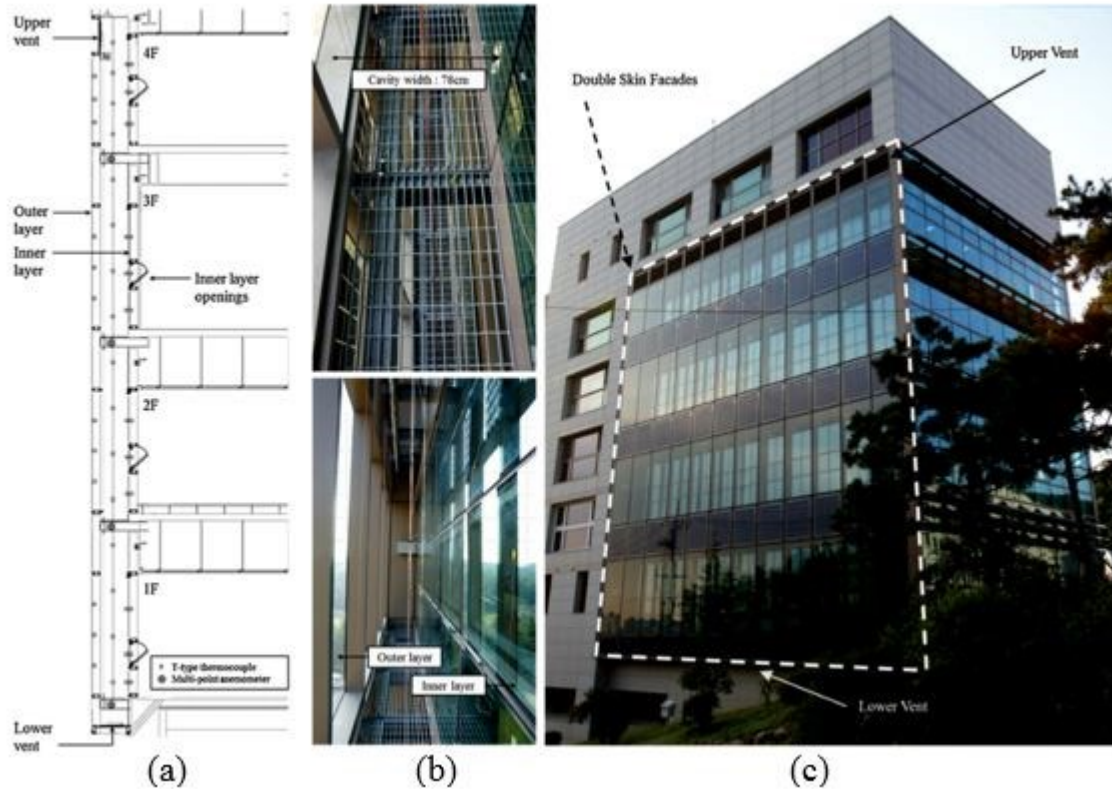


Figure 2.11: (a) sensor location, (b) cavity figure, (c) view of the DSF (Joe et al., 2014)

Three prototype DSFs integrating semi-transparent photovoltaics are tested and a comparison between the thermal response of the semi-transparent photovoltaics and the air inside the cavity is presented (Gaillard et al., 2014b) (Figure 2.12). The two-storey West North-West DSF of the building is designed in this way to increase the electrical performance of the semi-transparent photovoltaics installed by utilizing the stack effect (Gaillard et al., 2014a) (Figure 2.13). As reported by the experimental data collected under real conditions, in a span of a year, the behavior of the system can be predicted by using simple relationships.

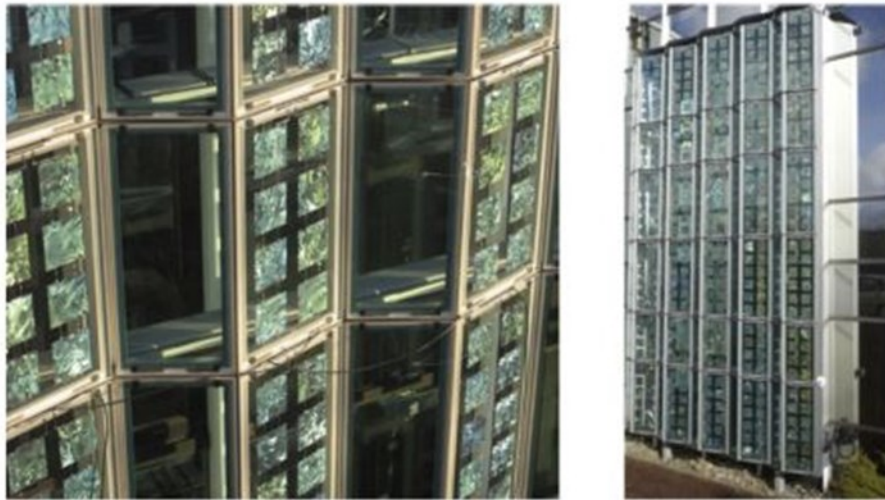


Figure 2.12: Prototype pleated PV double facade installed in Toulouse, France (Gaillard et al., 2014b)



Figure 2.13: Prototype building envelopes installed on individual houses in Moret sur Loing, France (Gaillard et al., 2014a)

An experimental set-up of a DSF integrated with see-through amorphous silicon (a-Si) photovoltaics is tested (Peng et al., 2013). The mechanical ventilation of the DSF can remove the excessive heat from the photovoltaics increasing in this way their efficiency. It is reported that the mechanically-ventilated DSF has the lowest solar heat gain coefficient, in comparison to the non-

ventilated one, where the heat loss was reduced. Different ventilation modes were examined in order to assess the thermal and power performance of this novel DSF integrating photovoltaics (Peng et al., 2015). The experimental set-up used for this study can be seen in Figure 2.14. It is concluded that a DSF integrated with photovoltaics acts as a buffer zone and thus reduces the heat losses of the building during the heating season, and a mechanical ventilated cavity reduces the solar heat gains. Also it stated that the lower operating temperatures result into an increase in the electric power production of the photovoltaics that can reach up to 3%.

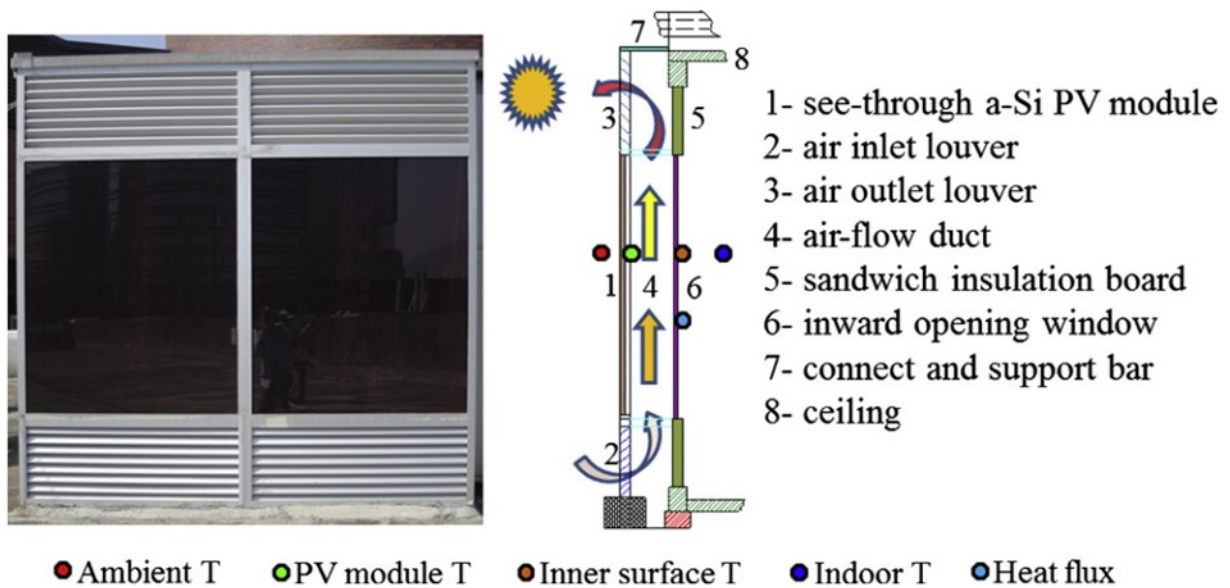


Figure 2.14: The structure of the ventilated PV-DSF system (Peng et al., 2015)

A comparison of a conventional clear glass DSF with a photovoltaic integrated DSF is performed by Han et al. (2013). The experimental set-up of a clear glass DSF and a DSF integrating photovoltaics can be seen in Figure 2.15. The ventilation inside the cavity can reduce substantially the possibility of overheating and at the same time increase the electricity production. It is also highlighted that a DSF integrating photovoltaics can provide better thermal comfort for the occupants.



Figure 2.15: Two outdoor test facilities, one with PV façade (left) and one with internal curtain (right) (Han et al., 2013).

2.6 Conclusion

In this regard, in order to assess the effects of DSF on building energy consumption and comfort, different mathematical models are coupled to building energy and airflow models or specific simulation software (Blanco et al., 2016; Gratia and De Herde, 2004a; Mei et al., 2003). Although such software are often proved to be a good choice between simulation accuracy and simulation time (Anđelković et al., 2016), a lack of whole building simulation tools including advanced DSF is highlighted, along with the need of models which are flexible with respect to the development of suitable operation strategies and the implementation of specific mathematical models (Elarga et al., 2016; Flores Larsen et al., 2015). Such tools could be adopted by building designers and researchers for detailed and rapid numerical analyses on advanced DSFs, especially during the design phase of NZEBs (Athienitis and O'Brien, 2015). Another aspect that is poorly reviewed is the daylighting in double skin facades, particularly when combined with semi-transparent

photovoltaics. In addition, the existence of DSF integrating photovoltaic panels and roller shading devices have not be studied and especially the shading that they provide to the interior skin of the DSF-P. Lastly, a parametric analysis for different DSF-P configurations have not been held in order to optimize such a technology.

For this reason a mathematical model is developed in order to analyze the design of DSF-P with integrated roller blinds. Capable to assess the electrical, thermal and visual performance of the DSF-P the developed model aims to study different operation strategies and to perform parametric analyses. The main design parameters that have not been examined are the cavity with of the DSF, the transmittance of the shading devices and the semi-transparent photovoltaics and the velocities within the cavity.

Chapter 3

3. DSF Integrating Photovoltaics (DSF-P) Modeling

3.0 Model description

A numerical model of a Double Skin Façade integrating Photovoltaic panels (DSF-P) was developed based on a detailed transient finite difference thermal network.

The model can simulate opaque or semi-transparent photovoltaics integrated on the exterior layer of the double skin façade as well as shading devices inside the cavity including the shading that they provide to the building (Figure 3.1). It is also capable to assess the active and passive effects of the generic DSF-P on the thermal and visual comfort and energy performance of the building in which the system is integrated.

The model also allows the users to perform a parametric analysis changing the design parameters of the building and of the DSF-P to be simulated. Specifically, the user can select the location of the building, load the relevant weather file, and decide on the orientation in which the DSF-P will be placed. The user may also select the dimensions of the adjacent to the DSF-P room and the

distance between the two skins of the DSF-P. What can also be adjusted by the user is the existence or not of opaque and semi-transparent photovoltaics, their location on the exterior skin and their dimensions. This also applies to the glazing and the insulation at the interior skin.

The characteristics of the skins can also be determined by defining the height and the insulating values of the spandrel, the upper spandrel, their absorbance and emissivity. The efficiency of the photovoltaics integrated on the exterior skin defined under standard test conditions can be determined by the user, as well as their transmittance. The model is also capable to determine the appropriate position of the photovoltaics to be integrated on the exterior skin, in order to provide shading to the interior of the building. In addition, although the integrated photovoltaics provide shading to the building, the model is ready to simulate the existence of a roller blind within the cavity. The height of the blind, and its thermal and optical properties can also be defined by the user.

Taking into consideration the temperature distribution of the air inside the cavity, as well as the wind velocities and directions imported from the weather file, the airflow inside the cavity can be determined by the model. It is also possible to manually set a desired airflow rate inside the cavity, enabling in this way a mechanical ventilation assisting the stack and wind effects.

The model parameters that can be set by the user are summarized in Table 3.1.

Table 3.1: Input parameters for the numerical model

Design parameters	Number of floors		Optical properties	STPV transmittance
	Position of PV			Roller shade transmittance
	Position of roller blind			Glazing transmittance
	Interior skin design			PV efficiency
Geometric parameters	H_{OPV}/H	H_{sp}/H	Thermal properties	Roller emissivity
	H_g/H	H_{wd}/H		Glazing emissivity
	H_{STPV}/H	H_{usp}/H		SHCG
	L_{ca}/H	H_{rol}/H_g		Insulation of the room
	W	H		COP of the heat pump
Site properties	Location of the building		Flow properties	Reynolds number
	Orientation of the DSF-P			Velocity

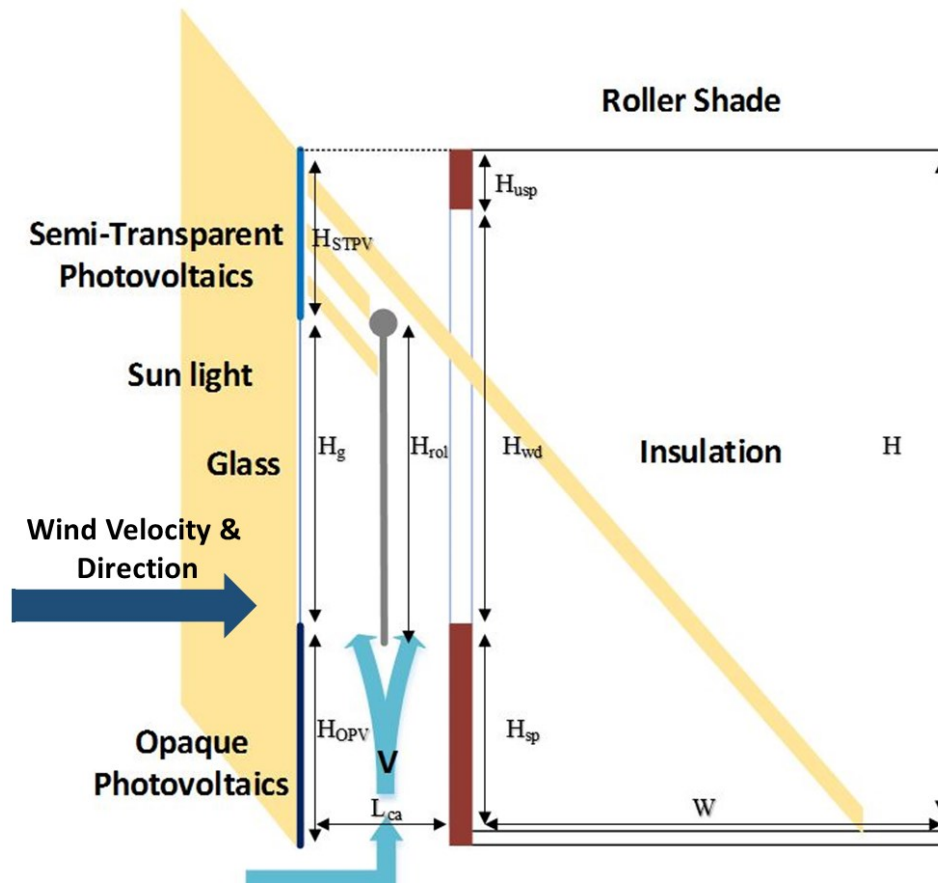


Figure 3.1: Sketch of the double façade section (one floor)

DSFs interactive nature of the model and the flexibility that it provides to the user gives the opportunity to be used for pre-feasibility studies. Engineers, architects and builders can take advantage of this model in the early stages of the design of a building or in the decision making process of retrofit projects, allowing the integration of BIPV/T technologies in new or retrofitted building facades.

The integrated with photovoltaics take full advantage of the cavity and especially of the air flow inside the cavity, serving the system in three ways:

- i) The cavity during the heating season acts as a thermal buffer zone for the building.
- ii) The air flow absorbs the heat from the integrated photovoltaics through convection and thus increases their electrical efficiency.

- iii) Utilizes the preheated air as a source for natural or hybrid ventilation (heating or cooling) for the building.

In addition, if the air at the top of the cavity is warmer than the outdoors, can be introduced to the HVAC system. In this way the energy consumption to heat the air of the adjacent room is decreased.

Also the air inside the cavity can be introduced directly in the interior of the building if the temperature of the air does not exceed the comfort levels of the occupants. Energy conservation can also be achieved by providing natural ventilation to the building or naturally heating and cooling the interior zone, if the DSF acts as a solar chimney.

The modelled cavity could also include automated roller shades, which help to reduce the space cooling and heating loads and control the daylight levels in the indoor space.

Air can flow on both sides of the shading devices placed within the cavity, extracting more heat from them and increasing the thermal efficiency of the system (Figure 3.1).

In this study an interactive numerical model for the assessment of the energy performance of a multi-storey Double Skin Façade integrating photovoltaics (DSF-P) has been implemented in MatLab (Mathworks). The whole exterior, and, similarly, the interior skin of a multi-storey building are designed as multiple strips made of semi-transparent photovoltaics, glazing, and opaque photovoltaic elements. Control volumes are formed between the strips on the exterior skin and those on the interior.

The mass entering the control volume is equal to the mass leaving the control volume and in the case of steady state and in the absence of work and heat transfer, the energy within the control volume remains constant (Figure 3.2).

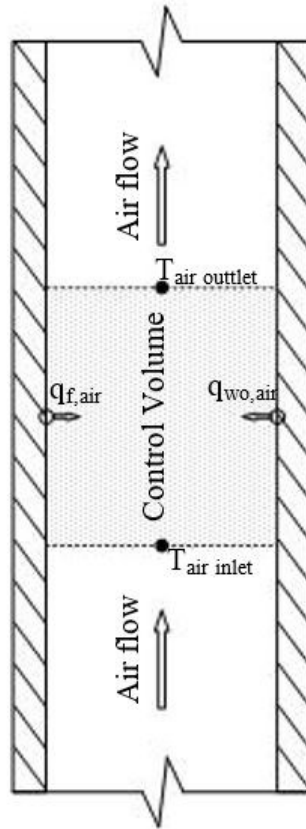


Figure 3.2: Schematic of a control volume in the DSF-P

3.1 Thermal Network

The simulation model of the DSF-P takes into account the heat transfer processes, utilizes a nodal approach and numerical solving processes. The temperature nodes used can be seen on Figure 3.3. A two-dimensional transient model is used to solve two sets of explicit finite difference equations, obtained for each node of the adopted thermal network, showing the conductive, radiative and convective heat transfers in the DSF-P system. These two sets of equations are due to the fact that the roller blind is implemented at the middle of the cavity. One set of equations is used in the case where there is not a roller blind, taking into consideration only one airflow inside the cavity (Figure 3.4) and another when the roller splits the cavity into two smaller cavities. This results into two airflows one in front of the roller and one behind it (Figure 3.5). The thermal storage of the air nodes inside the cavity is assumed to be negligible, the same is for the glazing, the photovoltaics and the insulation.

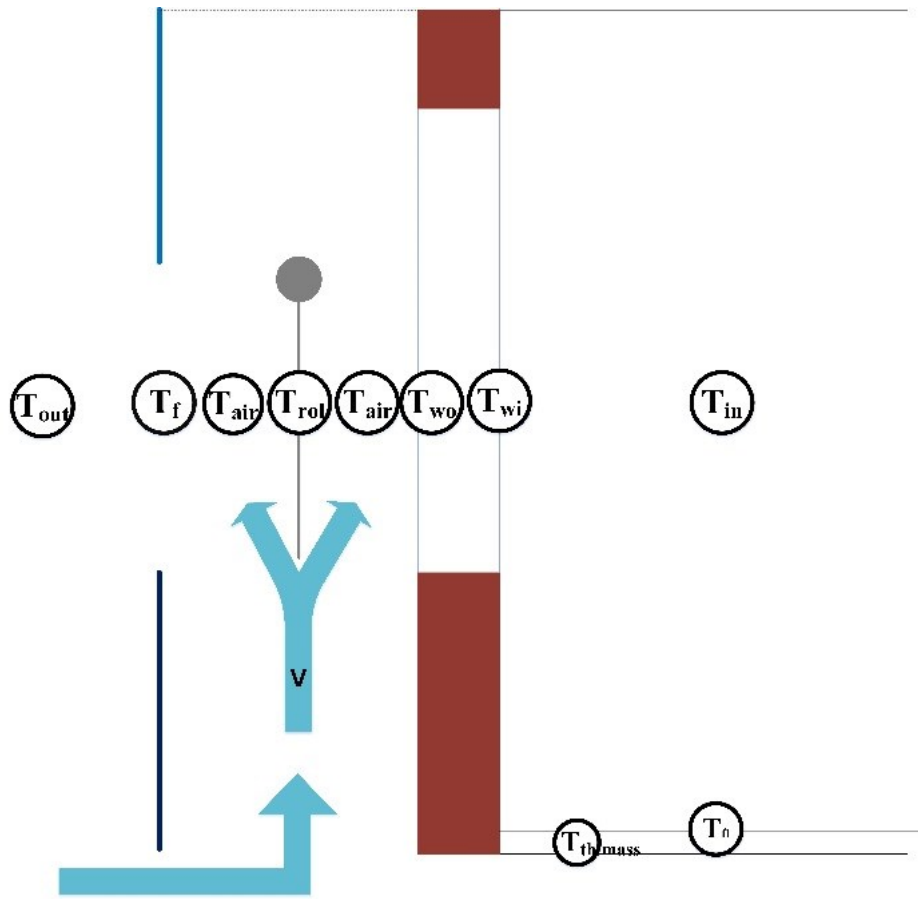


Figure 3.3: A façade schematic indicating the major nodes

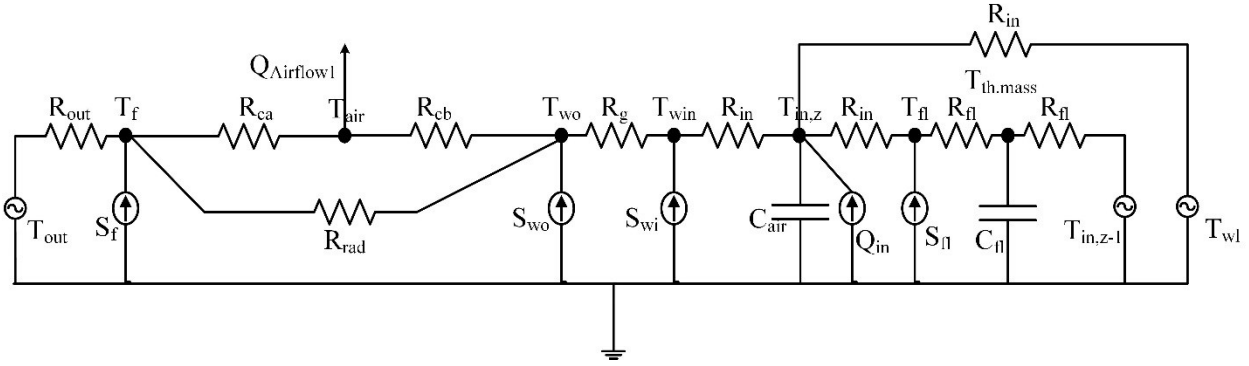


Figure 3.4: Thermal Network for the control volume with shading device, having one airflow

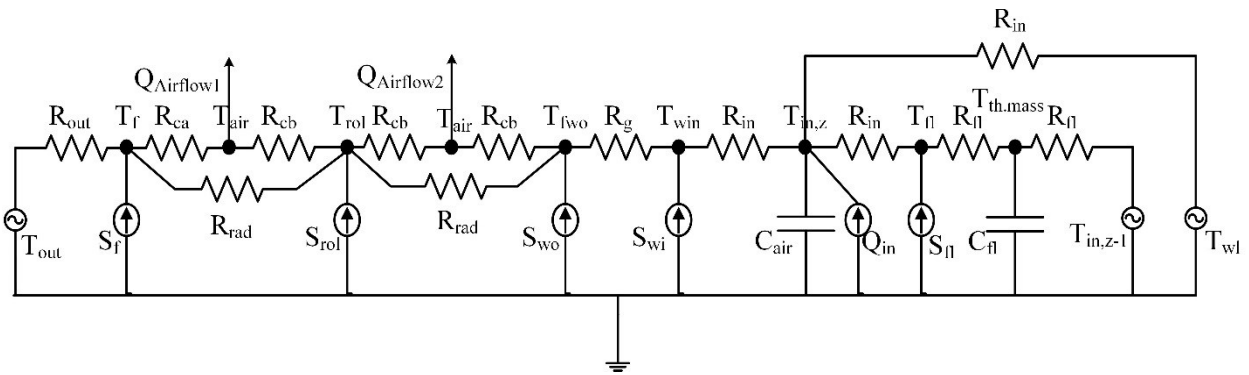


Figure 3.5: Thermal Network for the control volume with a shading device, having two airflows

- T : Temperature node
- R : Resistance equivalent
- S : Solar radiation
- Q : Auxiliary heating or cooling
- C : Thermal capacitance
- $Q_{Airflow}$: Equivalent heat source at the airflow inside the cavity

Each node at the two skins of the DSF-P are linked with the previous and the following nodes with a thermal resistance, while the airflow that leaves one control volume is introduced to the next one. In this way the temperature of the outlet of each control volume is the inlet temperature of the following one. The thermal resistance of the roller blind is considered negligible while it is assumed that no air passes through the shade and the air flow at the two sides of the roller blind are assumed to be equal. This assumption is consistent with the literature, in which, when venetian blinds are implemented within the cavity and the slat tilt angle is 0^0 , blocking in this way the air

exchange between the two channels, the airflow rates in both channels are almost identical. (Safer et al., 2005). This can be seen on Figure 3.6 where the velocity profile on the left and the right of the shading device is almost the same.

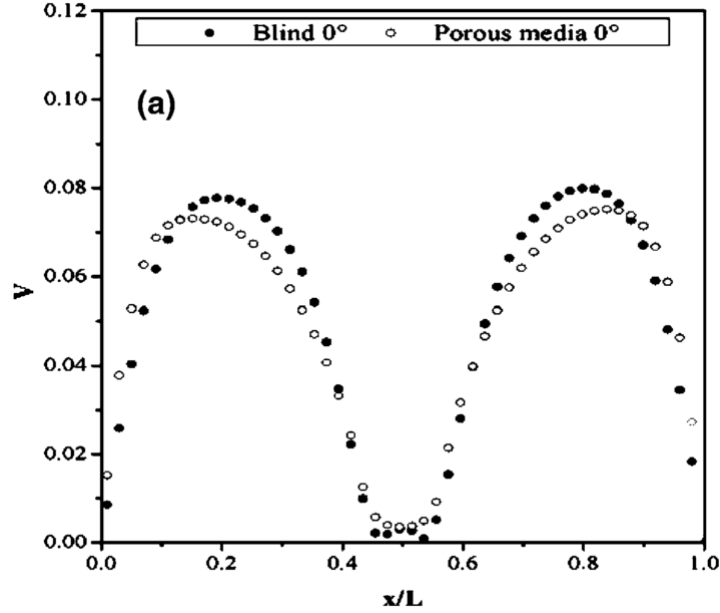


Figure 3.6: Velocity profiles inside the channel for blind and porous media for a tilt angle of 0° (Safer et al., 2005)

In order to capture the gradient of the air temperature along the cavity, each element of the multi-storey DSF-P (i.e. the façade, the two air channels, and the wall) is subdivided, along the vertical direction, in N equal control volumes (i.e. N is suitably selected to enhance the accuracy of the simulation results), whose temperatures are calculated through the energy balance method. The multi-storey building adjacent to the DSF-P is subdivided in Z different perimeter thermal zones as well. Each perimeter zone describes one room at the back of DSF-P. Therefore, in each time step t , for each z -th perimeter zone and for each n -th section/node of the façade, the corresponding energy balance equation is calculated as:

$$\sum_{i=n-1}^{n+1} \frac{T_{f,i} - T_{f,n}}{R_{f,i}} + \frac{T_{out} - T_{f,n}}{R_{ext,n}} + \frac{T_{air,n} - T_{f,n}}{R_{ca,n}} + \dot{Q}_{f,n} + \dot{Q}_{rad,n} = 0 \quad (1)$$

T_f : the temperature of the façade exterior skin ($^\circ\text{C}$)

- T_{out} : ambient air temperature (°C)
 T_{air} : temperature of the air within the cavity (°C)
 R_f : conductive resistance of each half section of the façade
 R_{ext} : external convective resistance
 R_{ca} : convective resistance calculated within the cavity
 \dot{Q}_f : the net radiation exchange, due to the sum of the incoming radiation directly absorbed by the surface and the radiative heat transfer between the exterior facade surface and the sky
 \dot{Q}_{rad} : long-wave radiation exchange on the internal surfaces within the cavity

The wall that separates the cavity from the interior space is modeled with two nodes. One at the exterior and one at interior surface of the wall. Along the vertical direction, N sections for each of these surfaces and N resistive thermal nodes for each storey, are taken into account. For such nodes, the boundary conditions are the air flowing within the cavity and the indoor air, respectively. In particular, similarly to equation (1), for each perimeter building zone and for each n-th section/node of the exterior and interior wall surfaces, the corresponding energy balance equations are calculated as:

$$\frac{T_{air,n} - T_{wo,n}}{R_{ca,n}} + \frac{T_{wi,n} - T_{wo,n}}{R_{wl,n}} + \dot{Q}_{wo,n} + \dot{Q}_{rad,n} = 0 \quad (2)$$

$$\frac{T_{wo,n} - T_{wi,n}}{R_{wl,n}} + \frac{T_{in,k} - T_{wi,n}}{R_{int,n}} + \dot{Q}_{wi,n} = 0 \quad (3)$$

- T_{wo} : temperature of the exterior wall (°C)
 T_{wi} : temperature of the interior wall (°C)
 T_{in} : temperature of the room (°C)
 R_{wl} : conductive resistance of the wall (K/W)
 R_{int} : internal convective resistance (K/W)
 \dot{Q}_{wo} : effective solar radiation incident on the external wall surface (W)
 \dot{Q}_{wi} : effective solar radiation incident on the internal wall surface (W)

The radiative heat transfer problem within the channel is solved by assessing the view factors and the radiosities of all sections constituting the cavity included between the façade and the facing surfaces, i.e. roller shades and/or wall. The way that the view factors are calculated is explained in detail in the next paragraph (chapter 3.2.3).

$$\dot{Q}_{f,n} = [\alpha_{f,n} I_{f,n} + \varepsilon_n \sigma F_{sky} (T_{sky}^4 - T_{f,n}^4)] A_n \quad (4)$$

α_f : exterior façade absorbance (-)

ε : exterior façade emissivity (-)

I_f : incident solar radiation (W/m²)

F_{sky} : view factor between the façade section and the sky (-)

T_{sky} : sky temperature (°C)

A : section surface (m²)

The wind and buoyancy-driven air flow in the cavity is assumed to be quasi-steady and for each of the N control volumes in which each air channel is discretized, an energy balance is written. It must be noted that the air temperature of the channels inside the DSF-P describe the radiation exchange, convection and mass transfer, including the identification of the heat transfer coefficients. The convective heat transfer coefficients are going to be investigated in detail on a separate section.

As reported in previous studies, the temperature profile in a ventilated cavity is exponential (Charron and Athienitis, 2006). Thus, with the aim to avoid the use of an air temperature profile, the change of energy of each control volume is assumed equal to the energy transferred to the air by convection. This leads, after solving a first order differential equation of air temperature, to an expression that provides an exponential profile.

$$T_{air,n} = \exp\left(-\frac{R_{ca,n}^{-1} + R_{ext,n}^{-1}}{\dot{m}c_{p,air}}\right) T_{air,n-1} + \left[1 - \exp\left(-\frac{R_{ca,n}^{-1} + R_{ext,n}^{-1}}{\dot{m}c_{p,air}}\right)\right] \left(\frac{R_{ca,n}^{-1} T_{f,n} + R_{ext,n}^{-1} T_{wo,n}}{R_{ca,n}^{-1} + R_{ext,n}^{-1}}\right) \quad (5)$$

\dot{m} : mass flow rate inside the cavity (kg/s)

c_p : specific heat capacity of the air (kJ/kgK)

Different boundary conditions are taken into account and no air leakage is assumed in the DSF-P cavity.

For each z -th indoor space adjacent to the DSF-P system, its indoor air is assumed as uniform and perfectly mixed. Therefore, a single lumped indoor air temperature node is taken into account. In order to assess the transient effects induced by the thermal mass. The floor thermal mass is lumped in a single capacitive node, whereas the thermal effect of interior walls are disregarded (i.e. also assuming the same temperature in the core zones of the whole building). This entails that for each z -th zone, the differential equations describing the energy rate of change of each temperature node of the air and floor is calculated as:

$$T_{fl,z}^t = T_{fl,z}^{t-1} + \frac{\Delta t}{C_{fl,z}} \left(\dot{Q}_{fl,z} + \sum_{k=1}^N \frac{T_{wi,k} - T_{fl,z}^{t-1}}{\bar{R}_{rad,n}} + \frac{T_{in,z} - T_{fl,z}^{t-1}}{\bar{R}_{fl,int}} \right) \quad (6)$$

$$T_{in,z}^t = T_{in,z}^{t-1} + \frac{\Delta t}{C_{in,z}} \left(\dot{Q}_{in,z} + \sum_{k=1}^N \frac{T_{wi,k} - T_{in,z}^{t-1}}{\bar{R}_{int,n}} + \frac{T_{fl,z} - T_{in,z}^{t-1}}{R_{fl,int}} \right) \quad (7)$$

T_{fl} : temperature of the floor capacitive node (°C)

T_{in} : temperature of the air node (°C)

Δt : time step (s)

C_{fl} : thermal capacitance of the floor capacitive node (J/K)

C_{in} : thermal capacitance of the indoor air capacitive node (J/K)

\dot{Q}_{fl} : solar heat source at the floor node (W)

\dot{Q}_{in} : overall sensible heat gain networked to the indoor air node (W)

\bar{R}_{rad} : the radiative thermal resistance between the internal wall surfaces and the floor (K/W)

$\bar{R}_{fl,int}$: the combined convective and radiative thermal resistance between the indoor air and the floor (K/W)

By following this approach, thermal power is added to or subtracted from $\dot{Q}_{in,z}$ with the aim to maintain the indoor air temperature at the desired set points.

3.1.1 Modeling of the Photovoltaics

It is also assumed that uniform solar radiation is incident on clean exterior surfaces and PV modules are operating at their maximum power point condition.

$$P_{el} = \eta_{PV} I_{f,n} A_n \quad (8)$$

P_{el} : electrical power production from the photovoltaics (W)

η_{pv} : efficiency of the photovoltaics (-)

I_f : incident solar radiation on the exterior façade (W/m²)

A_n : area of the photovoltaic modules (m²)

Where the photovoltaic efficiency is assumed to be linear decreasing with the increasing operating temperature (Sandberg, 1999) taking into consideration the photovoltaic module efficiency at standard test conditions, the photovoltaic module temperature coefficient and the cell temperature under standard test conditions.

$$\eta_{PV} = \eta_{stc} [1 - \beta_{PV} (T_{PV} - T_{stc})] \quad (9)$$

η_{stc} : efficiency of the photovoltaics under standard test conditions (-)

β_{pv} : photovoltaic module temperature coefficient (-)

T_{pv} : temperature of the photovoltaic module (°C)

T_{stc} : temperature of the photovoltaics under standard test conditions (°C)

3.1.2 Longwave radiation heat transfer and view factors in the DSF-P

The exterior skin of the DSF-P consists of three different sections having an opaque, glazing and a semi-transparent photovoltaic (Figure 3.1). The opaque photovoltaics are expected to perform in higher temperatures than the semi-transparent photovoltaics, and both the photovoltaics to have higher temperatures than the glazing. This lack of uniformity on the exterior skin has an effect on the heat transfer due to radiation exchange, which must be accurately taken into account. In addition, in the case where the roller blind is implemented on the middle of the cavity, the radiation exchange between some areas of the exterior and the interior skins are interrupted.

For assessing the radiative heat transfer within the cavity, all the view factors were calculated. The complexity of the radiative model developed for the DSF-P is mainly due to the fact that the model is automatically scalable, as it follows the number of the control volumes chosen.

The areas of the DSF that are demarcated by the control volumes on each skin are strips along the width of the façade. The view factors between each strip on the exterior skin and the different strips on the interior skin have been calculated. The same methodology is followed in order to calculate the view factors between each strip on the exterior skin and the strips of the roller blind.

In the implemented model, the double area integration approach is taken into account for the calculation of the fundamental expression for a view factor between isothermal, black-body, diffusely emitting and reflecting surfaces (Walton, 1986):

$$F_{1 \rightarrow 2} = \frac{1}{\pi A_i} \iint_{A_1 A_2} \frac{\cos \alpha_1 \cdot \cos \alpha_2}{r_{12}^2} dA_2 dA_1 \quad (10)$$

r : distance between the barycenters of the two sub-surfaces

$\alpha_{i,j}$: angles between r and the respective normal vectors

The equation above is numerically integrated by dividing the N sub-surfaces of the DSF parallel surfaces into a high number of rectangular finite control surfaces. The adoption of a high order spatial discretization scheme aims at increasing the accuracy of the results (Shapiro, 1985). Thus, each n -th surface is sub divided into $N_x \times N_y$ rectangular elements (i.e. N_x divisions along the horizontal edge and N_y divisions along the vertical edge) of the same area. In so doing, equation (10) becomes:

$$F_{i \rightarrow j} = \frac{1}{\pi A_i} \sum_{i=1}^{N_x} \sum_{j=1}^{N_y} \frac{\cos \alpha_i \cdot \cos \alpha_j}{r_{ij}^2} \Delta A_i \Delta A_j \quad (11)$$

The appropriate number of divisions ($N_x \times N_y$) is previously selected such as the difference between the analytical solution of the view factor between the two parallel plates of the DSF (Shapiro, 1985) and the sum of the n -th view factors calculated by the equation (11) is lower than a specified tolerance.

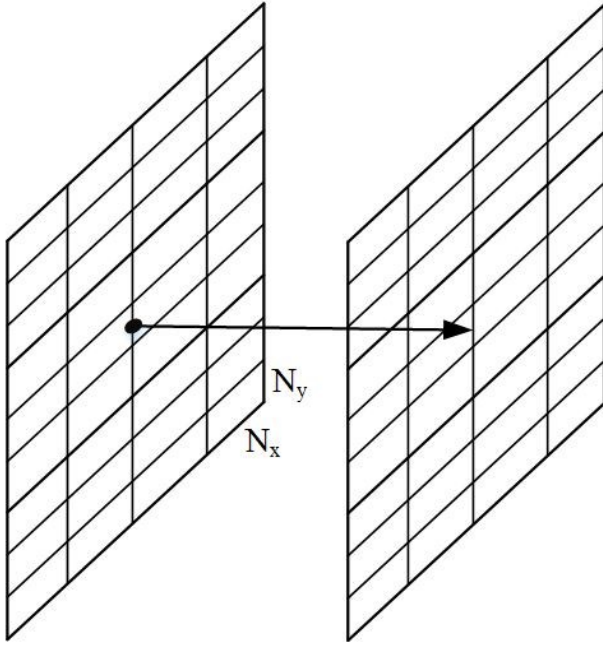


Figure 3.7: Discretization of typical surface to obtain view factors between them

Finally, with respect to the symmetric view factors between the façades cavity and the edge reradiating surfaces (e.g. $F_{i \rightarrow \infty i}$ and $F_{i \rightarrow \infty o}$ between the façades surfaces and the bottom (inlet section) and top (outlet section) of the cavity, $F_{i \rightarrow l}$ between the façades surfaces and the lateral surfaces, $F_{\infty i \rightarrow \infty o}$ between the bottom and the top façades, $F_{l^+ \rightarrow l^-}$ between the lateral surfaces) are calculated according to the geometric correlations for parallel equal rectangular plates and adjacent rectangles (Incropera and DeWitt, 2011):

$$F_{12} = \frac{2}{\pi XY} \left[\ln \left(\frac{(1+X^2)(1+Y^2)}{1+X^2+Y^2} \right)^{0.5} - X \tan^{-1} X - Y \tan^{-1} Y \right. \\ \left. + X(1+Y^2)^{0.5} \tan^{-1} \frac{X}{(1+Y^2)^{0.5}} + Y(1+X^2)^{0.5} \tan^{-1} \frac{Y}{(1+X^2)^{0.5}} \right] \quad (12)$$

$$F_{12} = \frac{1}{\pi L} \left[L \tan^{-1} \frac{1}{L} + N \tan^{-1} \frac{1}{N} - (N^2 + L^2)^{0.5} + \tan^{-1} \frac{1}{(N^2 + L^2)^{0.5}} \right. \\ \left. + \frac{1}{4} \ln \frac{(1+L^2)(1+N^2)}{1+L^2+N^2} \left(\frac{L^2(1+L^2+N^2)}{(1+L^2)(1+N^2)} \right)^{L^2} \left(\frac{N^2(1+L^2+N^2)}{(1+L^2)(1+N^2)} \right)^{N^2} \right] \quad (13)$$

In the case of the presence of the obstructing roller blind located within the cavity, the view factor between interrupted sub-surfaces are set to be equal to zero. Therefore, in order to determine the view factor between two interrupted cavity sub-surfaces, a suitable algorithm was implemented. Specifically, depending on the roller blind position in the cavity, the two extreme pairs of sub-surfaces of the cavity facades connected by virtual lines are defined by means of geometric considerations, as shown in Figure 3.8.

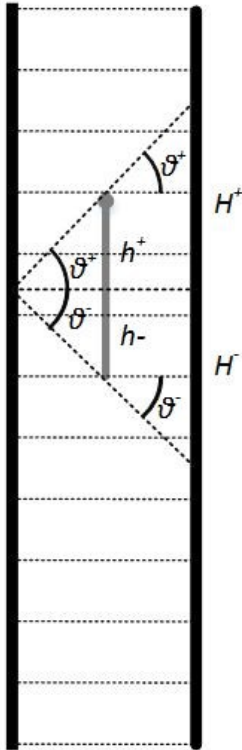


Figure 3.8: Obstructed view of the each strip

Here, it is possible to observe that all the pairs of obstructed sub-surfaces are those delimited by the segment H^+ and H^- , whose dimensions are calculated by the knowledge of the θ^+ and θ^- angles between the normal and the extreme connection lines. It is worth noting that the segments H^+ and H^- are equal to $2 \times h^+$ and $2 \times h^-$ if the obstruction (i.e. roller blind) is located at the middle of the cavity.

3.1.3 Radiosity method inside the cavity

In the simulation model, the calculation of the radiative heat flux within the cavity surfaces was carried out by taking into account a two-dimensional rectangular enclosure (Figure 3.8) with non-

participating media by using a finite element technique (Incropera and DeWitt, 2011). To do that the view factors, calculated inside the cavity are used (see section 3.2.2).

The bottom and top of the cavity, as well as the side surfaces, were assumed to be adiabatic and reradiating with a floating temperature distribution. The DSF's cavity surfaces were subdivided in N sub-surfaces, whereas single whole surfaces were taken into account for the remaining edge elements (i.e. two surfaces for the bottom and top of the cavity, and the lateral surfaces assumed to be at the same temperature). On each sub-surface the radiosity, J_n , is assumed to be uniform, and the radiative heat flux ($\dot{Q}_{rad,n}$ in equation (1)) is related to its temperature (i.e. emissive power, E_n) and to J_n , as it follows:

$$\sigma \cdot T_{f/wo,n}^4 = J_n + \frac{1 - \varepsilon_n}{\varepsilon_n} \cdot \sum_{k=1}^{\bar{N}} F_{n-k} (J_n - J_k) \quad (14)$$

σ : Stefan-Boltzmann constant ($5.67 \cdot 10^{-8} \text{ W/m}^2\text{K}^4$)

$T_{f/wo}$: Temperature of the façade or the exterior part of the wall (K)

J_n : Radiosity (W/m^2)

ε_n : Emissivity (-)

\bar{N} : Number of the surface enclosures (-)

n : Number of subsections (-)

In order to determine the unknown radiosities and temperatures of the \bar{N} -surface enclosure, (i.e. including all sub-surfaces and surfaces, with $\bar{N} = 2 \cdot N + 4$), a system of \bar{N} linear algebraic equations, combined in a matrix form, is solved (Shapiro, 1985).

3.1.4 Heat transfer coefficients

The local Nusselt numbers (Nu) are used in order to represent the convective heat transfer coefficients along the channel height. Nusselt number correlations developed by Liao et al. (Liao et al., 2007) for the façade and internal side are used:

$$Nu_f = (0.011Re + 62.856)e^{-0.475 \frac{H}{L_{ca}}} + (2.766 \times 10^{-3})Re + 5.58 \quad (15)$$

$$Nu_{int} = (0.109Re - 124.34)e^{(-1.635 \times 10^{-5} Re - 0.593) \frac{H}{L_{ca}}} + (4.098 \times 10^{-3})Re + 3.896 \quad (16)$$

Also by using the definitions of Nusselt and Reynolds number the local convective heat transfer coefficients are generated.

$$Nu = \frac{h_{ca} D_{ca}}{K_{air}} \quad (17)$$

$$Re = \frac{\rho_{air} V_{air} D_{ca}}{\mu} \quad (18)$$

$$D_{ca} = \frac{2W_{ca}L_{ca}}{W_{ca} + L_{ca}} \quad (19)$$

$$\rho_{air} = 1.2 \text{ (kg/m}^3\text{)} \quad (20)$$

$$\mu = [0.1983 + 0.00184(T_{air} - 300.15)]10^{-5} \quad (21)$$

Nu : local Nusselt number (-)

h_{ca} : convective heat transfer coefficient inside the cavity (W/m²K)

D_{ca} : hydraulic diameter of the cavity (m)

K_{air} : thermal conductivity of air (W/mK)

Re : Reynolds number (-)

ρ_{air} : air density (kg/m³)

V_{air} : velocity of the air inside the cavity (m/s)

μ : dynamic viscosity (Ns/m²)

T_{air} : temperature of the air inside the cavity (K)

The exterior convective heat transfer coefficients caused by the wind are calculated based on the equation developed by Emmel (2007).

$$\begin{aligned} h_{out} &= 5.15V_w^{0.81} & \theta &\leq 22.5^\circ \\ h_{out} &= 3.34V_w^{0.84} & 22.5^\circ &< \theta \leq 67.5^\circ \\ h_{out} &= 4.78V_w^{0.71} & 67.5^\circ &< \theta \leq 122.5^\circ \end{aligned} \quad (22)$$

$$h_{out} = 4.05V_w^{0.77} \quad 122.5^\circ < \theta \leq 157.5^\circ$$

$$h_{out} = 3.54V_w^{0.76} \quad \theta > 157.5^\circ$$

h_{out} : exterior convective heat transfer coefficient (W/m²K)

V_w : wind velocity that has been adjusted for height above ground (m/s)

Concerning the room, the combined interior radiative and convective heat transfer coefficient is assumed to be constant (8 W/m²K). The model can be expanded in the future to include a more detailed nonlinear coefficient in conjunction with a more detailed room model.

3.2 Shading

3.2.1 Positioning of the PV on the Exterior Skin

The position of the Semi-transparent photovoltaics on the DSF-P is of great importance due to the shading that they provide and the possible obstruction of the view. The use of this configuration is to minimize the heat losses, control the solar gains and at the same time provide the building with adequate daylight. The concept of three section façade (Tzempelikos et al., 2007) is applied for the exterior skin of the DSF. The façade in this way is discretized into three different section:

- i) the spandrel section
- ii) the viewing section
- iii) the daylight section

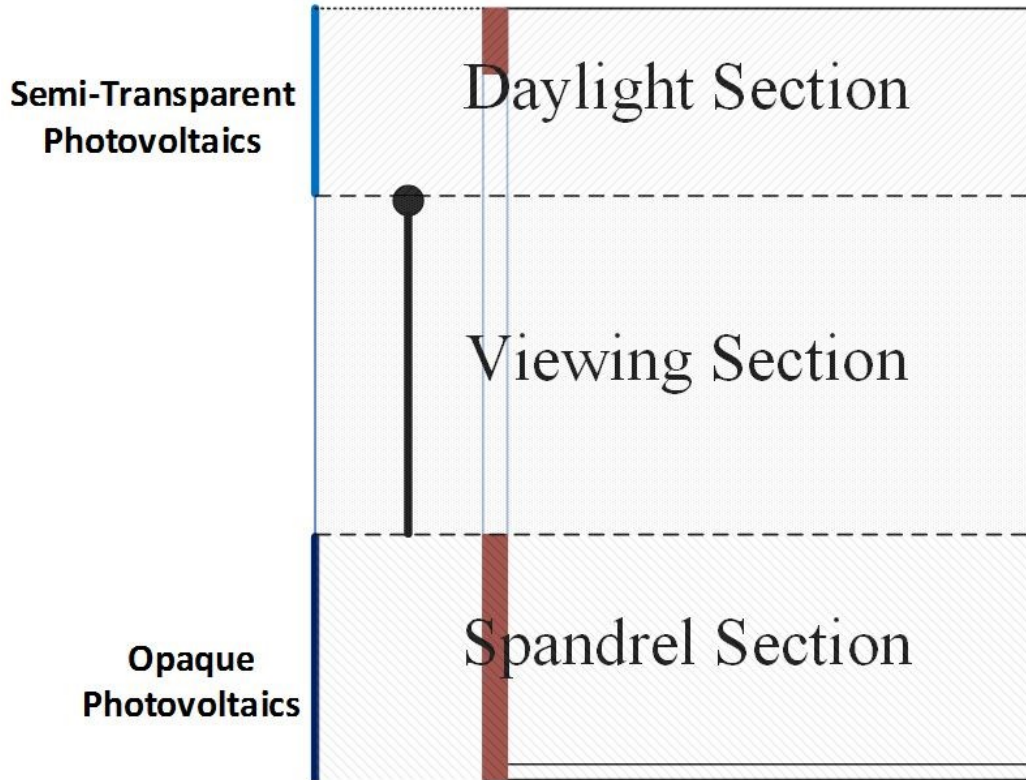


Figure 3.9: Three section façade

The opaque photovoltaics are integrated on the exterior skin at the spandrel section and the semi-transparent at the daylight section. The height of the opaque photovoltaic (H_{OPV}) section is equal to the height of the spandrel section (H_{sp}) on the interior wall.

In order to take advantage of the shading that the photovoltaics provide to the interior skin, the height of the STPV (H_{STPV}) is defined in this way in order to shade the interior zone during the cooling season. This is done by calculating the length of an overhang which prevents the direct solar radiation from entering the room beginning at the solar noon of April 15 (Kreider et al., 2002). In this way, solar radiation is blocked from entering the zone during the summer months but it is allowed to enter the room, during the winter months, when the solar gains are needed in order to passively heat the interior of the building.

Then the part of the overhang that exceeds the length of the cavity is projected on the exterior skin and the height of the STPV (H_{STPV}) is calculated, having in this way the same effect that an overhang would have (eq. 23,24). In addition, because the STPV does allow a part of the solar radiation to be transmitted to the inside, the daylighting levels of the interior space can be improved.

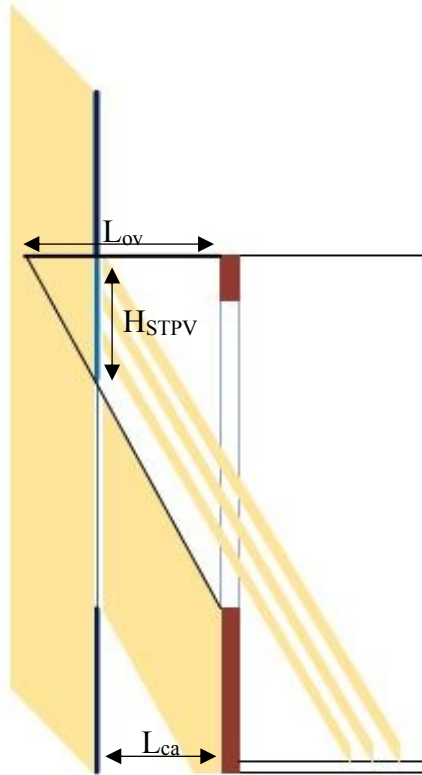


Figure 3.10: The semi-transparent photovoltaics integrated on the exterior skin act as an equivalent overhang

$$L_{ov} = \frac{(H_{wd} + H_{usp})}{\tan d} \quad (23)$$

$$H_{STPV} = \tan(d) * (L_{ov} - L_{ca}) \quad (24)$$

L_{ov} : optimal length of the overhang (m)

H_{wd} : window height (m)

H_{usp} : upper spandrel height (m)

d : profile angle ($^{\circ}$)

H_{STPV} : STPV height (m)

L_{ca} : cavity width (m)

3.2.2 Transmittance of STPV and Glazing

As it is mentioned before, the model is capable of reading imported Typical Meteorological Year data file (TMY). One of the parameters imported is the normal solar radiation and by taking into account the solar geometry equations, the direct and diffuse solar radiation are calculated for the vertical surface of the DSF-P. The simple isotropic model is usually sufficient for building simulations (Kreider et al., 2002) and is given by the following equations:

$$I_{dir} = I_{dir,n} \cos \theta \quad (25)$$

$$I_{dif,s} = I_{dif,n} \frac{(1 + \cos \theta_p)}{2} \quad (26)$$

$$I_{dif,g} = (I_n \cos \theta_s + I_{dif,n}) \rho_g \frac{(1 - \cos \theta_p)}{2} \quad (27)$$

$$I_{tot} = I_{dir} + I_{dif,s} + I_{dif,g} \quad (28)$$

The incident solar radiation on the exterior skin is absorbed, reflected and transmitted to the inside. The modeling of the transmittance of the semi-transparent photovoltaic and the glazing is determined by their properties. The extinction coefficient and the refractive index are used in order to calculate the angle of refraction and the component reflectivity. These two parameters are used in order to determine the transmittance, reflectance and absorbance of the semi-transparent photovoltaics and the glazing. The semi-transparent photovoltaic is modeled under the assumption that it has a uniform transmittance. For this reason, the extinction coefficient times the glazing thickness of the semi-transparent photovoltaic is given by:

$$Ke_{STPV} L_{STPV} = -\log(\tau_{STPV}) \quad (29)$$

Ke_{STPV} : extinction coefficient of STPV (m^{-1})

L_{STPV} : thickness of STPV (m)

τ_{STPV} : normal transmittance of the STPV (-)

which is a function of the overall normal transmittance of the STPV (τ_{STPV}). The same principals are used in order to model the effective transmittance and absorption of the glazing at the exterior skin and double pane window at the interior skin (Athienitis, 1998). More precisely, the solar beam radiation absorbed after many reflections is given by:

$$S_{dir} = \sum_j F_{ij} \rho_j I_{dir} \quad (30)$$

S_{dir} : Total solar beam radiation absorbed by the absorbed by each surface i (W/m²)

F: View factors inside the cavity (see chapter 3.6) (-)

ρ : Reflectance of each surface (-)

I_{dir} : Incident direct solar radiation (W/m²)

3.2.3 Shading Calculation

The integrated on the exterior skin opaque and semi-transparent photovoltaics as well as the roller blind that is implemented within the cavity, provide shading to the building and therefore affect significantly the energy balance of the system. The sun light is treated by separating the direct from the diffuse light. Concerning the direct light, the shading is calculated by the upper and the lower point of the photovoltaic panels, or the roller blind. The vertical distance between the upper or the lower point of the photovoltaic panels and shade that they provide is given by the equation (31).

$$y_{sh} = \frac{L_{ca} \tan \beta_s}{\cos a_s} \quad (31)$$

y_{sh} : vertical distance between the upper or the lower point of the photovoltaic panels and shade (m)

L_{ca} : cavity depth (m)

β_s : solar altitude (°)

α_s : surface azimuth ($^\circ$)

The area between these points is fully shaded in the case of the opaque photovoltaics and partially shaded in the case of semi-transparent photovoltaics and the roller (Figure 3.12). If the photovoltaics that are integrated on the exterior skin, shade the roller blind, then an effective transmittance of both of them is calculated for the interior skin. Because the method of control volumes is used for the energy balance and the points where the shadow begins and ends doesn't always align with the beginning and the end of each control volume, a percentage of the area that is shaded at the interior skin is taken. Further, this percentage is multiplied with the percentage of the overall transmittance of the elements that provide this shade.

For example, if the STPV with optical transmittance 30%, shades 80% of the surface area that a control volume defines and the rest 20% of this area has light transmitted through the exterior glazing with optical transmittance 70%, then the total transmitted light for this control volume is:
 $0.8 \cdot 0.3 + 0.2 \cdot 0.7 = 0.38$

3.3 Flow Network

The flow of the air inside the channel is naturally and mechanically driven. Mechanical ventilation is necessary in the cavity of the DSF-P in order to cool down the photovoltaics integrated on the exterior skin and therefore increase their efficiency and also to increase heat recovery in the heating season. For this reason, the airflow inside the cavity caused by natural effects such as stack and wind effects is also assisted by a fan. The total pressure difference because of natural means is the sum of the pressure difference due to stack effect and due to wind.

$$\Delta P_{nat} = \Delta P_{th} + \Delta P_w \quad (32)$$

ΔP_{nat} : Pressure difference caused by natural means (Pa)

ΔP_{th} : Pressure difference due to stack effect (Pa)

ΔP_w : Pressure difference due to wind effects (Pa)

Pressure difference due to stack effect related to the temperature difference between the ambient temperature and the temperature of the air within the cavity is given by:

$$\Delta P_{th} = 0.5\rho_{air}gH_{ca} \left[\frac{Tm_{ca} - T_{out}}{Tm_{ca}} \right] \quad Tm_{ca} - T_{out} \geq 0 \quad (33)$$

$$\Delta P_{th} = 0.5\rho_{air}gH_{ca} \left[\frac{Tm_{ca} - T_{out}}{T_{out}} \right] \quad Tm_{ca} - T_{out} < 0 \quad (34)$$

ρ_{air} : air density (kg/m³)

g : gravitational acceleration (9.81 m/s²)

H_{ca} : height of the cavity (m)

Tm_{ca} : average temperature of the air inside the cavity (K)

T_{out} : ambient air temperature (°C)

The pressure drop due to wind effect is given by the equation.

$$\Delta P_w = \Delta C_p 0.5\rho_{air}V_w^2 \quad (35)$$

C_p : pressure coefficients (-)

ρ_{air} : air density (kg/m³)

V_w : The velocity of the air (m/s)

The velocity of the air measured at a height of 10m above ground is used for this equation. The pressure coefficients determined experimentally by Lou et al. (2012) for twelve wind angles over 360°, are used in order to calculate via interpolation, the difference between the pressure coefficients at the exterior and the interior skin of the DSF-P (ΔC_p) (Figure 3.11).

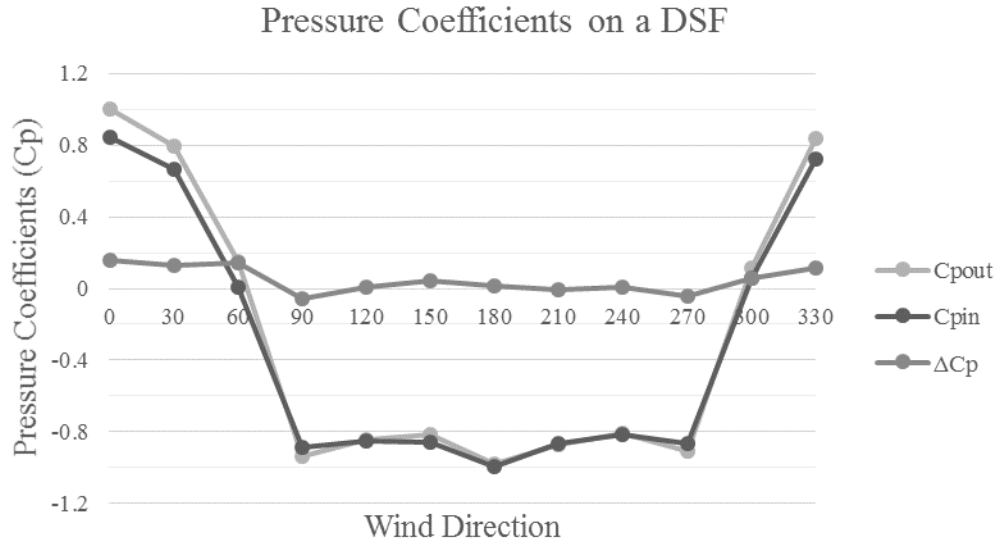


Figure 3.11: Wind pressure coefficients for 12 wind angles on a DSF (Lou et al., 2012)

$$V_{ca,th} = \frac{C_d}{A_{ca}} \sqrt{\Delta P_{nat}} \quad \Delta P_{nat} \geq 0 \quad (36)$$

$$V_{ca,th} = -\frac{C_d}{A_{ca}} \sqrt{|\Delta P_{nat}|} \quad \Delta P_{nat} < 0 \quad (37)$$

V_{ca} : velocity of the air inside the cavity (m/s)

C_d : orifice discharge coefficient (-)

A_{ca} : area of the cavity in the sagittal plane (m²)

ΔP_{nat} : Pressure difference caused by natural means (Pa)

The orifice equation used employs a discharge coefficient of $C_d=0.62$ for a flow through sharp edged rectangular objects.

The velocity of the air inside the cavity is going upwards when the pressure drop due to natural means is positive. This means that the wind effects either assists the stack effect or it is not that strong in order to oppose to it. Downward flow inside the cavity is presented when the wind effect is stronger than the stack effect leading to a negative natural pressure drop.

The total pressure drop caused by thermal, wind and mechanical systems is described by the equation:

$$\Delta P_{tot} = \Delta P_{nat} + \Delta P_{mech} \quad (38)$$

In the case where the total airflow inside the cavity, caused by natural means does not reach the desired airflow, then the fans at the top of the DSF-P start to operate in order to maintain the air velocity inside the cavity at the desired levels.

This pressure drop due to mechanical system is calculated by the power law where the flow is represented as a function of the total pressure difference. Then the pressure drop due to mechanical system is calculated by the use of equation 40:

$$Q = c(\Delta P_{tot})^{0.5} \quad (39)$$

$$\Delta P_{mech} = \left(\frac{V_{ca} A_{ca}}{c} \right)^2 - \Delta P_{nat} \quad (40)$$

- Q : airflow inside the cavity (m³/s)
- V_{ca} : velocity of the air inside the cavity (m/s)
- c : flow coefficient (m^{2.5}kg^{-0.5})
- A_{ca} : area of the cavity in the sagittal plane (m²)
- ΔP_{nat} : Pressure difference caused by natural means (Pa)

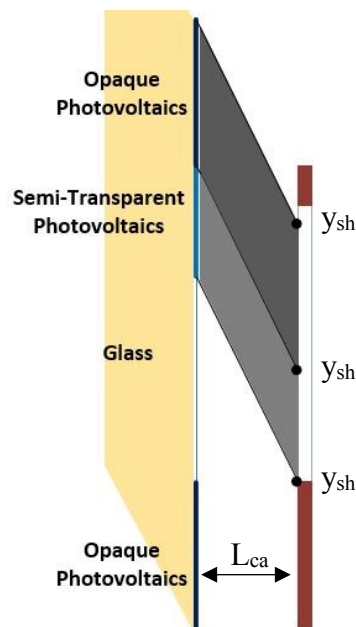


Figure 3.12: Shadows from the exterior skin to the interior. Fully shade from the opaque and semi-shade from the semi-transparent photovoltaic

3.4 Daylighting

Daylighting in double skin facades is a field that has not been extensively studied yet, particularly when combined with semi-transparent photovoltaics. In a DSF integrated with photovoltaics (DSF-P) the daylight analysis becomes more important since the photovoltaics integrated on the exterior skin shade the interior skin. Furthermore, the existence of roller blinds within the cavity is adding more to the necessity of this analysis. With new types of PV that are completely transparent and colored, a new type of analysis will also be needed.

For this reason, a simple and with low computational time daylight simulation model is created. Linked to the defined geometry a daylight model which uses the radiosity method, can estimate the illuminance at certain points inside the room. The interactive nature of the model is also followed for the daylighting modeling. More precisely, when the user defines the number of the control volumes, and thus the number of the strips that each skin of the DSF-P will be divided into, it also defines the surfaces that will be used for the radiosity method for the room. Also the number of the points for which the illuminance is going to be calculated can be defined by the user, in the x and y direction. In this way the user can choose an analysis by choosing points in the x-direction (Figure 3.13a), in the y-direction (Figure 3.13b), or both directions (Figure 3.13c).

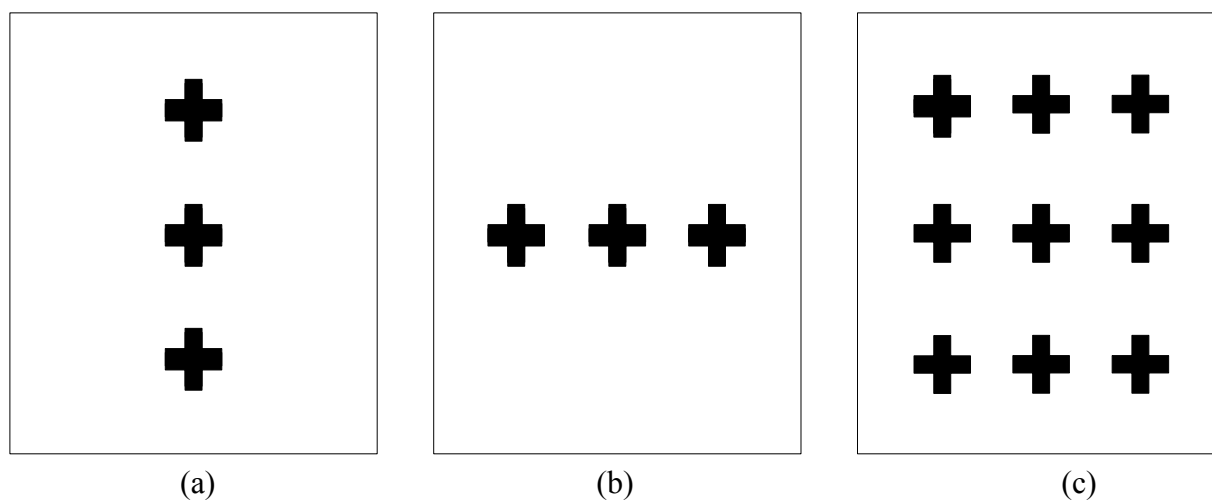


Figure 3.13: Examples of points chosen to calculate the illuminance on the work plane. (a) three points on the y-direction, (b) three points on the x-direction, (c) three points on the x and y direction.

Radiosity technique is a very fast method and in order to simplify the computations the method is based on some basic assumptions. It is assumed that all surfaces are perfectly diffuse and with homogeneous luminous exitance (visible radiation leaving the surface).

After the incident solar radiation on the internal skin of the DSF-P is calculated as explained on section 3.4.3 and taking into account the transmittance of the glazing on the interior skin, the initial luminous exitance (M_o) of the glazing is calculated. To do that the assumption that 1 W/m^2 is equal to 100 lx is used. The side of the room that is adjacent to the DSF-P, is divided into strips, defined by each control volume and has its own luminous exitance. If the strip is a spandrel or an upper spandrel, then the initial luminous exitance is 0.

The reflectances of each surface inside the room is then defined and the view factors between the surfaces of the room are calculated. To do that the following equations of a rectangular plate (Figure 3.14) to unequal rectangular plate are used:

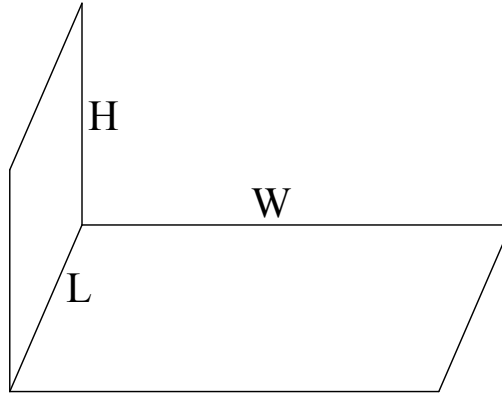


Figure 3.14: Sketch of rectangle perpendicular plates used in the view factor calculation.

$$F_{i,j}(w, h) = \left(w \tan^{-1} \frac{1}{w} + h \tan^{-1} \frac{1}{h} \right) + \sqrt{h^2 + w^2} \tan^{-1} \frac{1}{\sqrt{h^2 + w^2}} / \pi w + \frac{1}{4} \ln \left(\frac{w^2(1 + (h^2 + w^2))}{(1 + w^2)(h^2 + w^2)} \right)^{w^2} \left(\frac{h^2(1 + (h^2 + w^2))}{(1 + h^2)(h^2 + w^2)} \right)^{h^2} \frac{(1 + w^2)(1 + h^2)}{(h^2 + w^2)} / \pi w \quad (41)$$

Where:

$$w = \frac{W}{L}$$

$$h = \frac{H}{L}$$

- F: view factor (-)
- W: width of surface j (m)
- H: height of surface (m)
- L: length of the side that belongs to both surfaces (m)
- i: vertical surface (-)
- j: horizontal surface (-)

For non-adjacent rectangles, the solution can be found with the use of the view factor algebra. In the calculation of the view factors between the strips of the wall at the interior of the DSF-P and the side they are calculated separately using the convenient crossed string method (Martinez, 1995). To do that, the side walls are also divided into strips (Figure 3.15) and then with the use of equation (41) the view factors of a rectangular plate to an unequal rectangular plate are calculated. Then the view factors between the strips of the sidewalls and façade are calculated using the following equation:

For $n > m$

$$F_{m,n} = \frac{nF_{n,n} - \sum_{m=1}^n (n-m)F_{n-m,n-m} - F_{1,1}}{2(n-m)} \quad (42)$$

- n: strip surface of the wall with the window (-)
- m: strip surface of the side walls (-)

While for the case where $n < m$ the same equations in a symmetric way are used.

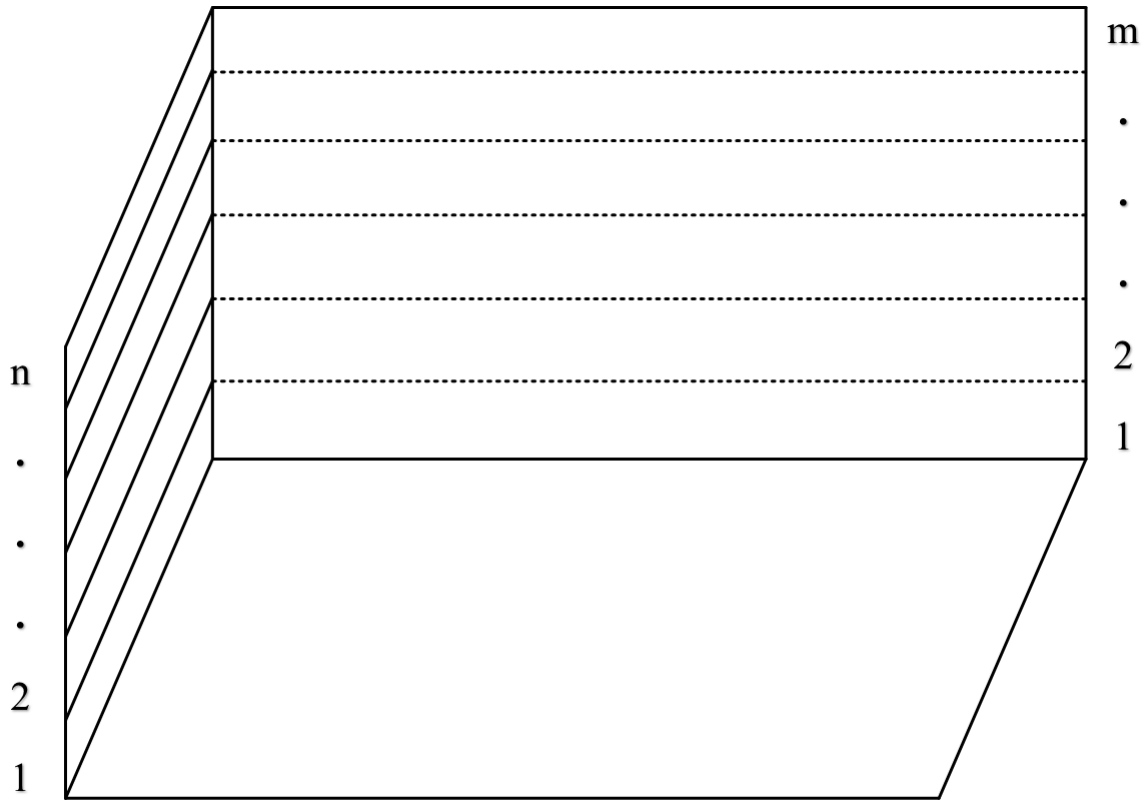


Figure 3.15: Strips on the wall of the building used for the view-factors

The formation of matrices of the initial luminous exitance, the reflectances and the view factors is necessary in order to use the inverse matrix method to solve the system. By using the following equations the final luminous exitance (M) of each surface is calculated:

$$M = (\mathbb{I} - \rho_i Fr_{i,j})^{-1} M_o \quad (43)$$

- M : final luminous exitance matrix (lx)
- \mathbb{I} : identity matrix
- ρ : reflectance matrix (-)
- Fr : view factors inside the room (-)
- M_o : initial luminous exitance matrix (lx)

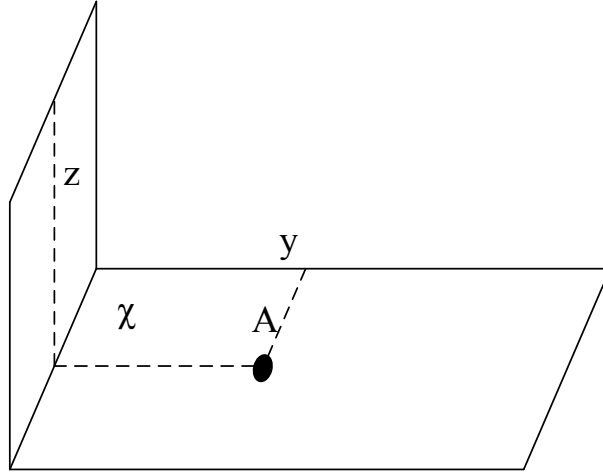


Figure 3.16: Schematic of the distances used to calculate the configuration factors

In order to calculate the illuminance at each point, the configuration factors between these points and each surface must be calculated. It is necessary to calculate the configuration factors between the points and the surfaces that located in the norther hemisphere of each point, because these are the surfaces that contribute to the illuminance of the points on the work-plane. Equation (44) (Holman, 1997) is used to find the configuration factors between a point and a vertical surface (walls) (see Figure 3.16) and equation (45) (Holman, 1997) is used for the configuration factors between a point and a horizontal surface (ceiling and floor). It should be noted that each surface must be divided into two surfaces, one at the left and one at the right of the point and thus calculate two configuration factors for each surface. In the case of the ceiling or the floor, the horizontal surface must be divided into four surfaces.

$$Cf(x, y, z) = \frac{1}{2\pi} \left(\tan^{-1} \frac{x}{z} - \frac{z}{\sqrt{y^2 + z^2}} \tan^{-1} \frac{x}{\sqrt{y^2 + z^2}} \right) \quad (44)$$

$$Cf(x, y, z) = \frac{1}{2\pi} \left(\frac{y}{\sqrt{y^2 + z^2}} \tan^{-1} \frac{x}{\sqrt{y^2 + z^2}} + \frac{x}{\sqrt{x^2 + z^2}} \tan^{-1} \frac{y}{\sqrt{x^2 + z^2}} \right) \quad (45)$$

- χ: distance between the point and the vertical surface (m)
- y: distance between the point and the side surfaces (m)
- z: distance between the point and the horizontal surfaces (m)

The horizontal illuminance at each point after infinite interreflections is calculated by:

$$E_A = \sum_{i=1}^u (M_i C f_i) \quad (46)$$

E: illuminance (lx)

M: final luminous exitance matrix (lx)

Cf: configuration factors (-)

u: total number of surfaces inside the room, after splitting them to calculate the configuration factors (-)

3.4.1 Calculation of electricity consumption for lighting

When daylight is not enough to meet this set-point, dimmable LED lighting that provides additional light to reach the required illuminance on the work-plane is assumed. In order to calculate the electricity consumed for the artificial lighting of the work-plane, the equation (47) is used. As described in 3.4 the average illuminance on the work-plane, is used in order to define the energy consumption of the lamps.

The difference between the desired illuminance set-point and the average illuminance on the work plane are calculated for each time step and for the cases where the daylight is not adequate to light the room during the working hours, the lamps are assumed to be operating.

$$P_{lamps} = \frac{(E_{setpoint} - E_{average})A_{workplane}}{n_{lamps}} \quad (47)$$

- P_{lamps} : Power consumption of the lamps (W)
- E_{setpoint} : Desired illuminance level on the work-plane (lux)
- E_{average} : Average illuminance level on the work-plane due to daylight (lux)
- $A_{\text{workplane}}$: Area of the work-plane (m^2)
- n_{lamps} : Luminous efficacy of the lamps (lm/W)

3.5 Developed control strategies

On the following tables the different strategies developed for the fans and the roller blinds are presented. Flow that is assisted by the fan (MVent), flow that is naturally developed (NVent) or without flow can be simulated and can be applied in different occasions.

Five different strategies have been developed for the use of the roller blinds, taking into consideration only the heating and cooling needs of the adjacent to the DSF-P zone. More strategies should be developed by taking into consideration the illuminance levels on the work-plane, as a result of the shading provided by the roller blind.

Table 3.2 Available strategies for the use or not of the fan

	Always	Day	Night	$T_{ca} > T_{room}$	$T_{ca} < T_{room}$	Heating mode	Cooling mode	Else
Strategy 1	MVent							
Strategy 2	NVent							
Strategy 3	Closed							
Strategy 4		MVent	NVent					
Strategy 5		MVent	Closed					
Strategy 6		NVent	Closed					
Strategy 7				MVent	Closed			
Strategy 8				NVent	Closed			
Strategy 9						Closed	MVent	NVent
Strategy 10						Closed	MVent	

Table 3.3 Available strategies for the roller blind with shading (100%) or without (0%)

	Always	Heating mode	Cooling mode	Day and Tca>Troom	Day and Tca<Troom	Day and Heating mode	Day and Cooling mode	Else
Strategy 1	Set							
Strategy 2		0%	100%					
Strategy 3				100%	0%			0%
Strategy 4				100%	0%			100%
Strategy 5						0%	100%	100%

3.6 Model Validation

In order to verify the model, a comparison between simulated values and previously collected experimental data took place. The comparison is focused on the opaque photovoltaics integrated on the exterior skin of the DSF.

More precisely, a comparison of surface temperatures of the opaque photovoltaics is held between the experimental data and the simulated values. The experimental data were retrieved from the MASc thesis of Liao (Liao, 2005), in which, data from March 2004 are presented and are collected from the experiments held on a test-hut built at Concordia University in Montreal (Canada) (Liao et al., 2007).

In order to perform the validation, the exact same conditions must be used as inputs to the model. The model allows us to change the width of the cavity, formed between the photovoltaic panel and the insulation, to 0.10m and the height of the opaque photovoltaic to 1m.

Also the typical meteorological data that are used as an input for the validation of the model, are the meteorological data from March of 2004, as they can be found on the Canadian environmental and natural resources website (Government of Canada, n.d.). On figure 3.17 the variables used for the experimental validation are presented.

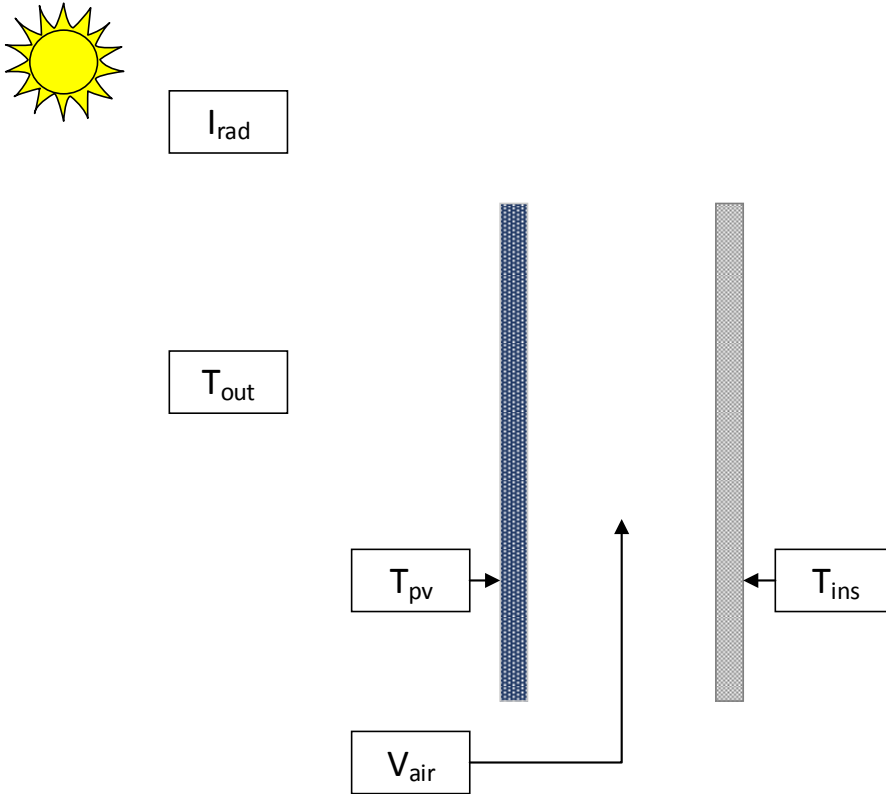


Figure 3.17: Experimentally validated variables

In Table 3.4, the temperatures of the opaque photovoltaic panel and the back insulated wall are presented and a comparison between the experimental and predicted temperatures is held for the opaque photovoltaic panel and the back insulated wall Figure 1.

The predicted results match with the experimental values within a range of 1.5°C . An exception between the measured and the simulated values is observed when the incident solar radiation is higher than the other cases. Even in this extreme case the temperature difference between the predicted and the measured is lower than 4°C , a temperature difference that does not affect drastically the efficiency of the photovoltaics and is within a range of 1.3%. Also the simulated temperature of the PV is higher than the one measured, resulting in an underestimation of the electrical production of the PV calculated by the equations (15) and (16).

This difference could be credited to the experimental error of the measurement equipment, the unknown insulating value of the experimental set-up and the also unknown wind velocity during the experimental procedure.

Table 3.4: Comparison of experimental and predicted temperatures under quasi-state conditions

March 2004	T _{out} (°C)	Average Velocity (m/s)	Incident Solar Radiation (W/m ²)	Measured		Simulated	
				T _{pv} (°C)	T _{ins} (°C)	T _{pv} (°C)	T _{ins} (°C)
10th	3.4	0.3	768.0	35.7	19.1	34.3	22.1
22th	-11.4	0.4	944.0	21.7	6.1	25.5	6.3
29th	9.7	0.4	714.0	34.5	23.6	35.5	22.8
30th	10.8	0.3	712.0	37.5	25.9	37.9	27.7

Chapter 4

4. Simulations and Results

4.0 Introduction

The interactive model, explained in detail in the previous chapter is used in order to simulate the behavior of a DSF-P under different ambient conditions. For this reason, simulations are held and presented for two typical weeks one for winter and one for summer. The 5 days selected for simulations are typical days representing average week days for each season.

In many high rise commercial buildings, the mechanical room is often located in every three stories. For this reason, a south facing three-storey DSF-P, located in Montreal (Canada) is simulated for the two different seasons described above. Every floor has a height of 2.8m, the width of the façade is 3.6m and the length between each skin is 0.5m. Each DSF-P cavity is equally discretized into 12 control volumes, while a typical insulating value of $4 \text{ W/m}^2\text{K}$ is chosen for the opaque parts of the interior skin, and $0.7 \text{ W/m}^2\text{K}$ for the double glazing low-e window.

The opaque and semi-transparent photovoltaics are simulated to be on the exterior skin of the DSF-P (Figure 4.1) and a typical roller blind ($\tau=0.1$ $\alpha=0.5$ or $\tau=0.4$ $\alpha=0.1$) is placed in the middle of the cavity. The dimensions of each section are also presented in Figure 4.1.

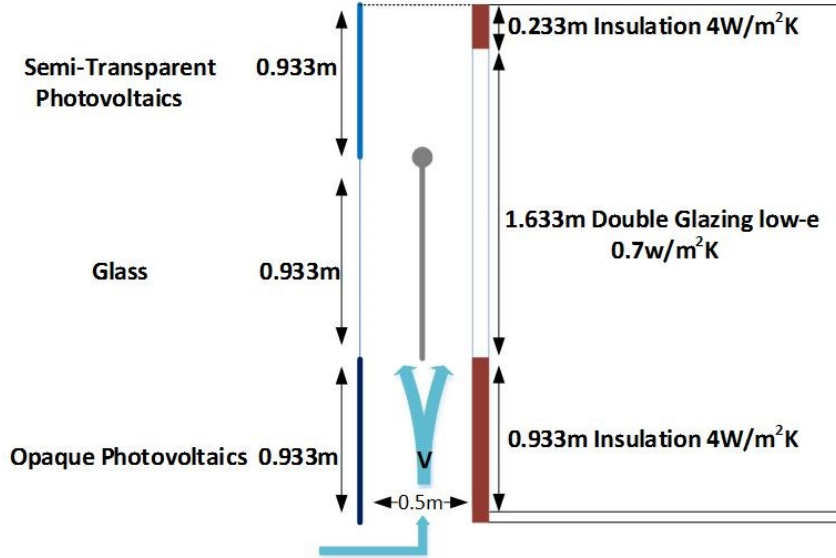


Figure 4.1: Schematic of the DSF-P simulated

The DSF-P cavity can be designed to be a narrow cavity and a wide cavity, in which people can fit to pass through it. For this reason two representative cavity widths are simulated ($L=0.25\text{m}$ and $L=0.50\text{m}$).

An air to water heat pump is assumed to be the supplier of the heating and cooling to the interior zone. The coefficient of performance (COP) ranges between 1.35 and 4.20 while the Energy Efficiency Ratio (EER) ranges between 2.74 and 9.74 (Appendix A).

The efficiency of the photovoltaics under standard test conditions is set to be 15% while dimmable LED lightning lamps with a luminous efficacy of 100lm/W are assumed to light the interior space.

4.1 Daily Analysis for a case with and without roller shade

4.1.1 Case I: Winter day (January 1st) without roller blind ($v=0.5\text{m/s}$)

The temperature at the middle of the cavity along the DSF-P is presented in Figure 4.2. For a three storey DSF-P, the maximum temperature difference between the inlet and the outlet of the DSF-P

is 2.66°C gaining almost 0.8°C per floor. It can be seen (Figure 4.2) that the temperature of the air increases mostly at the area which is behind the opaque photovoltaics.

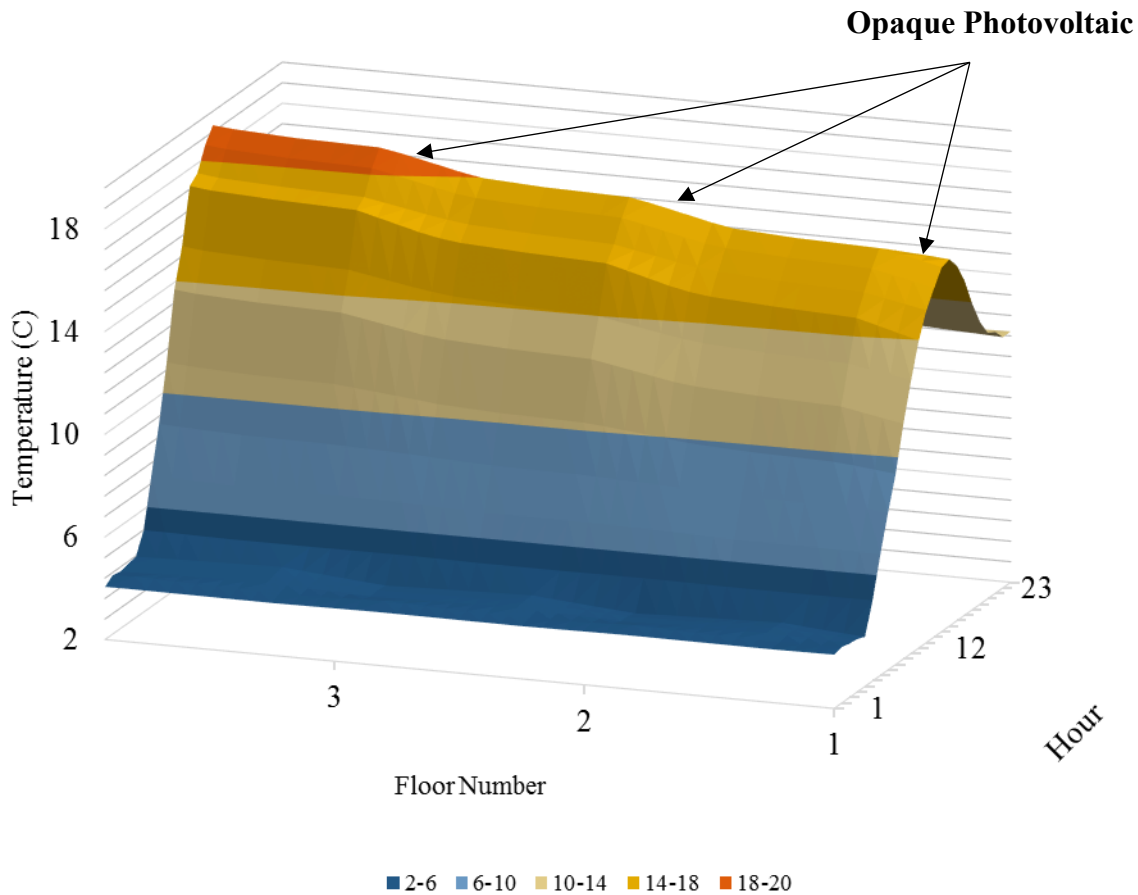


Figure 4.2: Temperature at the middle of the cavity of the DSF-P for a winter day for the case without roller blind

4.1.2 Case II: Winter day (January 1st) with roller blind ($v=0.5\text{m/s}$)

The temperature at the middle of the cavity of the DSF-P for the case with the roller blind extended along the viewing section as described in chapter 3.2, is presented in Figure 4.3. In this case, the roller blind is extended at the middle of the cavity and for this reason the temperature increases in these areas, as the roller blind absorbs energy. At the rest area, where the roller blind is not extended, the temperature of the air is presented.

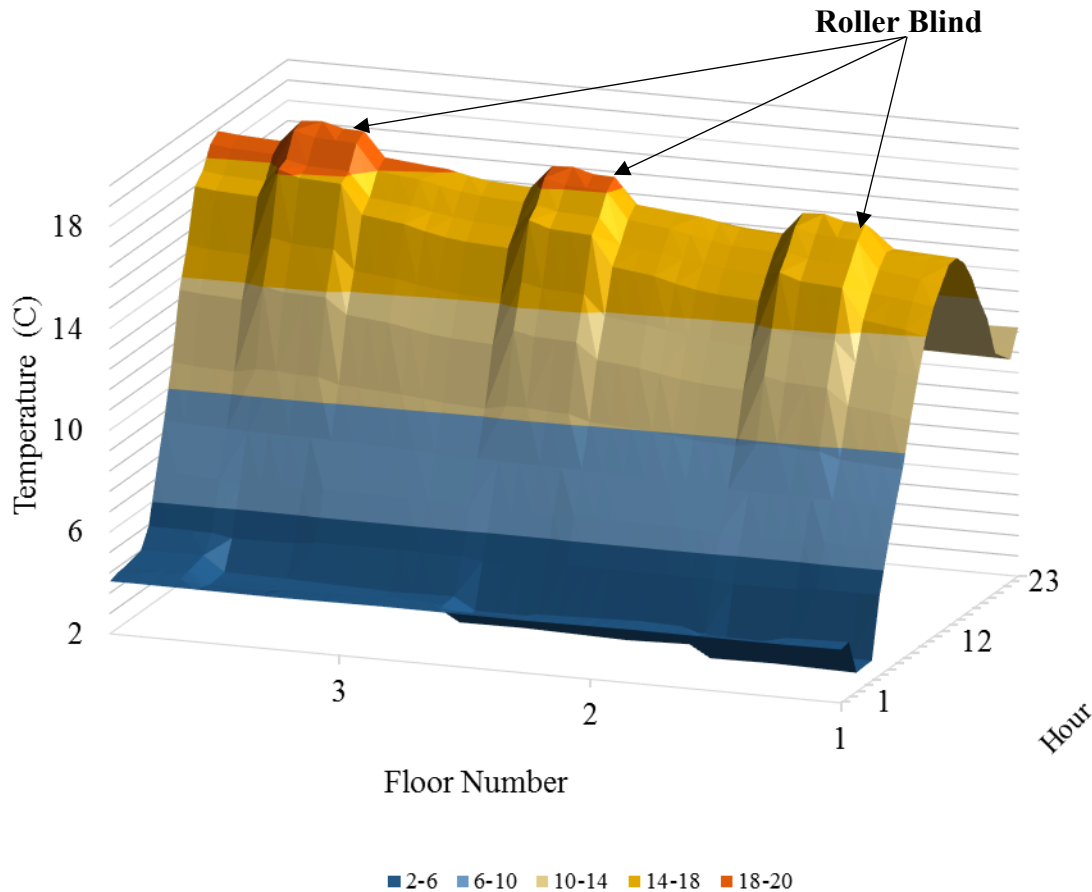


Figure 4.3: Temperature at the middle of the cavity of the DSF-P for a winter day for the case with roller blind

More cases for a spring and a summer day are presented in the Appendix B.

4.2 Typical weeks for winter and summer

4.2.1 Case I: Winter Week (January 27-31)

A typical five winter day sequence is selected for the simulations. The maximum incident solar radiation is between 600-900W/m² and the ambient temperature fluctuates between -15°C and 5°C. The temperature of the photovoltaics and of the air inside the cavity are strongly affected by these two parameters.

More specifically, the peak of the temperatures of the photovoltaics is aligned with the peak of the incident solar radiation on the façade. The temperature of the photovoltaics may reach up to 42°C, which is a 25°C higher than the ambient air temperature at this time. At the same time, it can be seen that the 30% transmittance semi-transparent photovoltaics has lower temperatures than the opaque because they absorb less energy.

The temperature of the air inside the cavity, is following the fluctuations of the ambient temperature. Because it is winter, the cavity is assumed to be closed and for this reason the temperature difference between the air within the cavity and the ambient air may reach the 15°C. It can also be seen that the temperature of the photovoltaics during the night is slightly lower than the temperature of the air and this is due to the radiation exchange with the colder sky-dome (Figure 4.4). The indoor air temperature is also presented in the same figure and the set points used for the heating is 21°C with a dead-band of 0.1°C. The heating and cooling inside the room (assumed to be an office) is provided from 7am to 6pm and the rest of the time, the temperature inside the room is let free to fluctuate. If the temperature exceeds 30°C or is less than 12°C then the room is cooled down or heated up in order to maintain the temperature at these levels.

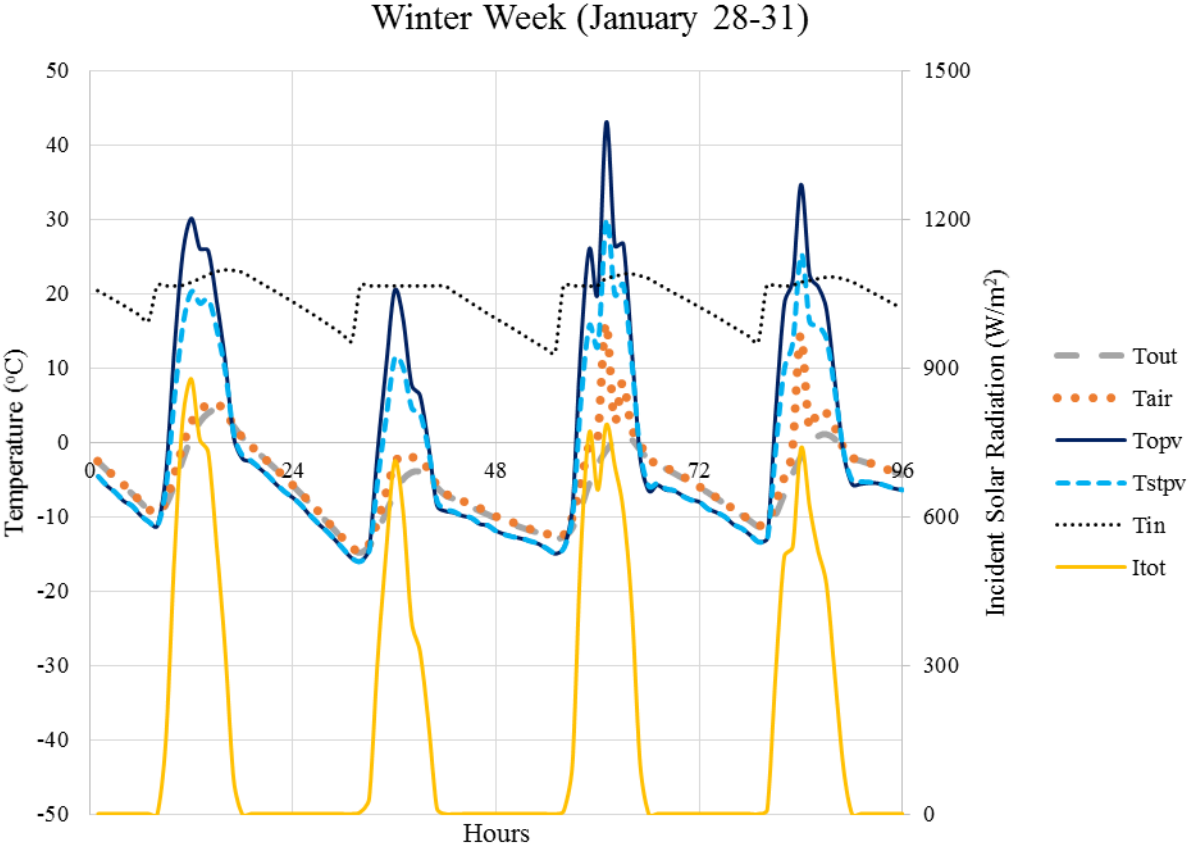


Figure 4.4: Simulated temperatures and incident solar radiation for a winter week

4.2.2 Case II: Summer Week (June 29 to July 2)

The discussion for the case I can also be repeated for the summer case. The major parameters that change are the boundary conditions of the system, which are the ambient temperature and the incident solar radiation.

The average ambient temperature fluctuates between 10°C and 25°C and the maximum of the incident solar radiation is between 300-450W/m².

Also for the Montreal and for the case of the DSF-P where the photovoltaics are mounted on a vertical position, the temperature of the opaque photovoltaics may reach temperatures up to 40°C. The indoor air temperature is also presented in the same figure and the set points used for the cooling is 24°C with a dead-band of 0.1°C.

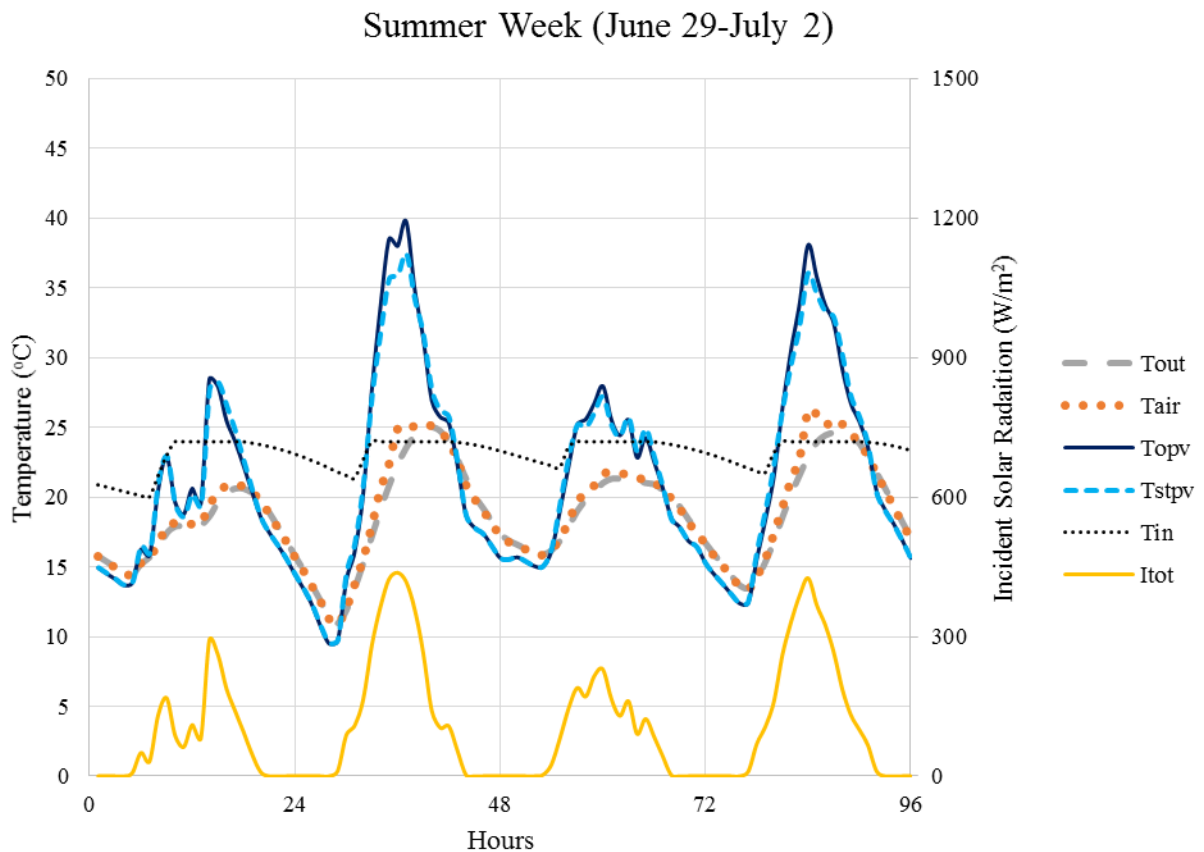


Figure 4.5: Simulated temperatures and incident solar radiation for a summer week

4.2.3 Wind effects on the DSF-P cavity for Case I: Winter Week (January 27-31)

The flow network developed and described on chapter 3.3, makes it possible for buoyancy and wind effects to be simulated. The pressure difference caused inside the cavity of the DSF-P by the temperature difference and the wind velocity and direction sometimes is enough to create an airflow inside the cavity without the additional pressure difference caused by a fan.

The cases of two different widths of the DSF-P cavity ($L=0.25\text{m}$ and $L=0.5\text{m}$) have been examined. These two cavity widths represent two different cases of DSF; the ones that people need to be able to walk across them for cleaning and safety reasons (wide DSF) and those with narrower cavities.

The velocity set-point for both cases was set to be 0.5m/s but this set point was only for the daytime. During the night the cavity is naturally ventilated (see Strategy #4 in section 3.11). It is easier for the air within the cavity to reach the velocity set point when the width is smaller ($L=0.25\text{m}$). This underlines the importance of the wind and buoyancy effects on the air flow within the cavity. (For a detailed comparison see Appendix B)

4.2.3.1 Comparison between windy and non-windy days

The velocity set-point is reached easier for the case with the narrower cavity, because the flow is driven by stronger wind and buoyancy effects. Having this in mind a set of 4 consecutive winter and summer days are presented, for the case with the wider cavity ($L=0.5\text{m}$). This is done in order to assess the impact that the wind velocity and direction has on the velocity of the air within the cavity. The days which are presented are chosen in order to compare windy and non-windy days.

For the winter days (Figure 4.6) and most specific for the first two days presented, the velocity of the air inside the cavity follows the same pattern with the velocity of the wind. During the first night, when the buoyancy effects are negligible, the effect that the wind direction has on the velocity of the air inside the cavity can be seen. Although, for high wind velocities, the velocity of the air within the cavity surpasses the velocity set-point, there are cases that this is not happening. That could be attributed to the fact that the wind direction should also be considered. The same observation can be drawn from the summer days which can be seen on Appendix B.

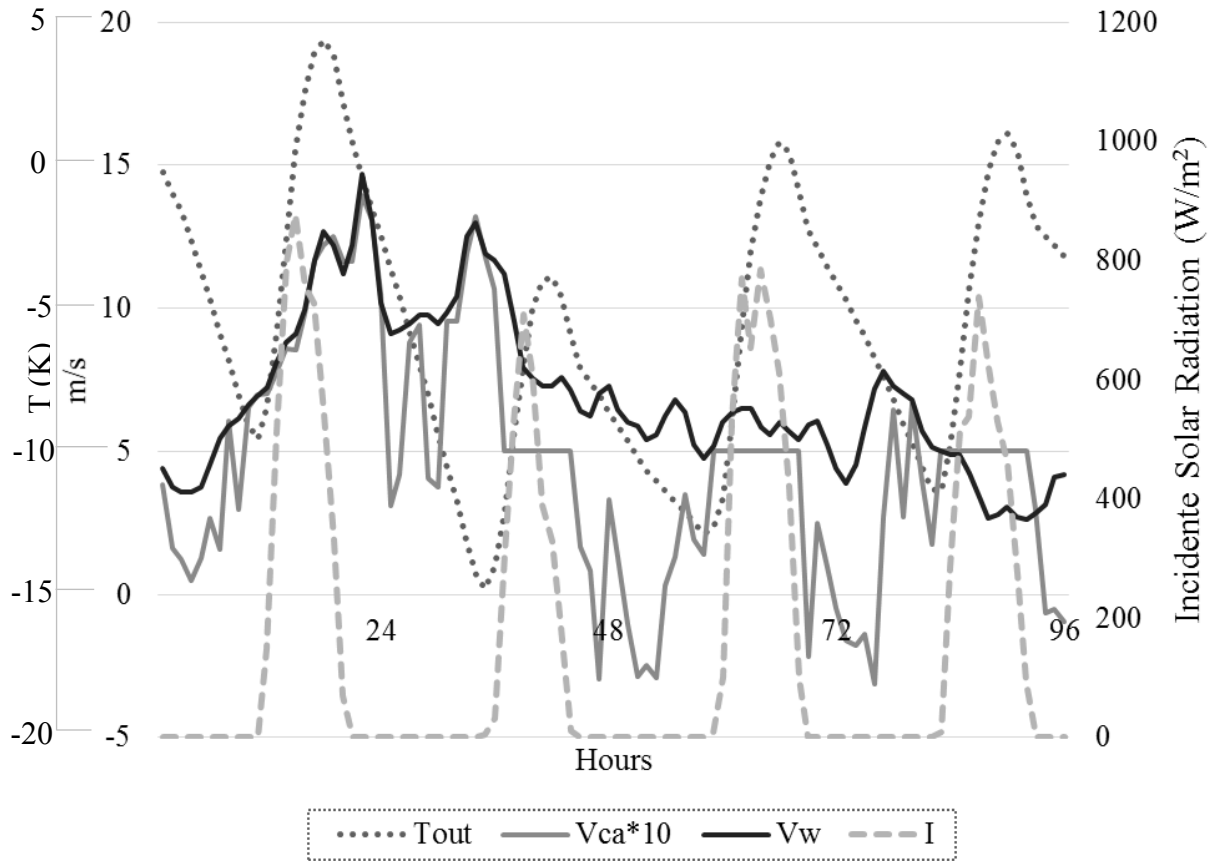


Figure 4.6: Wind and cavity velocities for four winter days for 0.50m cavity width

4.2.3.2 Wind, thermal and mechanical pressure difference inside the channel

It is mentioned before that for the narrower cavity ($L=0.25m$), the wind velocity required in order to reach the air velocity set-point is lower than in the wider cavity ($L=0.5m$). For this reason, four winter days are presented (Figure 4.7) for the narrower cavity, showing the pressure difference caused by the wind, the temperature difference and the fans.

The wind pressure difference is the main contributor to the pressure difference caused by natural means. However, as it was mentioned previously, the buoyancy effect is enough sufficient to drive the flow within the cavity, especially for the case of narrower cavity.

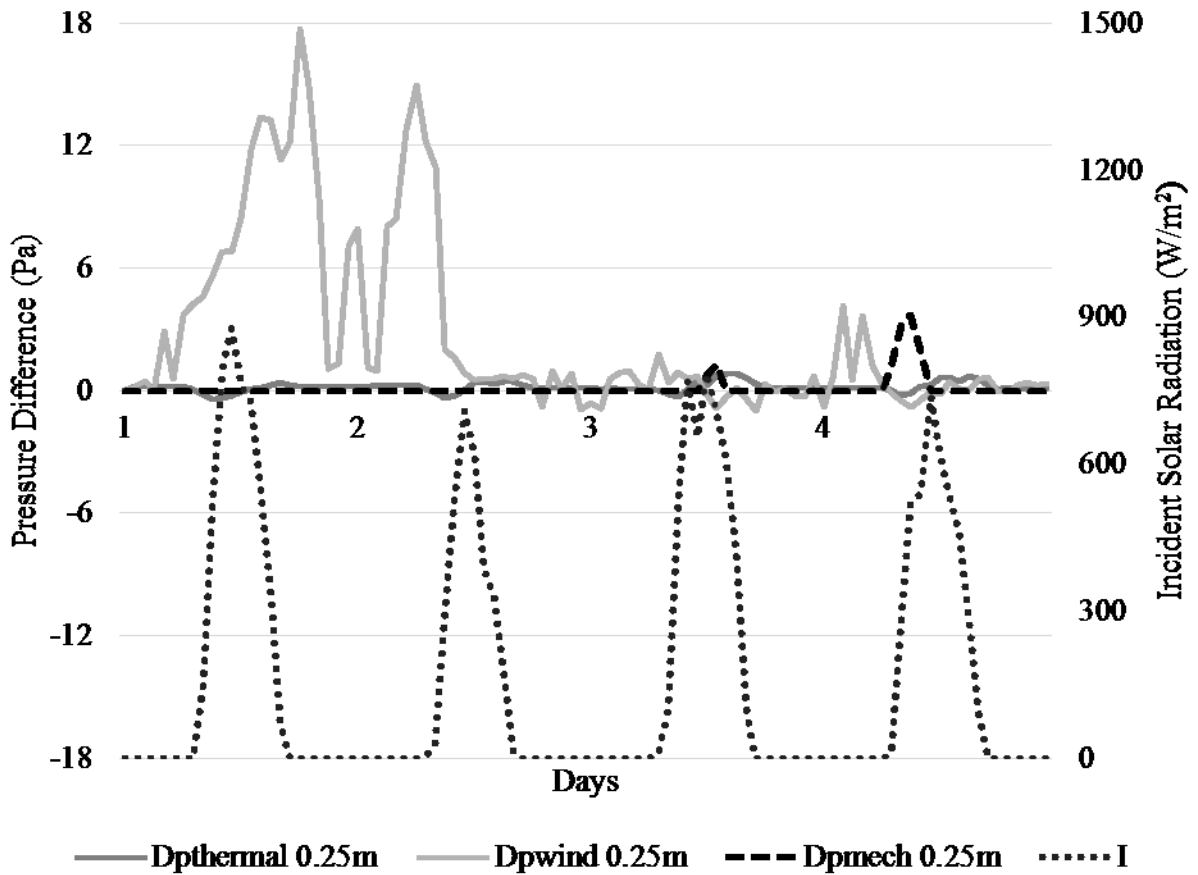


Figure 4.7: Thermal, wind and mechanical pressure drop within the cavity for the case of $L=0.25\text{m}$ for four winter days

This can also be verified by the data of Figure 4.8, where the pressure drop by the fans ($D_{p\text{mech}}$) is lower for the case of the narrower cavity ($L=0.5\text{m}$) and from the data of Figure 4.9 where the pressure drop caused by the temperature difference ($D_{p\text{thermal}}$) is almost doubled in the case of the narrower cavity.

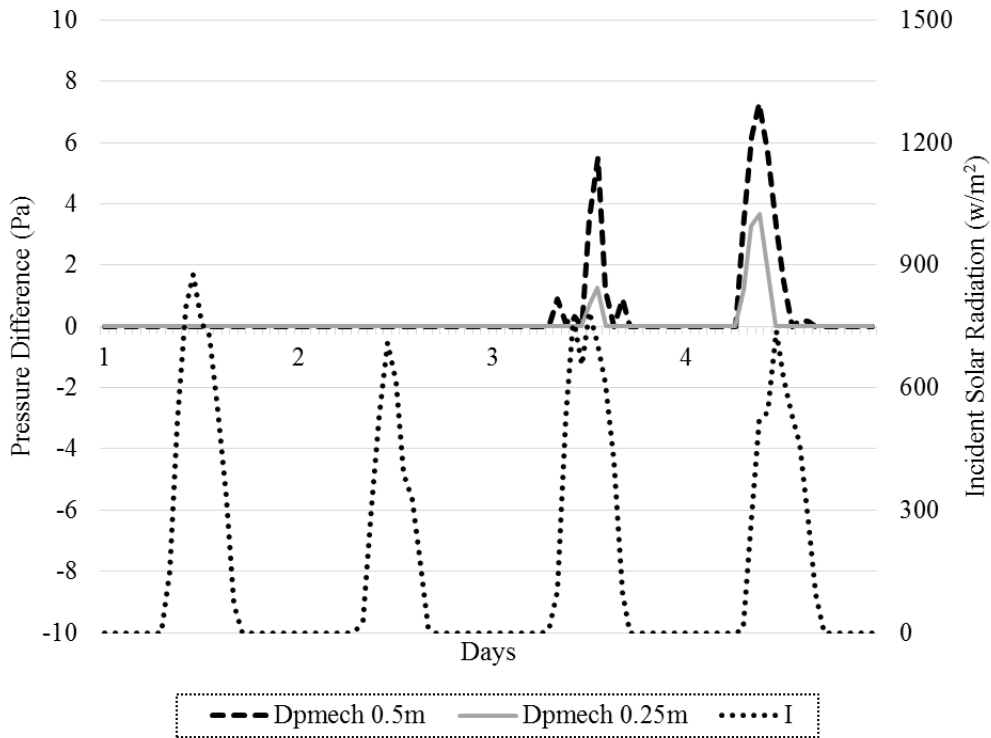


Figure 4.8: Comparison of the mechanical pressure drop for the two cases examined

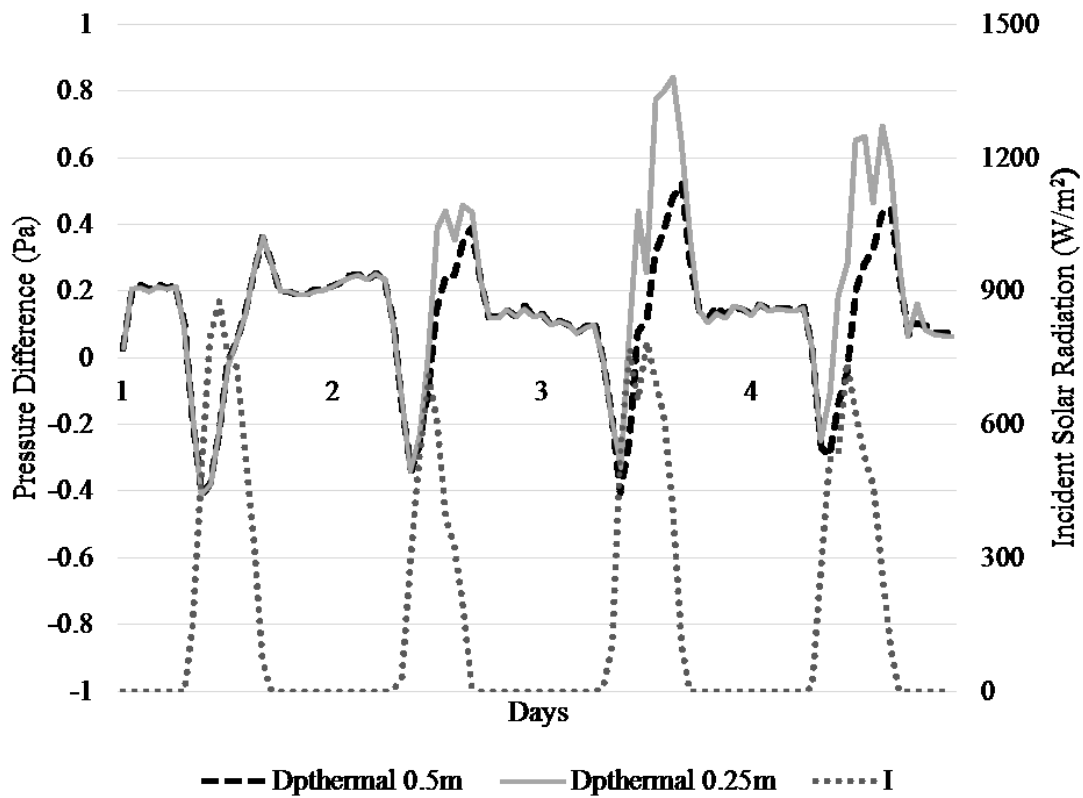


Figure 4.9: Comparison of the thermal pressure drop for the two cases examined

4.3 Annual Shading Effect

The shading provided by the photovoltaics and the roller blind has an impact on the thermal performance and daylight of the adjacent zone. This shading is a function of the position where the photovoltaics are integrated on the exterior skin, their transmittance and the area covered by the roller blind.

Following the three-section façade concept explained in section 3.4, the roller blind is implemented at the viewing section. This means that the roller blind starts directly underneath the semi-transparent photovoltaics integrated at the exterior skin and can expand till the spandrel section. The roller blind can extend along the viewing section (Figure 4.10). In this way, the daylight section is always unshaded by the roller blind. However, depending on the solar altitude, it is shaded either from the semi-transparent photovoltaics on the exterior skin, or from the opaque photovoltaics on the spandrel section of the floor above.

A case of a three-story DSF-P is simulated taking into consideration the shading effect of the exterior skin and the roller blind to the interior skin. More precisely, four different cases with four different heights of the roller blind and one case without the roller blind are simulated.

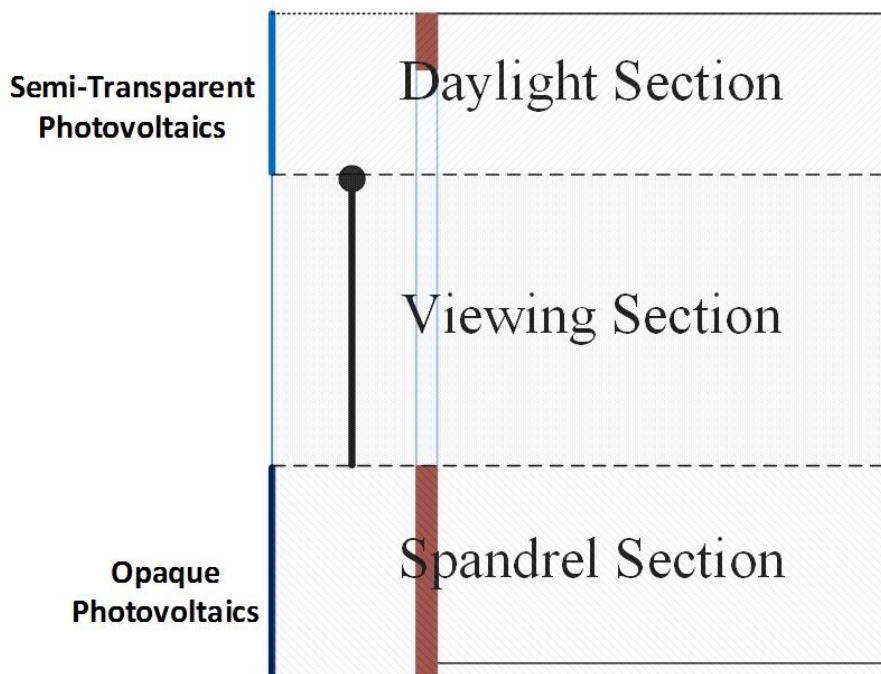


Figure 4.10: Three section façade

The way that the top floor is simulated is different from the way that the bottom two floors are simulated. The top floor takes also into account the shading from the top of the DSF-P. During the summer months, when the sun position is high in the dome, sun light passes through the top floor and is transmitted at the interior skin of the floor underneath.

The four shading cases are 25%, 50%, 75% and 100% of the viewing section covered by the roller blind and the fifth one is where no roller blind is simulated at the interior of the cavity of the DSF-P is the (0%) (Appendix C).

The simulated heights of the roller blind H_{rol} is at the 25%, 50% 75% and 100% of the maximum height that the roller blind can have, which is the height of the viewing section H_g .

For all the five different cases of shading, the results for a top and a middle floor will be presented as well as their combination to form a three-story DSF-P.

4.3.1 Annual incident solar radiation on the interior skin

Shading from the cup of the DSF-P

Light passes though the floor above

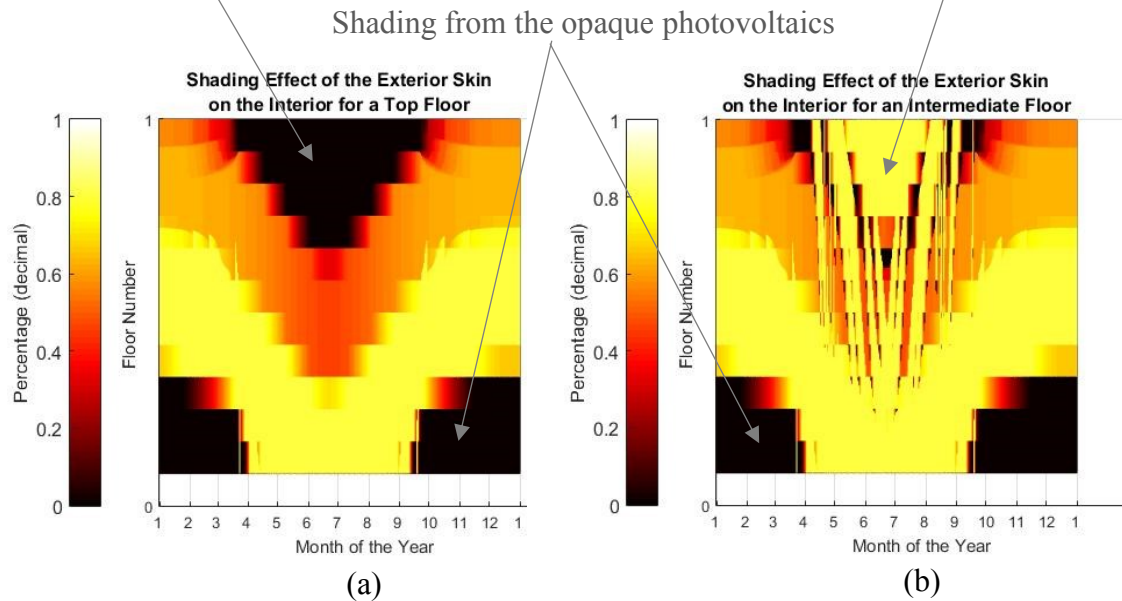


Figure 4.11: Shading of the exterior skin on the interior for a top (a) and a middle floor (b)

The percentage of the shading provided by the exterior skin to the interior one are shown in Figures 4.11 (a) and (b) for a top and an intermediate floor respectively. The difference between a top and an intermediate floor can be seen at the top of all the figures presented in this chapter, where in the case of the top floor, the top of the DSF-P shades the interior skin, while in the case of the

intermediate floor, light from the floor above lights the envelope of the building. It can be seen that these phenomenon is observed during the summer months where the sun position is higher. At the lower side of the figures, the dark area represents the shading that is provided to the building by the opaque photovoltaics integrated on the spandrel position of the exterior skin.

By combining the top and the intermediate floor, the incident solar radiation on the interior skin is presented in Figure 4.12. The area of the interior skin, where the window is placed, can reach more than 700W/m^2 during the winter months, while during the summer months these areas are shaded and the incident solar radiation reaches up to 400W/m^2 .

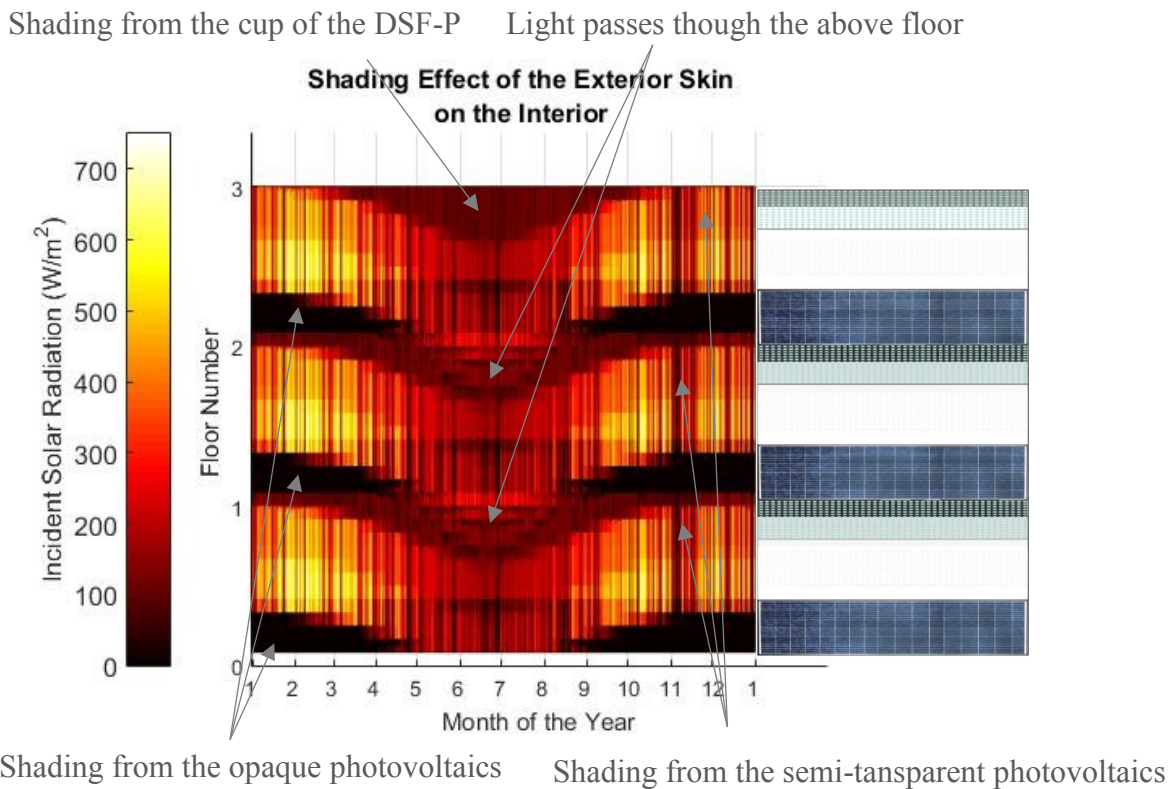


Figure 4.12: Shading effects of different elements integrated on the exterior skin

The other cases of 25%, 50%, 75% and 100% are presented in Appendix C. The darker area at the middle of each floor is the shade provided by the shading device.

4.4 Annual Energy Consumption

The energy consumption of DSF-P system and the adjacent to it zone consists of five different electricity consumptions, namely for heating and cooling, for fans within the cavity, for lighting within the room and for plug loads. The heating and cooling load of the adjacent zone depend on

many parameters such as the temperature of the air within the cavity, the cavity width, the shading provided by the roller blind and photovoltaics etc. On the contrary, the energy consumption by the fans depends mainly on the cavity width and the wind effects and the energy consumption for the lighting depends on the existence of roller blind, its transmittance and the transmittance of the semi-transparent photovoltaics. For this reason, these parameters are examined separately and are presented in the next chapters.

4.4.1 Energy consumption by the fans

4.4.1.1 Effect of the wind velocity and direction on the operation of the fans

In order to explain the behavior of the velocity within the cavity and the impact that the wind and the buoyance effects have on it, an annual analysis of the wind velocity and direction was held. Two different widths of the DSF-P cavity ($L=0.25\text{m}$ and $L=0.5\text{m}$) have been examined and Strategy #4 was used for this set of simulations with a velocity set-point of 0.5m/s . In Strategy #4, hybrid ventilation during the day and natural ventilation during the night is the strategy that was chosen in order to make more visible the fluctuation of the air-velocity inside the cavity due to the wind and buoyancy effects. The two different cavity widths selected are representative of DSFs with a narrow and a wide, in which people cannot and can walk in them respectively.

The number of times that the velocity of the air inside the cavity exceeds the velocity set-point, is presented in Figure 4.13. The simulation results are clustered into five groups depending on the wind direction. It must be noted that the wind direction angles start from 0° on the south to 180° or -180° depending on the direction.

It can be seen that the number of times that the wind and buoyancy effects are enough to drive the air and reach the velocity set-point is more than 4 times greater in the case of the narrower cavity ($L=0.25\text{m}$) than in the wider one ($L=0.5\text{m}$). On the same graph, the average velocity of the wind at each cluster is presented.

For the case of $L=0.5\text{m}$, the required wind velocity starts from approximately 7.5m/s for windward directions and can go up to 11m/s for leeward directions. On the other hand, this velocity is reduced by 24%, up to 46% for the cases of $L=0.25\text{m}$. It is also important to notice that even for the cases that the wind is leeward and for the case with the smaller cavity width, the velocity of the air inside the cavity exceeds the velocity set-point up to 50 more frequent than in the case of the wider cavity.

These results are in an agreement with the weekly results presented in Figure 4.6 in section 4.2.3.1 where the velocity of the air within the cavity was not always following the same pattern with the wind velocity.

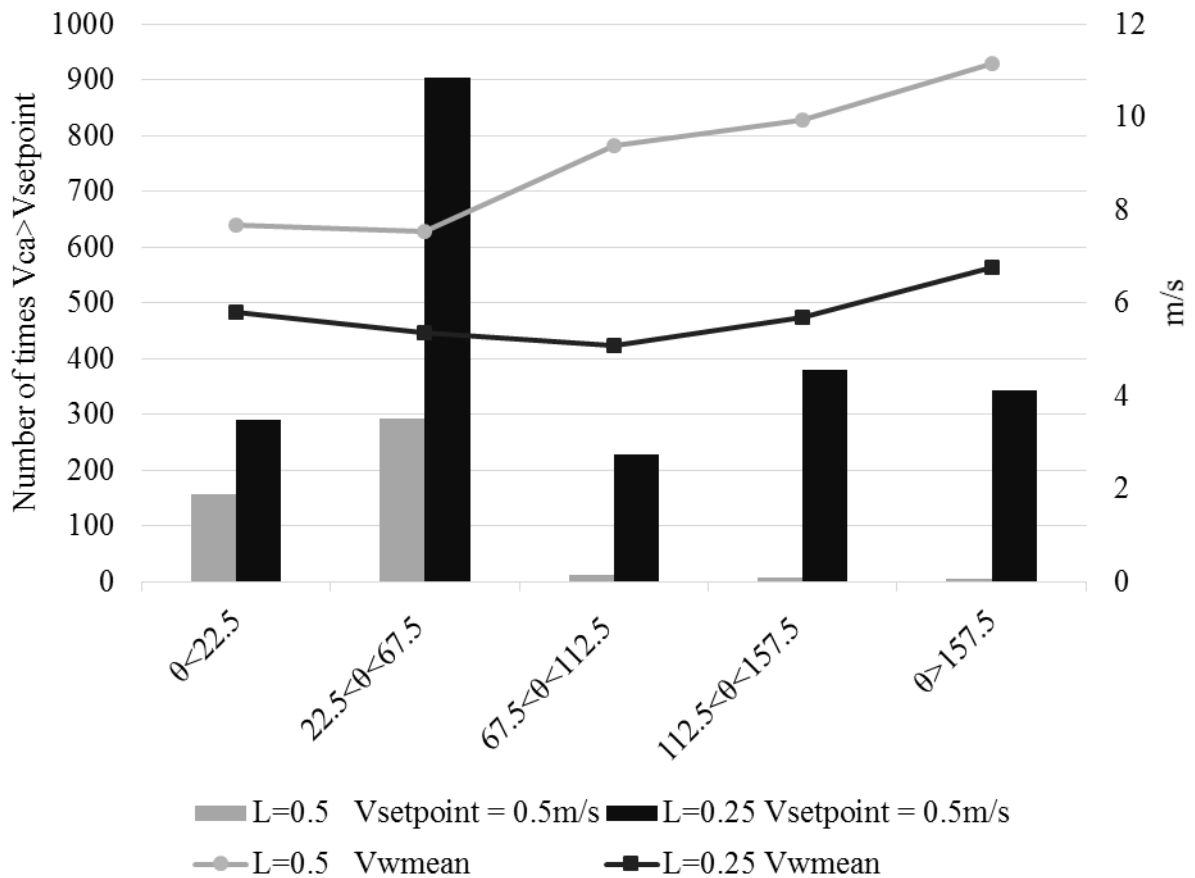


Figure 4.13: Wind direction and velocity distribution for which the velocity of the air within the cavity reaches the set-point without the assistance of a fan for 0.25m and 0.50m cavity widths

Table 4.1: Number of times and average wind velocities for which the velocity of the air within the cavity reaches the set-point without the assistance of a fan for 0.25m and 0.50m cavity widths (m/s)

	$0 < \theta < 22.5^\circ$	$22.5^\circ < \theta < 67.5^\circ$	$67.5^\circ < \theta < 112.5^\circ$	$112.5^\circ < \theta < 157.5^\circ$	$\theta > 157.5^\circ$
L=0.50m $V_{setpoint}=0.5\text{m/s}$	157	292	12	7	6
L=0.25m $V_{setpoint}=0.5\text{m/s}$	291	905	229	380	343
L=0.50m V_{wmean} (m/s)	7.68	7.54	9.38	9.94	11.15
L=0.25m V_{wmean} (m/s)	5.81	5.36	5.09	5.70	6.76

The maximum and minimum air velocities for which the velocity of the air inside the cavity exceeds the set-point are presented in Table 4.2. For the case with the narrower cavity, it can be seen that the even for low wind velocities and for all the wind directions, the velocity set-point is reached. For this it can be concluded that the buoyancy effects are stronger in the cases with smaller cavities.

Table 4.2: Maximum and minimum wind velocities for which the velocity of the air within the cavity reaches the set-point without the assistance of a fan for 0.25m and 0.50m cavity widths (m/s)

		$\theta < 22.5^\circ$	$22.5^\circ < \theta < 67.5^\circ$	$67.5^\circ < \theta < 112.5^\circ$	$112.5^\circ < \theta < 157.5^\circ$	$\theta > 157.5^\circ$
max	L=0.5m	14.70	14.10	14.00	12.00	12.20
	L=0.25m	14.70	14.10	14.70	13.70	12.90
min	L=0.5m	4.75	4.75	6.30	8.60	10.20
	L=0.25m	1.70	0.45	0.35	0.20	0.30

4.4.1.2 Electricity consumption by the fans

An important fraction of the electricity consumption comes from the operation of the fans that assist the flow inside the cavity. For this reason a parametric analysis with two different cavity widths (L=0.25m and L=0.5m) and three different velocity set points (V=0.5m/s, V=1m/s and V=1.5m/s) is presented. Also two strategy #1 and strategy #4 are compared. In strategy #1, the velocity inside the cavity is always assisted by the fan in order to reach the velocity set-point while the fans are not operating during the night in strategy #4.

The power of the fans is calculated using the equation:

$$P_{fan} = \frac{\dot{m}\Delta P_{mech}}{n_{fan}} \quad (47)$$

Comparing the two strategies, the difference on the fan consumption is around 40% to 45% as it can be seen in Table 4.3. It can also be seen that a smaller cavity can reduce the energy consumption by the fans, between 75% and 90% for each strategy.

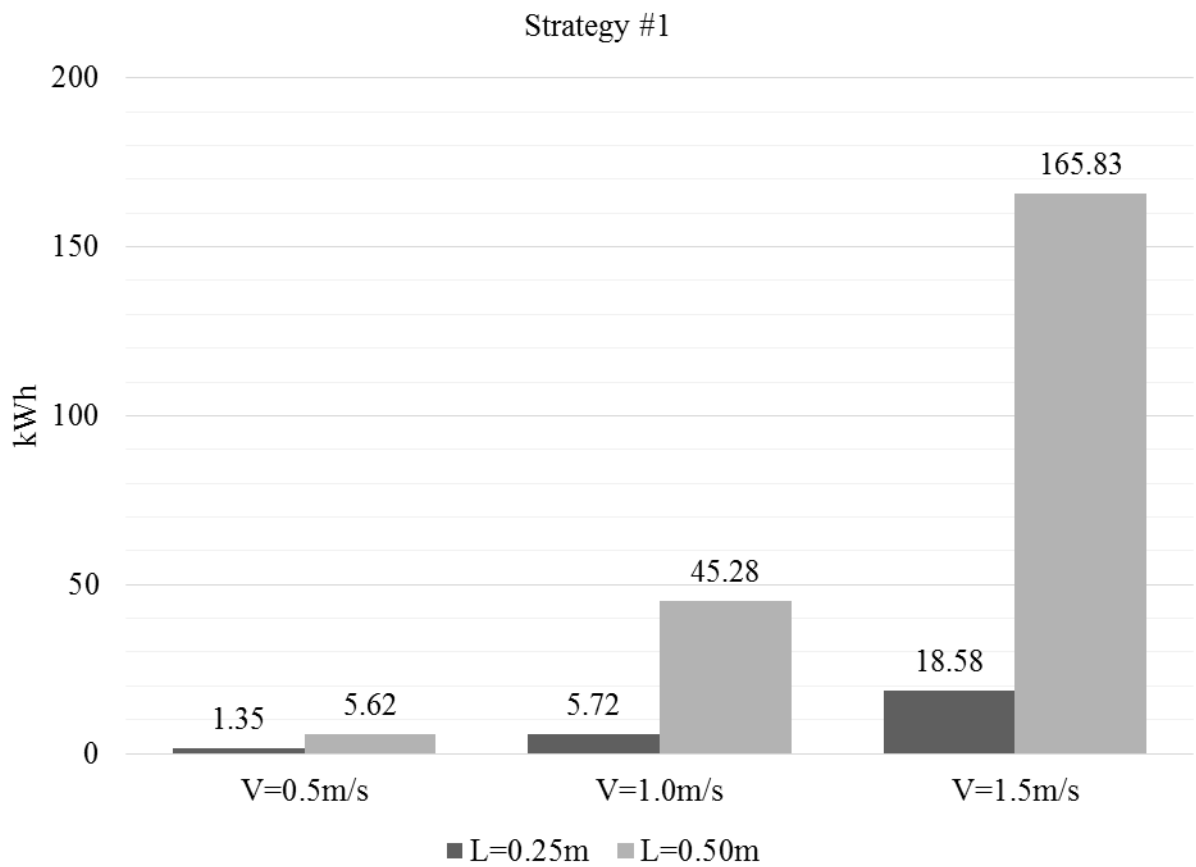


Figure 4.14: Electricity consumption by the fans for different cavity widths and velocities for strategy #1

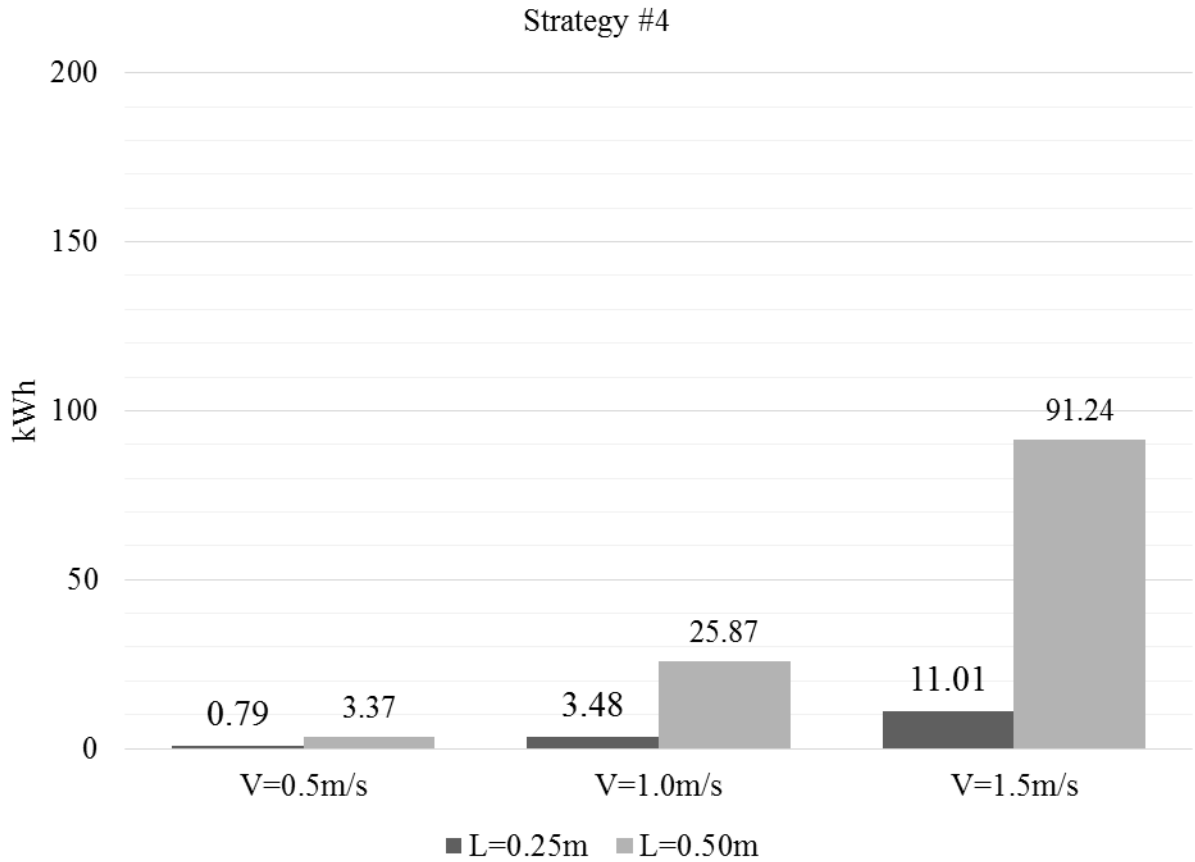


Figure 4.15: Electricity consumption by the fans for different cavity widths and velocities for strategy #4

Table 4.3: Electricity consumption by the fans for different cavity widths and velocities for strategy #1 and strategy #4 (kWh)

	Strategy #1			Strategy #4			Differences %	
	L=0.25m	L=0.50m	%	L=0.25m	L=0.50m	%	L=0.25m	L=0.50m
V=0.5m/s	1.35	5.62	0.76	0.79	3.37	0.77	0.41	0.40
V=1.0m/s	5.72	45.28	0.87	3.48	25.87	0.87	0.39	0.43
V=1.5m/s	18.58	165.83	0.89	11.01	91.24	0.88	0.41	0.45

4.4.2 Energy Consumption for Lighting

4.4.2.1 Daylight calculation

The simple daylight modeling developed and explained in section 3.5 is used to assess the illuminance levels on the work-plan. Then the energy consumed in order to artificially light the work-plane with lamps is calculated and compared for the different cases examined.

The simulations are held for year in Montreal and for five different shading configurations as explained in the previous paragraph. One without a shading device implemented within the cavity and four with different heights of the roller blind. Only a comparison between these cases is presented in this chapter and the rest are in the Appendix D.

The configuration factors are calculated for five different points on the y-axis of the room Figure 4.12. The points are facing upwards, are placed on the level of the work-plane and are equally spaced at a distance of 1.37m starting to count from the window.

The illuminance at these points is simulated for all days throughout a year. The simulated results are used in order to predict the daylight autonomy of each point. The daylight autonomy is defined as the percentage of the annual daytime hours that the point is above a specific level. The levels used for this study is 200lx, 300lx, 400lx and 500lx. Also for the daytime hours, the monthly average illuminance on these points is presented.

Results only for the first six months of the year are presented due to the fact that the rest months behave in a similar way.

Table 4.4: Illuminance Categories as described by IESNA (Illuminating Engineering Society of North America)

Working spaces where simple visual tasks are performed	100lx
Performance of visual tasks of high contrast and large size	300lx
Performance of visual tasks of high contrast and small size, or visual tasks of low contrast and large size	500lx

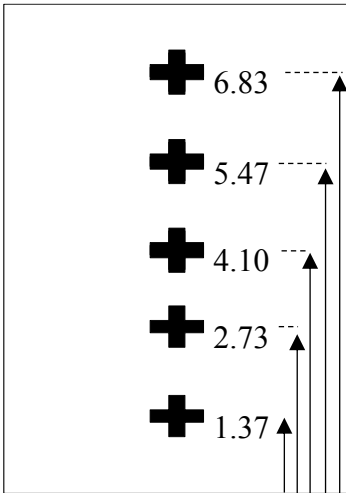


Figure 4.16: Points for which illuminance levels are calculated and their distance from the window

4.4.2.2 Daylight Simulation Comparison

A comparison between the average illuminance levels for January for the different shading cases examined is presented in Figure 4.17. The difference between the 0% and 25% shading cases is the highest difference observed, presenting a difference of 3,000lx. It can also be seen that the cases of 75% and 100% shading result into similar illuminance levels. This is because the majority of the direct solar radiation is already blocked and this small difference is the result of the 25% of the unshaded area. The fact that should also be noted is that even when the roller blind is fully extended (100% shading) the average illuminance for January is around 5,000lx.

For the summer case and most specific for June, it is observed that the existence of the roller blind is not a decisive parameter. From no shading (0%) to fully shaded (100%) the difference is around 1000lx. The illuminance levels are lower than those in the cases of the winter months and this is because of the design of the STPV. The STPV integrated on the exterior skin is designed i to block the direct solar radiation and prevent solar gains to penetrate the room during the summer months. For this reason, the difference between the 0% shading and 100% shading is only the diffuse solar radiation by the roller blind.

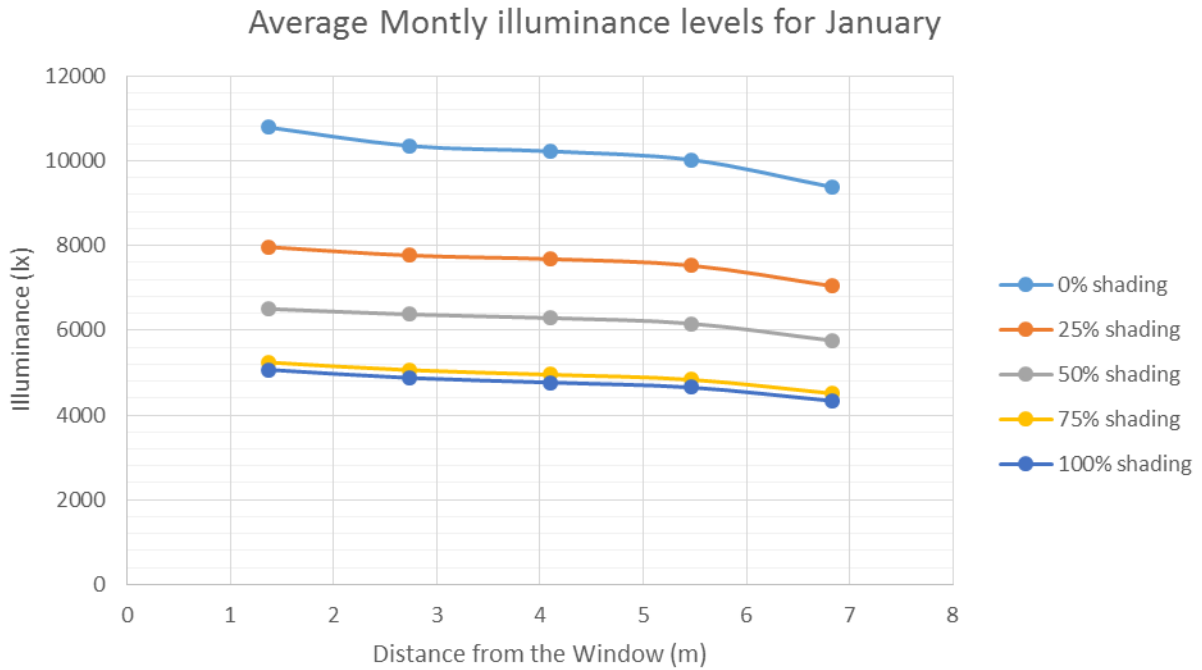


Figure 4.17: Average illuminance inside the room for January

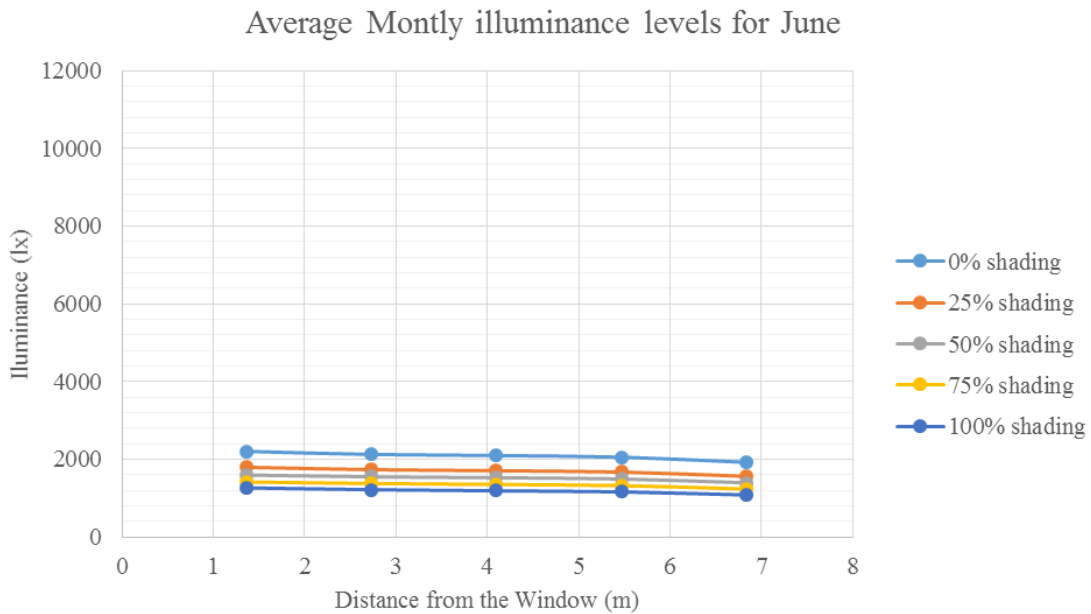


Figure 4.18: Average illuminance inside the room for June

The daylight autonomy at 300lx decreases from 77% to 72% at the cases of 0% shading to 100% shading respectively. A typical illuminance (300lx) for office applications can be reached on an

average of 75% of the day-time. The design of the STPV integrated on the exterior skin to act as an overhang and therefore block a big percentage of the direct solar radiation and allow a smaller percentage of daylight to penetrate the room and therefore contributes a lot at the daylight autonomy of the room.

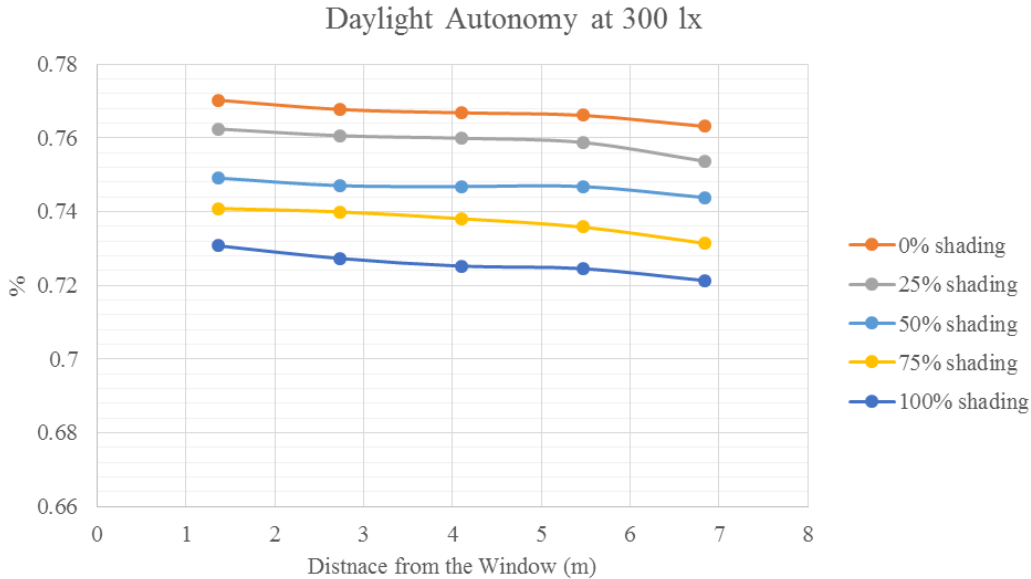


Figure 4.19: Daylight autonomy at 300lx for all the different shading configurations

4.4.2.3 Annual electricity consumption for lighting

For the cases examined the electricity consumption for the lights on the room is presented in Figure 4.20. The lights are assumed to be switched-on when the daylight is not adequate to provide 500lux on the work-plane and only for the hours between 8am and 6pm. The luminous efficacy of the lamps is assumed to be 100lm/W.

Two different cases are presented, with two different types of roller blinds. One case with a roller blind of high transmittance ($\alpha_{rol}=0.1$, $\tau_{rol}=0.4$) and one with a roller blind of high absorbance ($\alpha_{rol}=0.5$, $\tau_{rol}=0.1$)

The implementation of a roller blind within the cavity may result in a 15.9% more electrical energy need in order to light the interior space. For this reason control strategies for movement of the roller blind should be developed in order to reduce the energy consumption for the lights but at the same time to take advantage of the solar heat gains.

Table 4.5: Comparison of the energies consumed for artificial lighting the work-plane for different shading configurations

	Energy Consumption Increase (%)	
	$\alpha_{rol}=0.1, \tau_{rol}=0.4$	$\alpha_{rol}=0.5, \tau_{rol}=0.1$
25% shading and 0% shading	2.6	2.6
50% shading and 0% shading	9.8	15.9
75% shading and 0% shading	11.9	22.9
100% shading and 0% shading	15.9	33.9

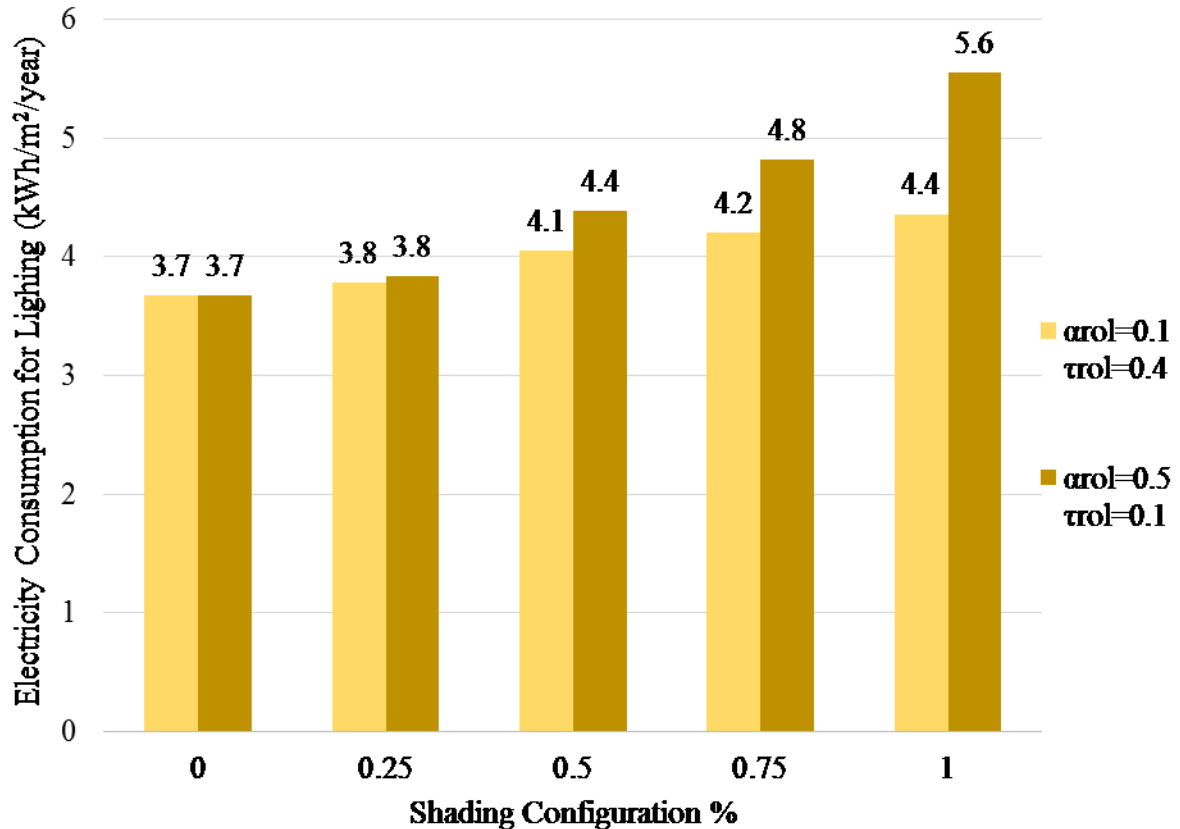


Figure 4.20: Electricity consumed to light the work plane at 500lux for a year for the different shading configurations

4.5 Parametric analysis

The previous sections have underlined the significance of the different parameters for the energy consumption of the DSF-P system. These parameters are the cavity width, the airflow within the cavity, the semi-transparent photovoltaic transmittance, the existence of a roller blind within the cavity and the transmittance caused by these blinds. For this reason a parametric analysis was held. The differences between the energy consumption and generation for the simulated cases were found.

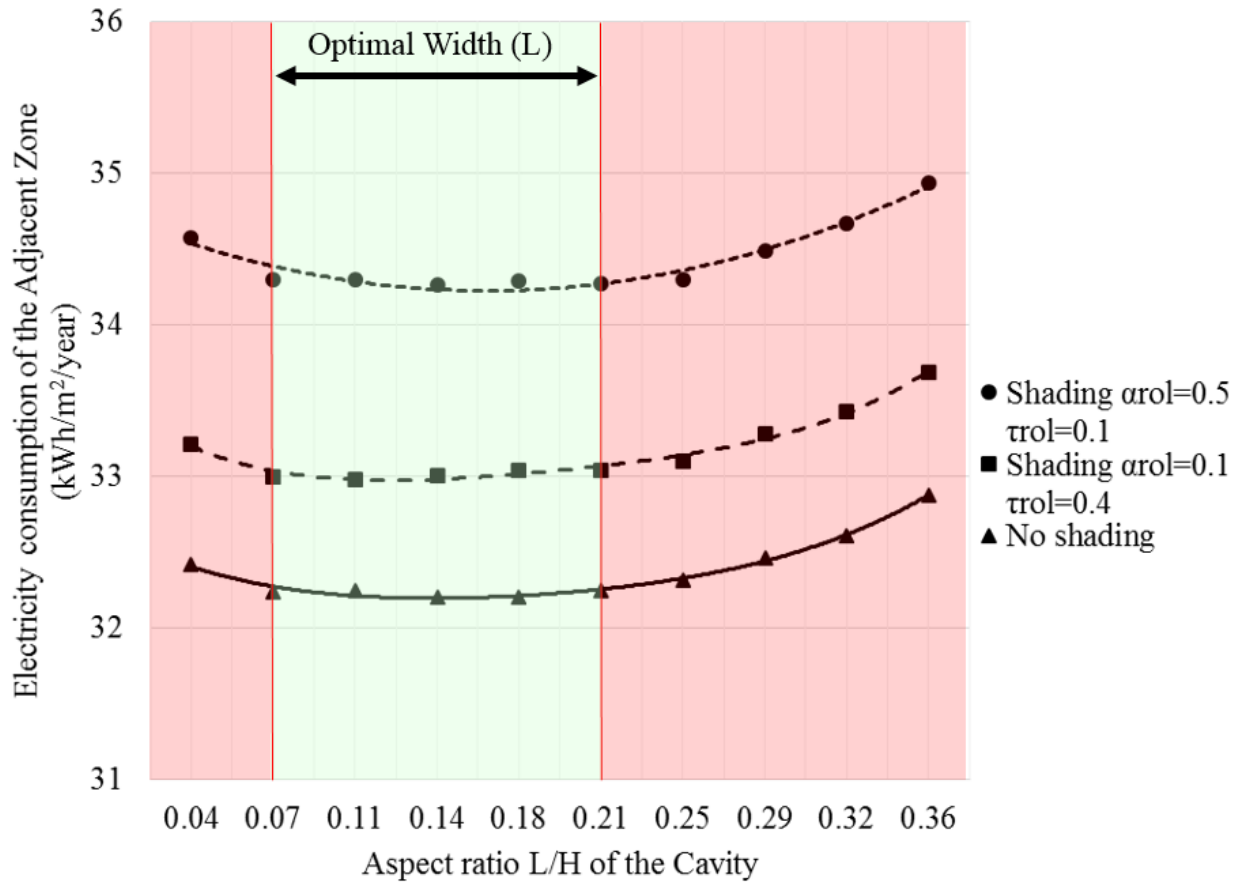


Figure 4.21: Electricity consumption of the DSF-P system for different shading configurations for different cavity aspect ratios

Table 4.6: Equivalence between the cavity width and the aspect ratio for a 2.8m high floor

L:	0.1m	0.2m	0.3m	0.4m	0.5m	0.6m	0.7m	0.8m	0.9m	1.0m
Aspect Ratio:	0.04	0.07	0.11	0.14	0.18	0.21	0.25	0.29	0.32	0.36

Figure 4.21 shows a comparison of electricity consumption for cases with and without shading devices. For the case where a roller blind is simulated within the DSF-P cavity, two different roller blind absorbances and transmittances were assumed. The one is a low absorptive ($\alpha_{rol}=0.1$) and has high transmittance ($\tau_{rol}=0.4$) roller blind and the other case presents a high absorptive ($\alpha_{rol}=0.5$) and has low transmittance ($\tau_{rol}=0.1$) roller blind. The total energy consumption of the room adjacent to the DSF-P is calculated and presented for different cavity widths. The aspect ratio (L/W) the width over height of the cavity is used for this comparison. For the case simulated,

the DSF-P has a height of 2.8m so the equivalence between the cavity width and the aspect ratio is presented on Table 4.6. The velocity set-point is assumed to be 0.5m/s.

All the cases presented follow the same pattern, presenting the lowest energy consumption between 0.2m and 0.6m. For smaller cavities, the heating and cooling loads increases and for this reason the energy consumption increases. As the cavity gets wider, the electricity consumption of the fans in order to maintain the velocity of the air at a certain point also increases resulting into an increased energy consumption. For the climate examined (cold climate, Montreal, Canada) the case without a shading devise is preferred or the roller blind with higher transmittance. Although taking into consideration that Montreal is a heating dominated region, cannot be concluded that no shading device should be implemented within the cavity but a high transmittance roller blind should be preferred. For the case without a shading device implemented within the cavity, the impact that the velocity set-point has on the energy consumption for different cavity widths is presented in Figure 4.22.

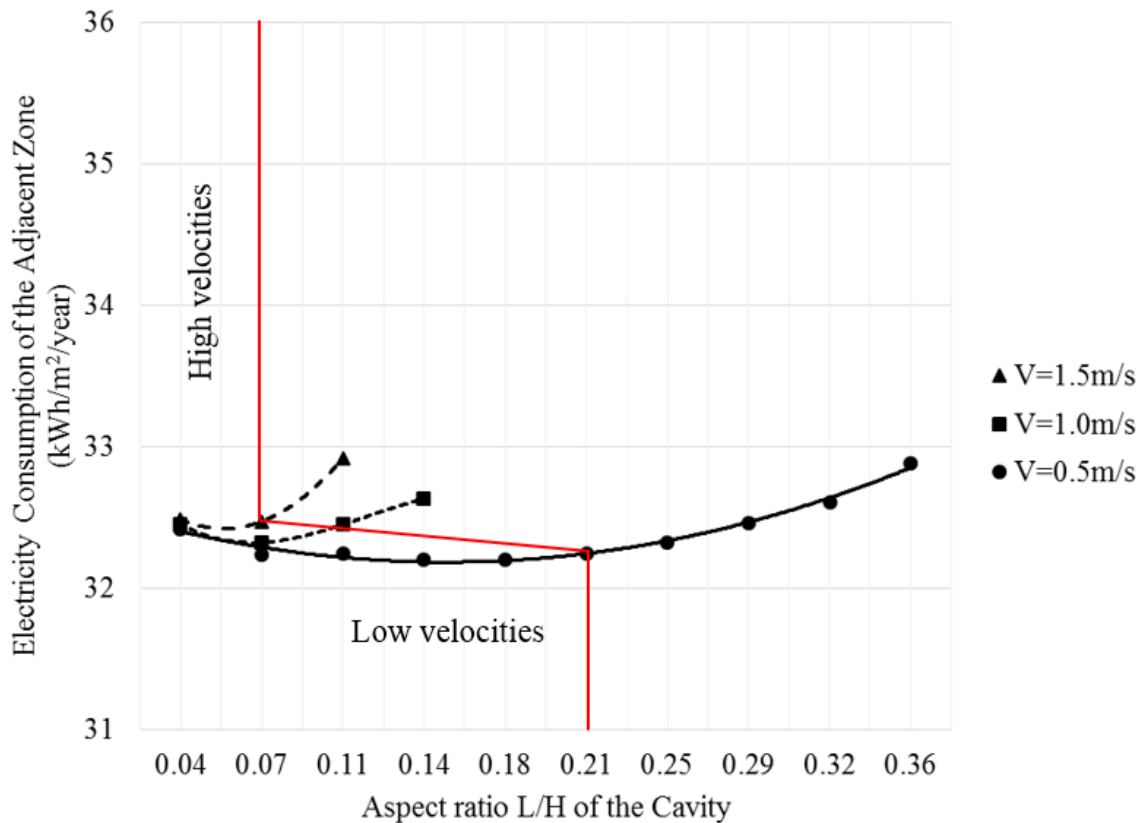


Figure 4.22: Electricity consumption of the DSF-P system for different velocity set-points for different cavity aspect ratios

For narrow cavities, the air velocity within the cavity does not affect the energy consumption of the DSF-P system. On the contrary, for wider cavities the electricity consumption of the system increases because the electricity consumption for the fans also increases. For the lower velocities though, because the airflow within the cavity is assisted by the buoyancy and wind effects the energy consumption does not increase drastically as the cavity width increases.

For this reason, two representative cases of narrow cavities ($L=0.2\text{m}$ and 0.4m) with aspect ratios of 0.07 and 0.14 are presented and the energy consumption of the DSF-P system is compared for four different air velocities within the cavity. At the same graph the cases of a high transmittance and a high absorbance roller blind along with the cases without a roller blind are presented.

As also shown in Figure 4.21, the façade configurations that allow higher transmittance of solar gains are preferred for the cold climate of Canada. For all the cases examined it can be observed that the energy consumption of the DSF-P system is the same for two different cavity widths simulated for air velocities around 0.5m/s . This is happening because for velocities set-points lower than 0.5m/s the fans are consuming very little while as the velocity set-point increases, the fan consumption increases too. For the part of the Figure 4.23 on the left of the 0.5m/s , this small energy difference is explained by the small difference on the heating, cooling and daylighting electricity consumption.

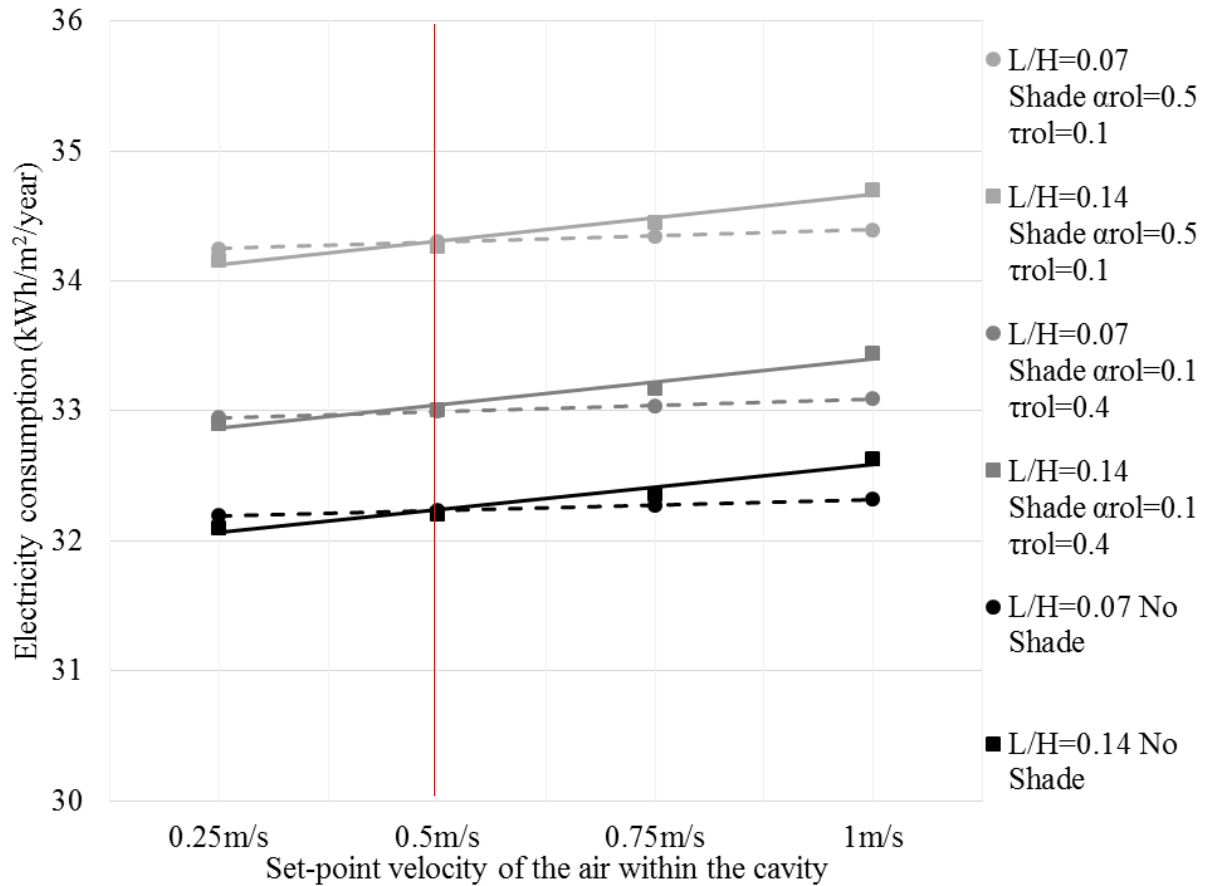


Figure 4.23: Electricity consumption of the DSF-P system for different cavity aspect ratios with different shading configurations and different velocity set-points.

4.6 Energy Balance

The electricity consumption of the adjacent zone consists of five different parameters; the electricity consumed to heat or cool the adjacent room, the electricity consumed for the lights, for the fan implemented at the top of the cavity and for the appliances. It is assumed that the plug load factor is 3.55W/m^2 for a 12.5m^2 of workstation, while all the occupants use notebooks and one printer is assigned for every ten occupants (Wilkins and Hosni, 2011).

It should be noted that the airflow inside the cavity is assisted by a fan in order to reach the velocity set-point. Here the two representative cases of a narrow ($L=0.25\text{m}$) and a wider ($L=0.50\text{m}$) cavity are presented and the velocity in which they present the same energy consumption ($V=0.5\text{m/s}$) is used for the parametric analysis.

The energy balance between the electricity consumption and generation of the photovoltaics is presented for different semi-transparent photovoltaics transmittances (0.3, 0.5 and 0.7) and for different zone areas. It must be noted that the area that the photovoltaics are integrated is the same, and the width of the façade does not change. It should also be noted that the cell efficiency of the integrated photovoltaics is assumed to be 20% and the area of the façade is 10.08m² while the area covered by the photovoltaics is more than 55% of the façade area.

The only parameter that changes in this analysis is the length of the room. In this way, as the length of the room increases, the energy consumption for the daylighting increases as well as the electricity consumption for the appliances the heating and the cooling of the room.

It should also be noted that the amount of electricity needed for the operation of the fan of the heat pump is calculated and added each time to the heating or cooling demand, depending in which cycle the heat pump is operating.

In Figure 4.24, the energy balance per square meter per year is presented for different room areas. It can be seen that positive or net-zero energy adjacent zone can be achieved for floor areas up to 2.7 and 3.5 times larger than the exterior skin surface area for integrated semi-transparent photovoltaics with transmittances of 30% and 70% respectively.

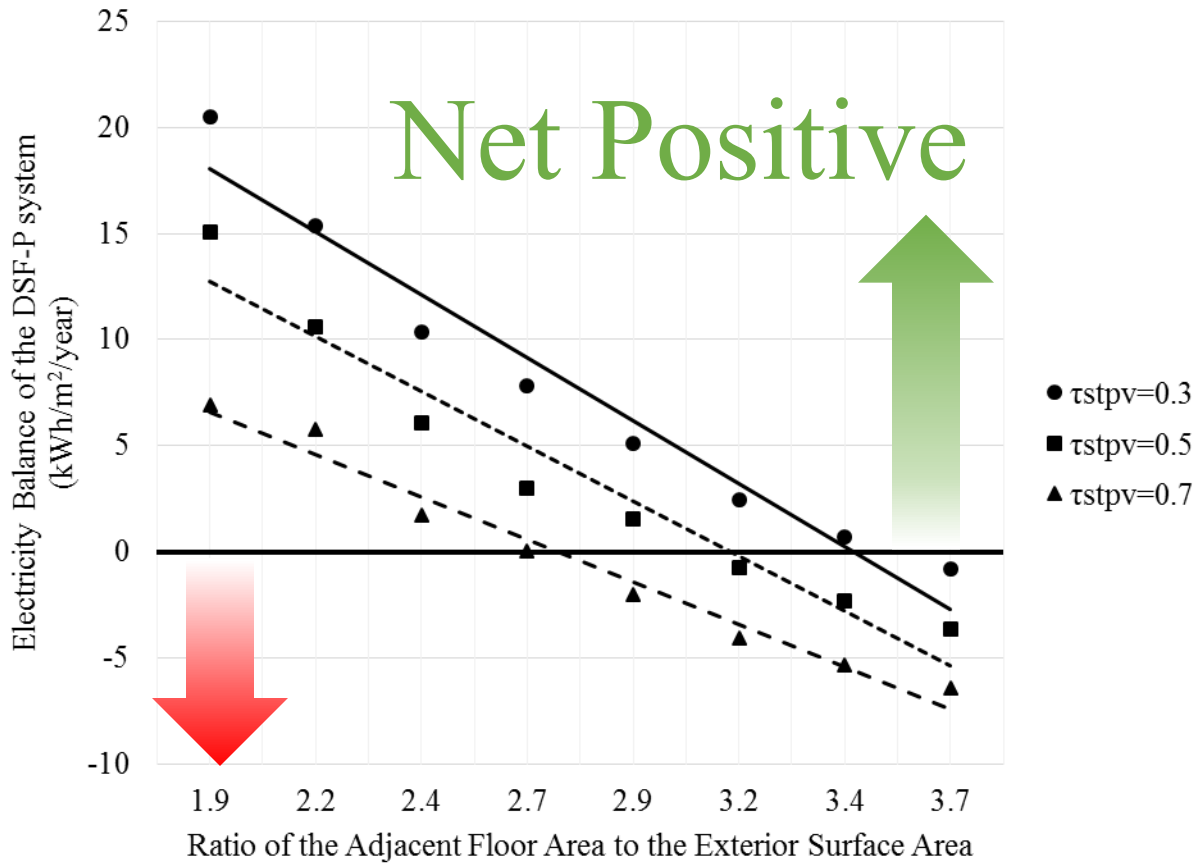


Figure 4.24: Electricity balance of the DSF-P system for different STPV transmittances for different zone areas for a narrow cavity ($L=0.25\text{m}$)

The case in Figure 4.25 follows the same pattern with the Figure 4.24. It presents the electricity balance for the case of the wider cavity ($L=0.5\text{m}$) for the different transmittances of the photovoltaics. It can be seen that the zone areas that net-zero DSF-P is achieved is slightly decreased.

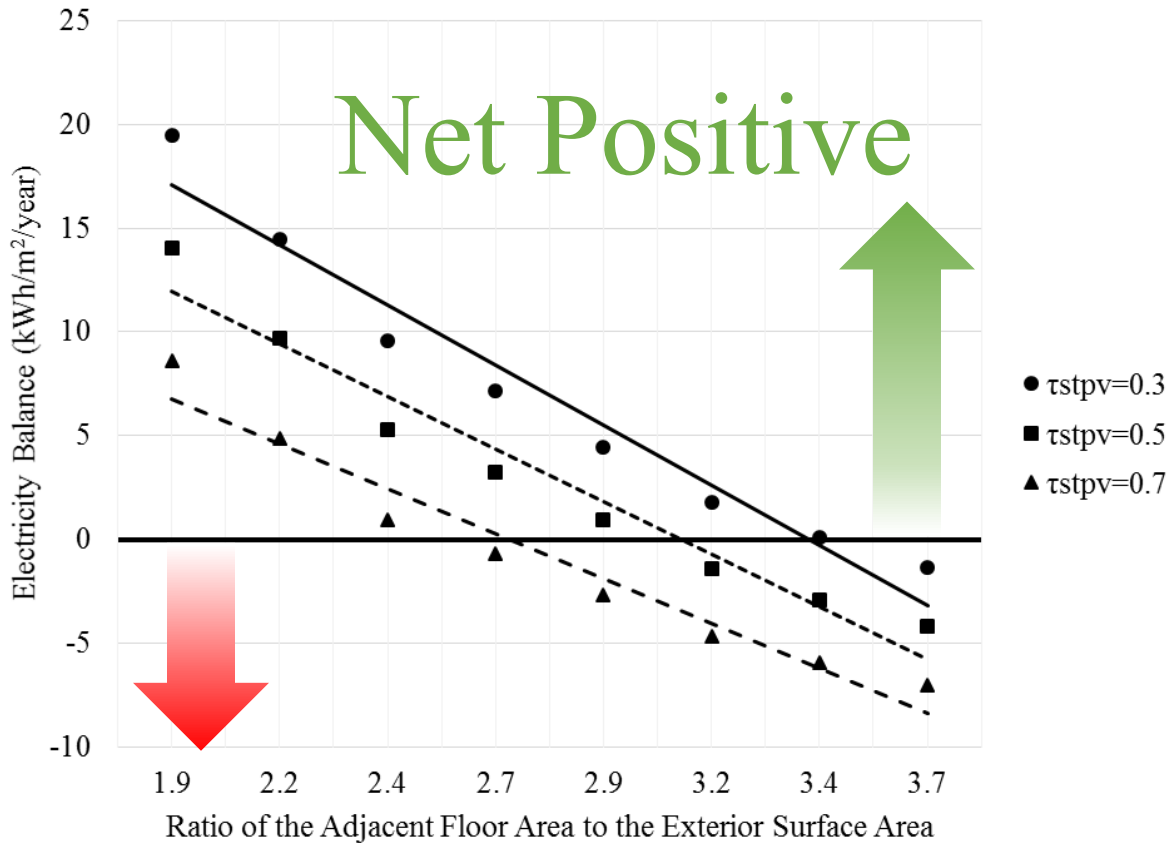


Figure 4.25: Electricity balance of the DSF-P system for different STPV transmittances for different zone areas for a narrow cavity ($L=0.50\text{m}$)

4.6.1 Energy Balance and Consumption by Parameters

For one of the simulated cases, which is also indicative of the rest cases examined, the electricity consumption by the different parameters is presented in Table 4.7.

Table 4.7: Electricity consumption of the DSF-P and the adjacent room for a year

	kWh/year
	V=0.5m/s 0% shading
Heating	298.91
Cooling	120.16
Lamps	112.29
Fan	3.42
Appliances	420.76
Total Electricity Consumption	955.54

Electricity Consumption

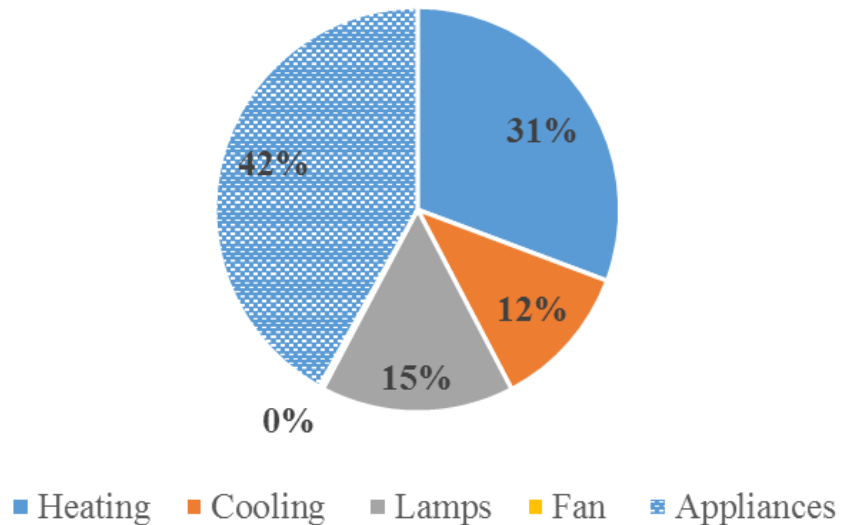


Figure 4.26: Electricity consumption of the DSF-P and the adjacent room for the case of $V=0.5\text{m/s}$ and with 0% shading

It can be seen that the largest consumption of electricity comes from the appliances and the heating demand. More than 910kWh/year are generated from the photovoltaics integrated on a 10.08m^2 façade if a module efficiency of 15% is assumed and more than 1230kWh/year are generated if a module efficiency of 20% is assumed. This amount of electricity covers from 84% to 130% of the total electricity consumed at the DSF-P and its interior room (area of 29.52m^2).

It should be noted that the overall energy balance, throughout the year is positive for most of the cases examined and that the energy balance pattern for the different cases examined follow the same pattern; less energy consumption during the heating season for lower velocities and without a shading device and higher energy balance during the cooling season if the velocity inside the cavity increases and a shading device is used.

Chapter 5

5. Summary and Conclusions

5.0 Thesis Summary and Conclusions

This thesis presents the development of a mathematical model able to analyze and optimize the design of advanced DSFs integrating photovoltaics and roller blinds (DSF-P) for the first time. This innovative design increases the envelope area of buildings on which, photovoltaic panels can be integrated up to 60%.

The model is capable of assessing the potential that an innovative DSF-P has on the electrical, thermal and visual performance of the DSF-P. The mathematical model created can examine different operation strategies and perform parametric analyses for identifying the set of design and operating parameters which the performance of the DSF-P is optimized.

The simulations shown that the wind effects dominate in wider cavities than in narrower cavities, where the buoyancy effects increase. This result into an easier to be reached velocity set-point for a narrower cavity ($L=0.25\text{m}$) than in a wider one ($L=0.5\text{m}$). In this way, the energy consumption

by the fans decreases. In addition the appropriate strategy selected can reduce the energy demand by the fans, up to 90% depending on the velocity set-point and the cavity width.

A 75% shading is preferred (over 100%) as both cases present the same illuminance levels on the work plane but at the same time the one-fourth of the viewing section is not covered by a roller blind, giving the advantage to the occupants of more view to the outside.

This increase in the energy consumption by the fans also results into the increase of the energy consumption if the cavity is greater than 0.50m-0.60m depending on the air velocity set-point. On the other hand, cavities narrower than 0.2m increase the energy consumption of the DSF-P.

Finally more than 1230kWh/year are generated if a 20% photovoltaic cell efficiency is assumed and a 30% STPV transmittance is assumed. This amount of electricity covers up to 130% of the total electricity consumed at the DSF-P and its interior room (area of 29.52m²). In addition, a net-zero energy adjacent zone can be achieved for floor areas up to 2.7 and 3.5 times larger than the exterior skin surface area.

5.1 Contribution

A complete mathematical model is created that is capable of assessing the energy performance of a DSF integrating for the first time semi-transparent and opaque photovoltaics.

This model can be used for different:

- geometric characteristics of the DSF-P,
- integrating positions of the photovoltaics on the exterior skin,
- photovoltaic characteristics
- flow characteristics
- wind velocities
- wind directions
- interior façade designs
- interior room designs
- DSF-P orientations
- building locations

It is also capable of simulating multiple floor DSF-P.

In addition, the easiness in which the user can interact with the model make it possible to be used by everyone, not depending on his background and perform feasibility studies for the optimization of the performance of the DSF-P.

5.2 Future work

DSF integrating photovoltaics have not been extensively reviewed in the past. For this reason, a full scale experimental investigation of DSF-P should follow. This may also help with further validation of the model and further development of dimensionless correlations in order to assess the heat transfer coefficients within the cavity.

Further investigation and development of control strategies for the airflow inside the cavity and the shading provided by the roller blind should be held.

Also the illuminance levels on the work-plane should be measured and correlations between simple daylight models or advanced daylight simulation software (DAYSIM, RADIANCE, etc.) should be created.

Lastly, a model capable to simulate and assess the performance of a multi-storey DSF-P with multiple inlets should be developed.

References

- Andelkovic, A., Gvozdenc-Urosevic, B., Kljajic, M., Ignjatovic, M., 2015. Experimental research of the thermal characteristics of a multi-storey naturally ventilated double skin facade 86, 766–781.
- Andelković, A.S., Mujan, I., Dakić, S., 2016. Experimental validation of a EnergyPlus model: Application of a multi-storey naturally ventilated double skin façade. *Energy Build.* 118, 27–36.
- Asfour, O.S., Gadi, M.B., 2006. A comparison between CFD and Network models for predicting wind-driven ventilation in buildings. *Build. Environ.* 42, 4079–4085.
- Athienitis, A., O'Brien, W., 2015. *Modeling, Design, and Optimization of Net-Zero Energy Buildings.*
- Athienitis, A.K., 1998. *Building Thermal Analysis.* 1993 Math Soft, Inc.
- Athienitis, A.K., Bambara, J., O'Neill, B., Faille, J., 2010. A prototype photovoltaic/thermal system integrated with transpired collector. *ASHRAE Trans.* 117, 403–410.
- Balocco, C., 2002. A simple model to study ventilated facades energy performance. *Energy Build.* 34, 469–475.
- Barbosa, S., Ip, K., 2014. Perspectives of double skin façades for naturally ventilated buildings: A review. *Renew. Sustain. Energy Rev.* 40, 1019–1029.
- Blanco, J.M., Buruaga, A., Rojí, E., Cuadrado, J., Pelaz, B., 2016. Energy assessment and optimization of perforated metal sheet double skin façades through Design Builder; A case study in Spain. *Energy Build.* 111, 326–336.
- Chan, a. L.S., Chow, T.T., Fong, K.F., Lin, Z., 2009. Investigation on energy performance of double skin facade in Hong Kong. *Energy Build.* 41, 1135–1142.
- Charron, R., Athienitis, A.K., 2006. Optimization of the performance of double-façades with integrated photovoltaic panels and motorized blinds. *Sol. Energy* 80, 482–491.
- Chen, Y., Athienitis, a. K., Galal, K., 2010a. Modeling, design and thermal performance of a BIPV/T system thermally coupled with a ventilated concrete slab in a low energy solar house: Part 1, BIPV/T system and house energy concept. *Sol. Energy* 84, 1892–1907.
- Chen, Y., Galal, K., Athienitis, a. K., 2010b. Modeling, design and thermal performance of a BIPV/T system thermally coupled with a ventilated concrete slab in a low energy solar house: Part 2, ventilated concrete slab. *Sol. Energy* 84, 1908–1919.
- Coussirat, M., Guardo, a., Jou, E., Egusquiza, E., Cuerva, E., Alavedra, P., 2008. Performance and influence of numerical sub-models on the CFD simulation of free and forced convection in double-glazed ventilated faCades. *Energy Build.* 40, 1781–1789.
- De Gracia, A., Castell, A., Navarro, L., Oró, E., Cabeza, L.F., 2013. Numerical modelling of ventilated facades: A review. *Renew. Sustain. Energy Rev.* 22, 539–549.
- de Gracia, A., Navarro, L., Castell, A., Cabeza, L.F., 2015. Energy performance of a ventilated double skin facade

- with PCM under different climates. *Energy Build.* 91, 37–42.
- Design, I. of S.M., n.d. *faceworld* [WWW Document]. URL <https://facadeworld.com/2014/03/15/solarlux-nijverdal/> (accessed 1.1.16).
- Elarga, H., Goia, F., Zarrella, A., Dal Monte, A., Benini, E., 2016. Thermal and electrical performance of an integrated PV-PCM system in double skin façades: A numerical study. *Sol. Energy* 136, 112–124.
- Emmel, M.G., Abadie, M.O., Mendes, N., 2007. New external convective heat transfer coefficient correlations for isolated low-rise buildings. *Energy Build.* 39, 335–342.
- Fallahi, A., Haghghat, F., Elsadi, H., 2010. Energy performance assessment of double-skin facade with thermal mass. *Energy Build.* 42, 1499–1509.
- Flores Larsen, S., Filippin, C., Lesino, G., 2015. Modeling double skin green facades with traditional thermal simulation software. *Sol. Energy* 121, 56–67.
- Fuliotto, R., Cambuli, F., Mandas, N., Bacchin, N., Manara, G., Chen, Q., 2010. Experimental and numerical analysis of heat transfer and airflow on an interactive building facade. *Energy Build.* 42, 23–28.
- Gaillard, L., Giroux-Julien, S., Ménézo, C., Pabiou, H., 2014a. Experimental evaluation of a naturally ventilated PV double-skin building envelope in real operating conditions. *Sol. Energy* 103, 223–241.
- Gaillard, L., Ménézo, C., Giroux, S., Pabiou, H., Le-Berre, R., 2014b. Experimental Study of Thermal Response of PV Modules Integrated into Naturally-ventilated Double Skin Facades. *Energy Procedia* 48, 1254–1261.
- Gavan, V., Woloszyn, M., Kuznik, F., Roux, J.J., 2010. Experimental study of a mechanically ventilated double-skin façade with venetian sun-shading device: A full-scale investigation in controlled environment. *Sol. Energy* 84, 183–195.
- Government of Canada, n.d. Historical Data [WWW Document]. URL http://climate.weather.gc.ca/historical_data/search_historic_data_e.html
- Gratia, E., De Herde, A., 2004a. Natural ventilation in a double-skin facade. *Energy Build.* 36, 137–146.
- Gratia, E., De Herde, A., 2004b. Is day natural ventilation still possible in office buildings with a double-skin façade? *Build. Environ.* 39, 399–409.
- Gratia, E., De Herde, A., 2004c. Natural cooling strategies efficiency in an office building with a double-skin façade. *Energy Build.* 36, 1139–1152.
- Gratia, E., De Herde, A., 2004d. Optimal operation of a south double-skin facade. *Energy Build.* 36, 41–60.
- Gratia, E., De Herde, A., 2007a. The most efficient position of shading devices in a double-skin facade. *Energy Build.* 39, 364–373.
- Gratia, E., De Herde, A., 2007b. Are energy consumptions decreased with the addition of a double-skin? *Energy Build.* 39, 605–619.

- Gratia, E., De Herde, A., 2007c. Greenhouse effect in double-skin facade. *Energy Build.* 39, 199–211.
- Gratia, E., De Herde, A., 2007d. Guidelines for improving natural daytime ventilation in an office building with a double-skin facade. *Sol. Energy* 81, 435–448.
- Haase, M., Marques da Silva, F., Amato, a., 2009. Simulation of ventilated facades in hot and humid climates. *Energy Build.* 41, 361–373.
- Han, J., Lu, L., Peng, J., Yang, H., 2013. Performance of ventilated double-sided PV facade compared with conventional clear glass facade. *Energy Build.* 56, 204–209.
- Holman, J.P., 1997. *Heat Transfer*, 8th ed. McGraw-Hill.
- Incropera, F.P., DeWitt, D.P., 2011. *Introduction to Heat Transfer*, 6th editio. ed. Wiley.
- Jelle, B.P., Breivik, C., 2012. State-of-the-art building integrated photovoltaics. *Energy Procedia* 20, 68–77.
- Ji, Y., Cook, M.J., Hanby, V.I., Infield, D.G., Loveday, D.L., Mei, L., Building, Q., Gateway, T., Uk, L.L.E., 2007. CFD MODELLING OF DOUBLE-SKIN FAÇADES WITH VENETIAN BLINDS Institute of Energy and Sustainable Development , De Montfort University , Centre for Renewable Energy Systems Technology , Department of Electronic and Electrical Department of Civil and Building 1491–1498.
- Joe, J., Choi, W., Kwak, Y., Huh, J.H., 2014. Optimal design of a multi-story double skin facade. *Energy Build.* 76, 143–150.
- Joe, J., Choi, W., Kwon, H., Huh, J.H., 2013. Load characteristics and operation strategies of building integrated with multi-story double skin facade. *Energy Build.* 60, 185–198.
- Kala, S., Stathopoulos, T., Suresh Kumar, K., 2008. Wind loads on rainscreen walls: Boundary-layer wind tunnel experiments. *J. Wind Eng. Ind. Aerodyn.* 96, 1058–1073.
- Karava, P., Stathopoulos, T., Athienitis, A.K., 2003. Investigation of the performance of trickle ventilators. *Build. Environ.* 38, 981–993.
- Kim, D.W., Park, C.S., 2011. Difficulties and limitations in performance simulation of a double skin façade with EnergyPlus. *Energy Build.* 43, 3635–3645.
- Kim, S.Y., Song, K.D., 2007. Determining Photosensor Conditions of a Daylight Dimming Control System Using Different Double-skin Envelope Configurations. *Indoor Built Environ.* 16, 411–425.
- Kreider, J.F., Curtiss, P.S., Rabl, A., 2002. *Heating and Cooling of Buildings: Design for Efficiency*, Second. ed. McGraw-Hill, NewYork.
- Larsen, O.K., Heiselberg, P.K., Jensen, R.L., 2014a. Experimental data and boundary conditions for a Double-Skin Facade building in external air curtain mode. Aalborg Dep. Civ. Eng. Aalborg Univ. (DCE Tech. Memo. No. 38).
- Larsen, O.K., Heiselberg, P.K., Jensen, R.L., 2014b. Experimental data and boundary conditions for a Double-Skin

- Facade building in preheating mode. Aalborg Dep. Civ. Eng. Aalborg Univ. (DCE Tech. Memo. No. 40).
- Liao, L., 2005. Numerical and Experimental Investigation of Building-Integrated Photovoltaic-Thermal Systems. Concordia University.
- Liao, L., Athienitis, a. K., Candanedo, L., Park, K.-W., Poissant, Y., Collins, M., 2007. Numerical and Experimental Study of Heat Transfer in a BIPV-Thermal System. *J. Sol. Energy Eng.* 129, 423.
- Lou, W., Huang, M., Zhang, M., Lin, N., 2012. Experimental and zonal modeling for wind pressures on double-skin facades of a tall building. *Energy Build.* 54, 179–191.
- Manz, H., 2004. Total solar energy transmittance of glass double facades with free convection. *Energy Build.* 36, 127–136.
- Manz, H., Frank, T., 2005. Thermal simulation of buildings with double-skin façades. *Energy Build.* 37, 1114–1121.
- Manz, H., Schaelin, a., Simmler, H., 2004. Airflow patterns and thermal behavior of mechanically ventilated glass double facades. *Build. Environ.* 39, 1023–1033.
- Marques da Silva, F., Gomes, M.G., Rodrigues, a. M., 2015. Measuring and estimating airflow in naturally ventilated double skin facades. *Build. Environ.* 87, 292–301.
- Martinez, I., 1995. Radiative view factors [WWW Document]. ReCALL. URL <http://webserver.dmt.upm.es/~isidoro/tc3/Radiation View factors.pdf> (accessed 8.7.16).
- Matlab, n.d. Matworks [WWW Document]. 2016. URL <http://www.mathworks.com/>
- Mei, L., Infield, D., Eicker, U., Fux, V., 2003. Thermal modelling of a building with an integrated ventilated PV facade. *Energy Build.* 35, 605–617.
- Park, C.S., Augenbroe, G., Messadi, T., Thitisawat, M., Sadegh, N., 2004. Calibration of a lumped simulation model for double-skin façade systems. *Energy Build.* 36, 1117–1130.
- Pasut, W., De Carli, M., 2012. Evaluation of various CFD modelling strategies in predicting airflow and temperature in a naturally ventilated double skin faade. *Appl. Therm. Eng.* 37, 267–274.
- Peng, J., Lu, L., Yang, H., 2013. An experimental study of the thermal performance of a novel photovoltaic double-skin facade in Hong Kong. *Sol. Energy* 97, 293–304.
- Peng, J., Lu, L., Yang, H., Ma, T., 2015. Comparative study of the thermal and power performances of a semi-transparent photovoltaic façade under different ventilation modes. *Appl. Energy* 138, 572–583.
- Poirazis, H., 2007. Double-skin façades. *ASHRAE J.* 49, 70–73.
- Quesada, G., Rouse, D., Dutil, Y., Badache, M., Hallé, S., 2012a. A comprehensive review of solar facades. Transparent and translucent solar facades. *Renew. Sustain. Energy Rev.* 16, 2820–2832.
- Quesada, G., Rouse, D., Dutil, Y., Badache, M., Hallé, S., 2012b. A comprehensive review of solar facades.

- Transparent and translucent solar facades. *Renew. Sustain. Energy Rev.* 16, 2643–2651.
- Saelens, D., 2002. Energy performance assessment of single storey multiple-skin facades. Ph.D. dissertation, Laboratory for Building Physics, K.U. Leuven, Leuven.
- Saelens, D., Carmeliet, J., Hens, H., 2003. Energy Performance Assessment of Multiple-Skin Facades. *HVAC&R Res.* 9, 167–185.
- Saelens, D., Roels, S., Hens, H., 2008. Strategies to improve the energy performance of multiple-skin facades. *Build. Environ.* 43, 638–650.
- Safer, N., Woloszyn, M., Roux, J.J., 2005. Three-dimensional simulation with a CFD tool of the airflow phenomena in single floor double-skin facade equipped with a venetian blind. *Sol. Energy* 79, 193–203.
- Sandberg, M., 1999. Cooling of Building Integrated Photovoltaics by Ventilation Air. IEA-ECB&CS Annex 35.
- Serra, V., Zanghirella, F., Perino, M., 2010. Experimental evaluation of a climate facade: Energy efficiency and thermal comfort performance. *Energy Build.* 42, 50–62.
- Shameri, M. a., Alghoul, M. a., Elayeb, O., Zain, M.F.M., Alrubaih, M.S., Amir, H., Sopian, K., 2013. Daylighting characteristics of existing double-skin façade office buildings. *Energy Build.* 59, 279–286.
- Shameri, M. a., Alghoul, M. a., Sopian, K., Zain, M.F.M., Elayeb, O., 2011. Perspectives of double skin façade systems in buildings and energy saving. *Renew. Sustain. Energy Rev.* 15, 1468–1475.
- Shapiro, A.B., 1985. Computer Implementation, Accuracy, and Timing of Radiation View Factor Algorithms. *ASME J. Heat Transf.* 730–732.
- Tzempelikos, A., Athienitis, A.K., Karava, P., 2007. Simulation of facade and envelope design options for a new institutional building. *Sol. Energy* 81, 1088–1103.
- Viljoen, a., Dubiel, J., Wilson, M., Fontoynt, M., 1997. Investigations for improving the daylighting potential of double-skinned office buildings. *Sol. Energy* 59, 179–194.
- Walton, G.N., 1986. Algorithms for Calculating Radiation View Factors Between Plane Convex Polygons With Obstructions. National Bureau of Standards, NBSIR 86-3463.
- Wilkins, C.K., Hosni, M.H., 2011. Plug load design factors. *ASHRAE J.* 53, 30–34.
- Xu, X.L., Yang, Z., 2008. Natural ventilation in the double skin facade with venetian blind. *Energy Build.* 40, 1498–1504.
- Zeng, Z., Li, X., Li, C., Zhu, Y., 2012. Modeling ventilation in naturally ventilated double-skin facade with a venetian blind. *Build. Environ.* 57, 1–6.
- Zhou, J., Chen, Y., 2010. A review on applying ventilated double-skin facade to buildings in hot-summer and cold-winter zone in China. *Renew. Sustain. Energy Rev.* 14, 1321–1328.

Zöllner, a., Winter, E.R.F., Viskanta, R., 2002. Experimental studies of combined heat transfer in turbulent mixed convection fluid flows in double-skin-façades. *Int. J. Heat Mass Transf.* 45, 4401–4408.

Appendix A: Specifications about the Heat Pump

The PLR, EER and COP of a heat pump assumed to provide heating and cooling within the adjacent zone is presented.

Table 0.1: PLR and EER map for the chiller

		Temperatures											
		20		25		30		35		40		45	
PLR		kW	EER	kW	EER	kW	EER	kW	EER	kW	EER	kW	EER
kW Cooling nominal 14	100	20	4.35	19	3.74	18	3.24	16.8	2.77	15.4	2.32	14.1	1.96
	90	18.2	4.64	17.3	3.96	16.4	3.41	15.3	2.89	14.1	2.42	13	2.04
	80	15.6	5.18	14.8	4.35	14	3.68	13	3.08	12	2.56	11.2	2.15
	60	12.9	5.87	12.2	4.83	11.5	4.01	10.7	3.3	9.98	2.72	9.36	2.28
	50	11	6.52	10.3	5.27	9.74	4.3	9.12	3.51	8.52	2.86	8.09	2.39
	30	9.16	7.7	8.5	6.06	7.98	4.84	7.49	3.85	7.06	3.09	6.82	2.56
kW Cooling nominal 16	100	23.6	3.75	22.2	3.22	20.9	2.78	19.4	2.38	17.8	2.01	16.5	1.71
	90	21.7	3.98	20.5	3.41	19.4	2.94	18	2.5	16.6	2.12	15.3	1.81
	80	17	4.7	16.1	3.97	15.2	3.37	14.2	2.81	13.1	2.38	12.2	2.02
	60	15.3	5.04	14.5	4.2	13.7	3.53	12.8	2.92	11.8	2.46	11.1	2.09
	50	13.1	5.56	12.4	4.56	11.7	3.78	10.9	3.09	10.1	2.58	9.61	2.19
	30	11	6.23	10.3	5.03	9.63	4.1	9.02	3.31	8.46	2.73	8.12	2.13
kW Cooling nominal 19	100	29.7	4.12	28	3.54	26.2	3.05	24.1	2.56	21.9	2.15	19.8	1.79
	90	27.3	4.38	25.8	3.75	24.2	3.23	22.3	2.7	20.3	2.27	18.4	1.88
	80	23	4.95	21.7	4.2	20.4	3.57	18.8	2.95	17.2	2.48	15.7	2.05
	60	19.4	5.59	18.3	4.65	17.1	3.89	15.8	3.16	14.6	2.63	13.3	2.18
	50	16.6	6.24	15.5	5.1	14.6	4.2	13.5	3.37	12.4	2.78	11.5	2.29
	30	13.8	7.14	12.8	5.72	12	4.62	11.1	3.64	10.3	2.97	9.69	2.44
kW Cooling nominal 22	100	33.2	4.25	31.5	3.66	29.6	3.14	28.2	2.74	24.6	2.17	22.1	1.76
	90	30	4.59	29.4	3.93	27.8	3.38	25.5	2.83	23.1	2.34	20.5	1.87
	80	28.5	4.87	27	4.12	25.6	3.55	23.4	2.95	21.5	2.47	19	1.97
	60	22.6	5.4	24.4	4.56	20.4	3.93	19	3.32	17.2	2.73	15.5	2.24
	50	19.6	7.93	18.6	6.37	17.5	5.22	16.4	4.34	15	3.51	13.6	2.89
	30	12.3	9.74	11.6	7.63	11	6.16	10.3	5.04	9.5	3.99	8.4	3.1

Table 0.2: PLR and COP map for the heat pump

		Temperatures																	
		-20		-10		-7		0		2		7		10		15		18	
	PLR	kW	COP	kW	COP	kW	COP	kW	COP	kW	COP	kW	COP	kW	COP	kW	COP	kW	COP
kW Thermal Nominal 9	100	7.37	1.36	10.9	1.94	11.9	2.1	14.1	2.43	14.9	2.56	18.6	3.14	19.6	3.3	22.2	3.69	23.7	3.91
	90	6.67	1.4	9.89	1.99	10.9	2.16	13	2.49	13.8	2.62	17.2	3.23	18.1	3.4	20.4	3.8	21.8	4.04
	70	4.94	1.54	7.49	2.14	8.51	2.32	10.3	2.68	10.9	2.82	14.4	3.48	14.8	3.66	16.5	4.11	17.6	4.38
	50	3.35	1.79	5.29	2.37	6.32	2.54	7.9	2.92	8.36	3.08	11.3	3.78	11.8	3.99	13	4.5	13.7	4.8
	40	2.56	2.11	4.19	2.61	5.22	2.75	6.68	3.14	7.07	3.31	9.94	4.02	10.2	4.26	11.2	4.82	11.7	5.16
kW Thermal Nominal 10	100	8.87	1.4	12.2	1.86	13.3	1.99	15.3	2.24	16.3	2.37	20.5	2.93	21.8	3.09	24.5	3.44	26.1	3.64
	90	8.08	1.43	11.2	1.9	12.1	2.04	14.2	2.28	15.1	2.41	18.7	3.06	19.6	3.2	22.1	3.57	23.6	3.79
	70	6.2	1.54	8.78	2.03	9.62	2.18	11.5	2.42	12.3	2.56	15.3	3.31	15.8	3.44	17.8	3.87	19	4.11
	50	4.25	1.74	6.21	2.22	7.1	2.37	8.73	2.64	9.28	2.79	12.1	3.59	12.4	3.75	13.8	4.22	14.6	4.5
	40	3.27	1.98	4.93	2.42	5.84	2.55	7.33	2.83	7.8	3	10.5	3.83	10.7	4	11.8	4.52	12.4	4.83
kW Thermal Nominal 11	100	8.11	1.09	14.2	1.86	16	2.08	19.9	2.53	21	2.65	25.8	3.21	27.1	3.36	30.7	3.75	32.8	3.98
	90	7.37	1.12	13	1.9	14.6	2.13	18.4	2.57	19.4	2.7	23.4	3.35	24.4	3.48	27.6	3.91	29.6	4.16
	70	5.56	1.22	9.98	2.05	11.5	2.3	14.8	2.77	15.5	2.9	19.2	3.63	19.7	3.76	22.2	4.24	23.7	4.52
	50	3.78	1.4	7.04	2.27	8.45	2.53	11.2	3.04	11.8	3.19	15.2	3.97	15.5	4.12	17.3	4.66	18.3	4.98
	40	2.9	1.63	5.57	2.51	6.95	2.75	9.38	3.3	9.88	3.46	13.2	4.26	13.4	4.43	14.8	5.03	15.6	5.39
kW Thermal Nominal 15	100	13.2	1.73	15.9	1.95	17	2.07	20.3	2.42	21.6	2.56	27.2	3.17	28.7	3.33	32.6	3.73	34.9	3.97
	90	11.8	1.65	14.6	1.98	15.6	2.09	16.8	2.21	17.9	2.39	25.1	3.24	26.5	3.41	30.1	3.83	32.3	4.08
	70	8.93	1.58	11.2	1.93	12.1	2.07	14.7	2.48	15.7	2.67	19.6	3.26	20.9	3.45	23.9	3.92	25.7	4.2
	50	6.36	1.47	8.2	1.86	8.94	2.02	10.4	2.32	11.1	2.5	14.9	3.28	15.9	3.5	18.1	3.98	19.4	4.27
	40	4.88	1.35	6.4	1.74	7.02	1.91	8.64	2.35	9.26	2.52	11.8	3.21	12.7	3.46	14.4	3.86	15.4	4.09

Appendix B: Temperature and Velocity Profiles

Temperature and velocity profile for certain days, for the air within the cavity as well as the temperature of the photovoltaics

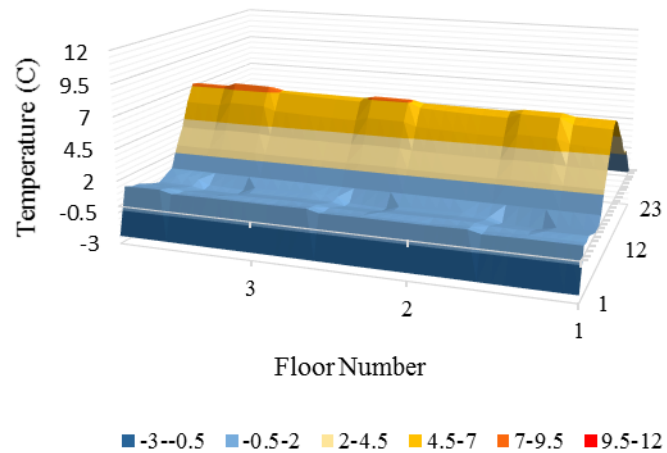
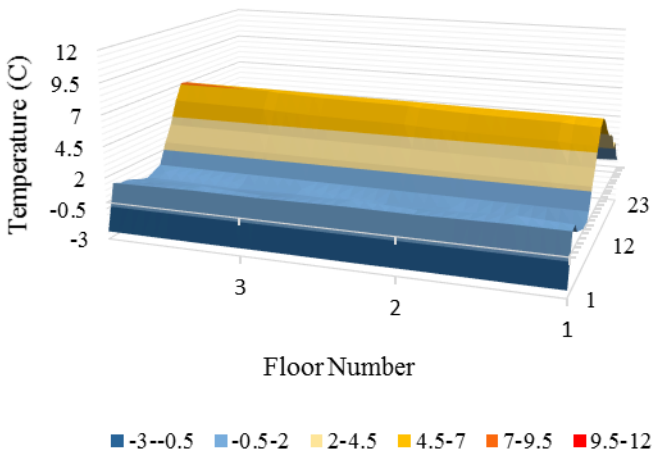
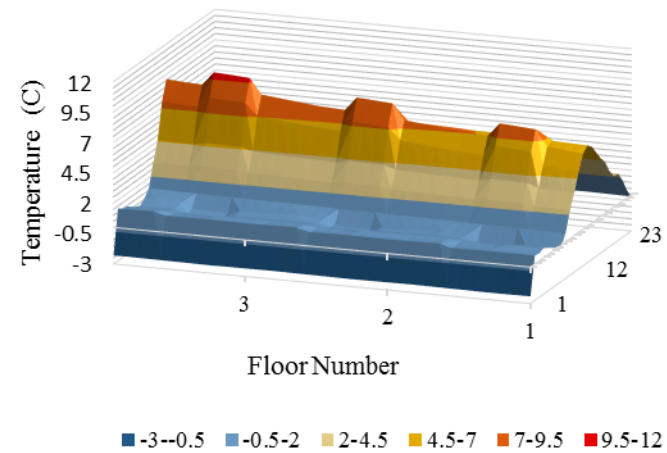
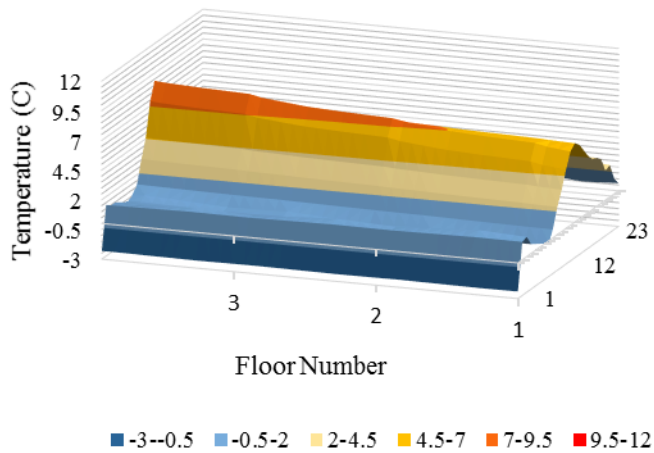


Figure 0.1: Temperature at the middle of the cavity of the DSF-P for a winter day for the case without roller blind for $V=1.5\text{m/s}$

Figure 0.2: Temperature at the middle of the cavity of the DSF-P for a winter day for the case with roller blind $V=1.5\text{m/s}$

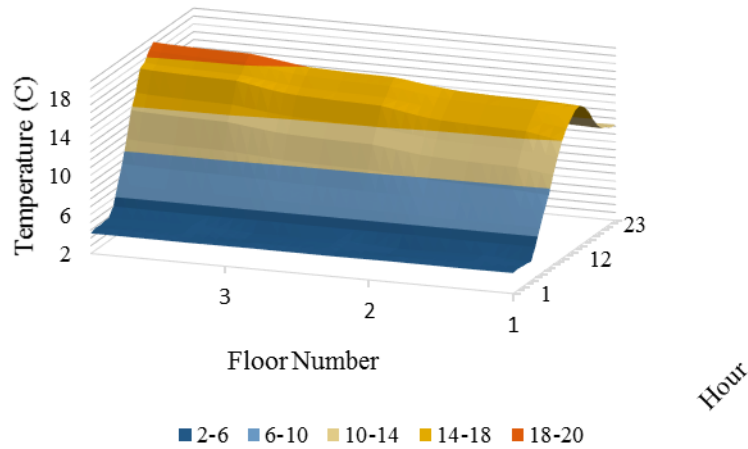


Figure 0.3: Temperature at the middle of the cavity of the DSF-P for May 1st for the case without roller blind for $V=0.5\text{m/s}$

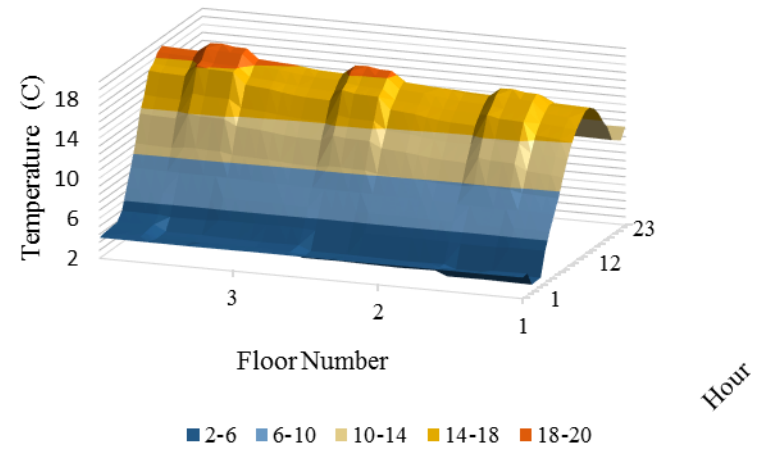


Figure 0.4: Temperature at the middle of the cavity of the DSF-P for May 1st for the case with roller blind for $V=0.5\text{m/s}$

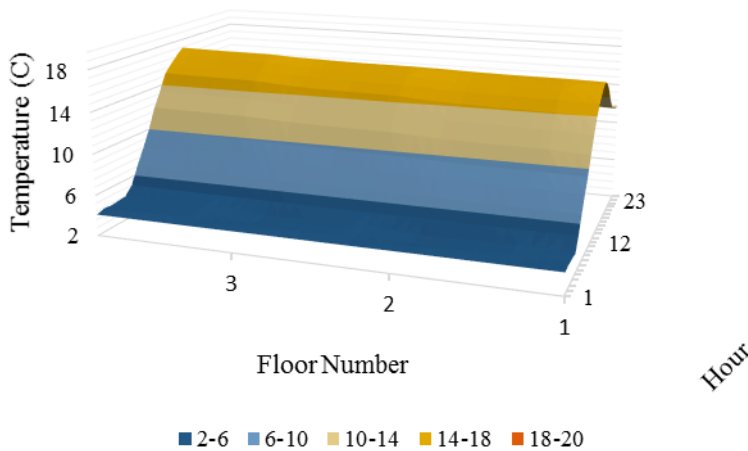


Figure 0.5: Temperature at the middle of the cavity of the DSF-P for May 1st for the case without roller blind for $V=1.5\text{m/s}$

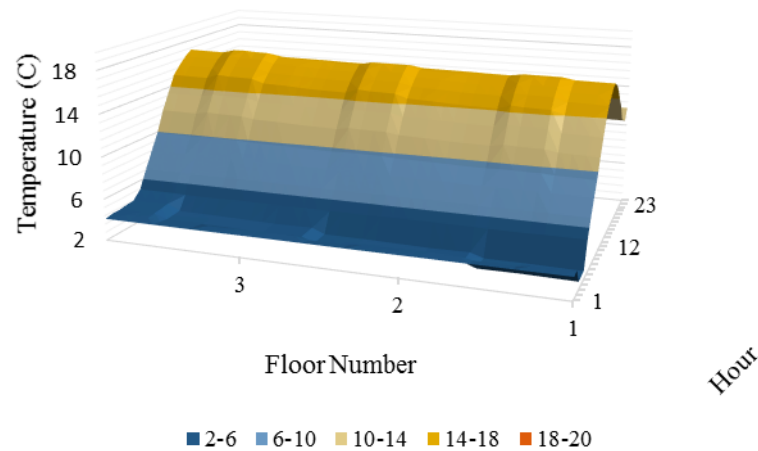


Figure 0.6: Temperature at the middle of the cavity of the DSF-P for May 1st for the case with roller blind for $V=1.5\text{m/s}$

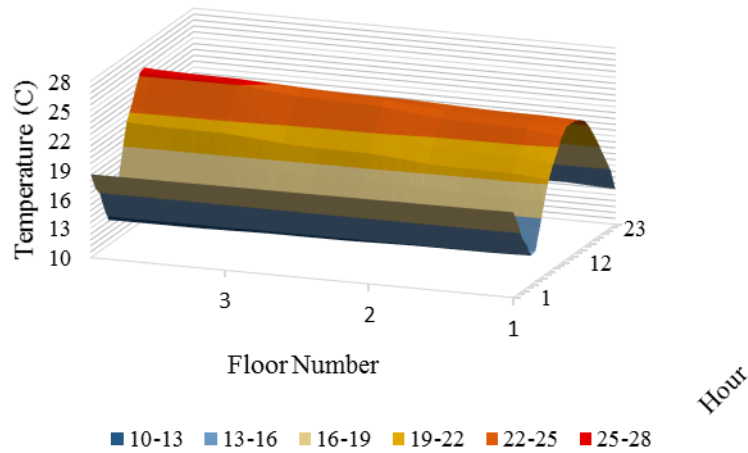


Figure 0.7: Temperature at the middle of the cavity of the DSF-P for August 1st for the case without roller blind for $V=0.5\text{m/s}$

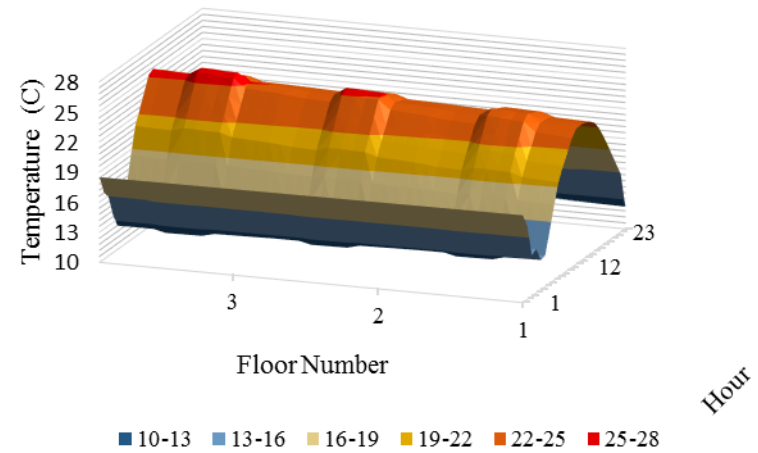


Figure 0.8: Temperature at the middle of the cavity of the DSF-P for August 1st for the case with roller blind for $V=0.5\text{m/s}$

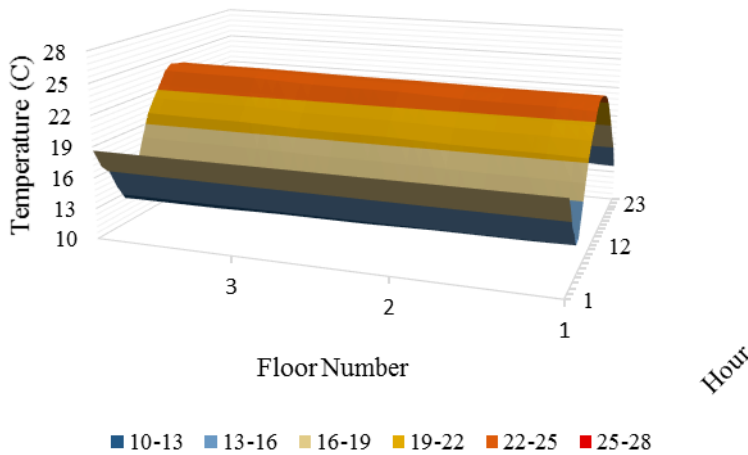


Figure 0.9: Temperature at the middle of the cavity of the DSF-P for August 1st for the case without roller blind for $V=1.5\text{m/s}$

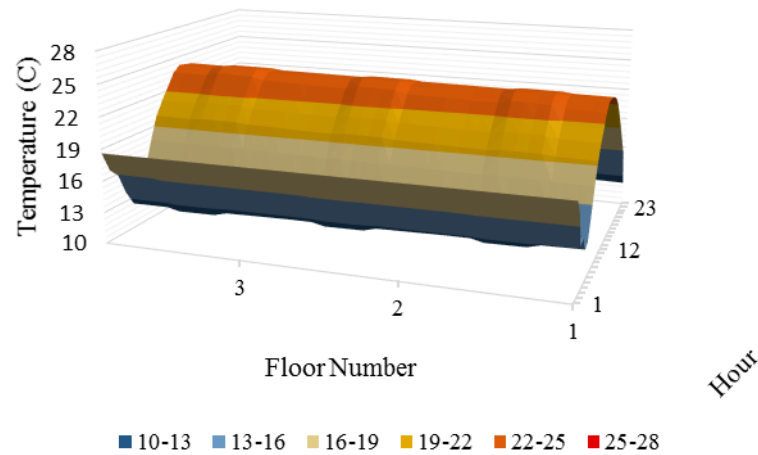


Figure 0.10: Temperature at the middle of the cavity of the DSF-P for August 1st for the case with roller blind for $V=1.5\text{m/s}$

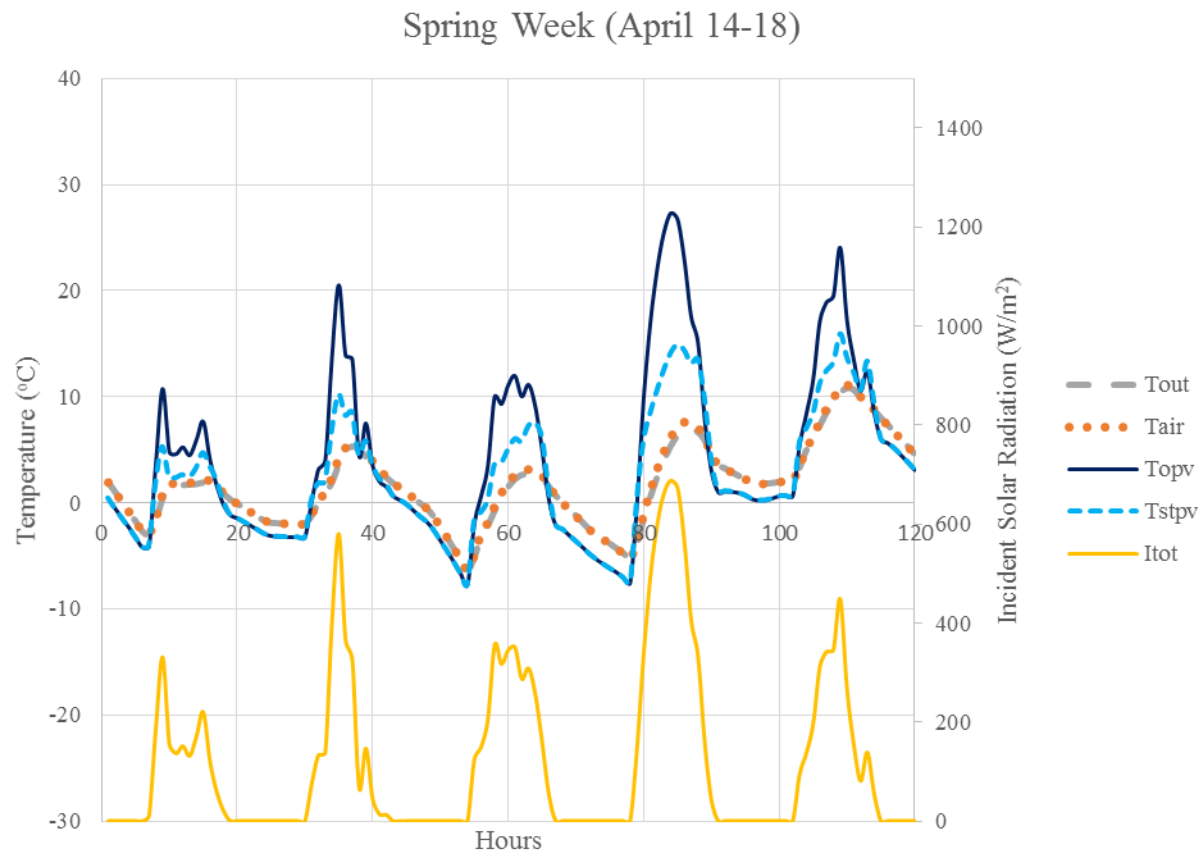


Figure 0.11: Simulated temperatures and incident solar radiation for a spring week

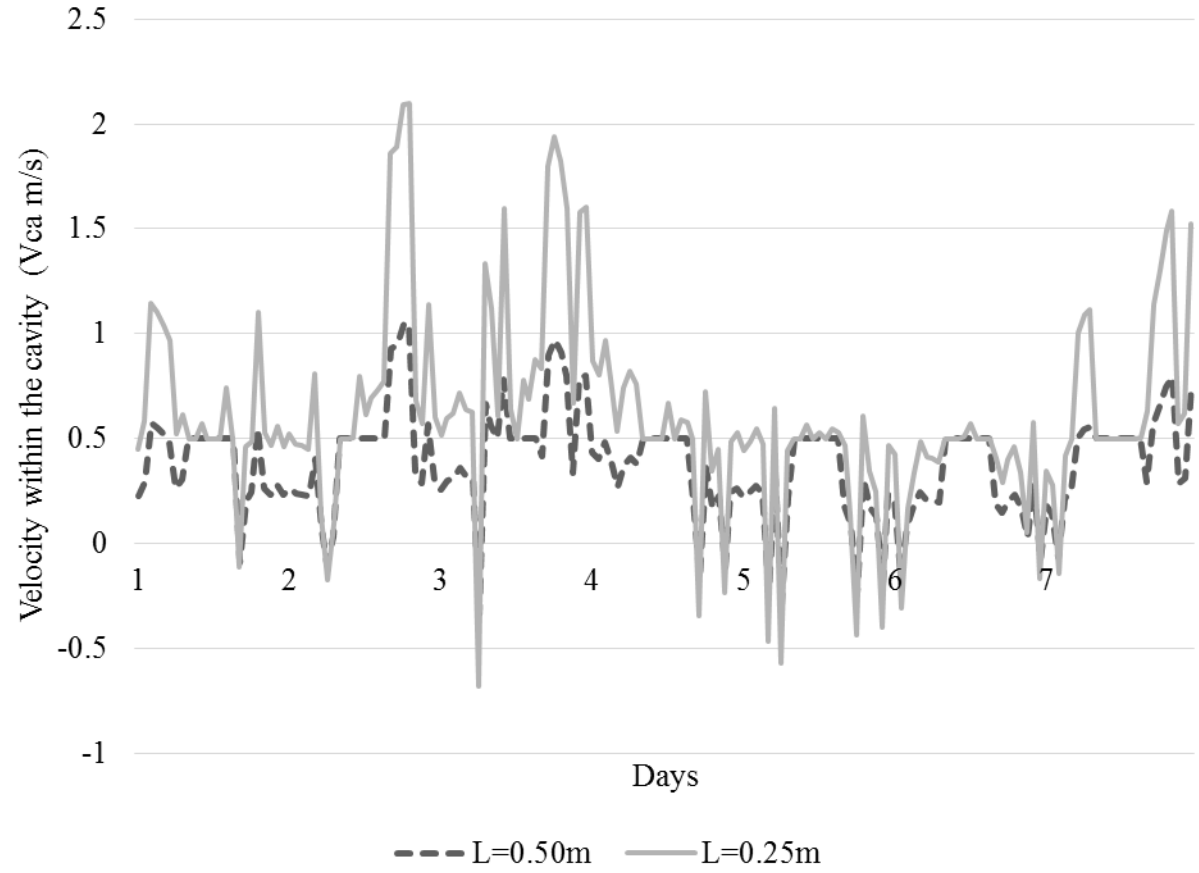


Figure 0.12: Velocity of the air within the cavity with a set-point of 0.5m/s for the cases of $L=0.25\text{m}$ and $L=0.50\text{m}$

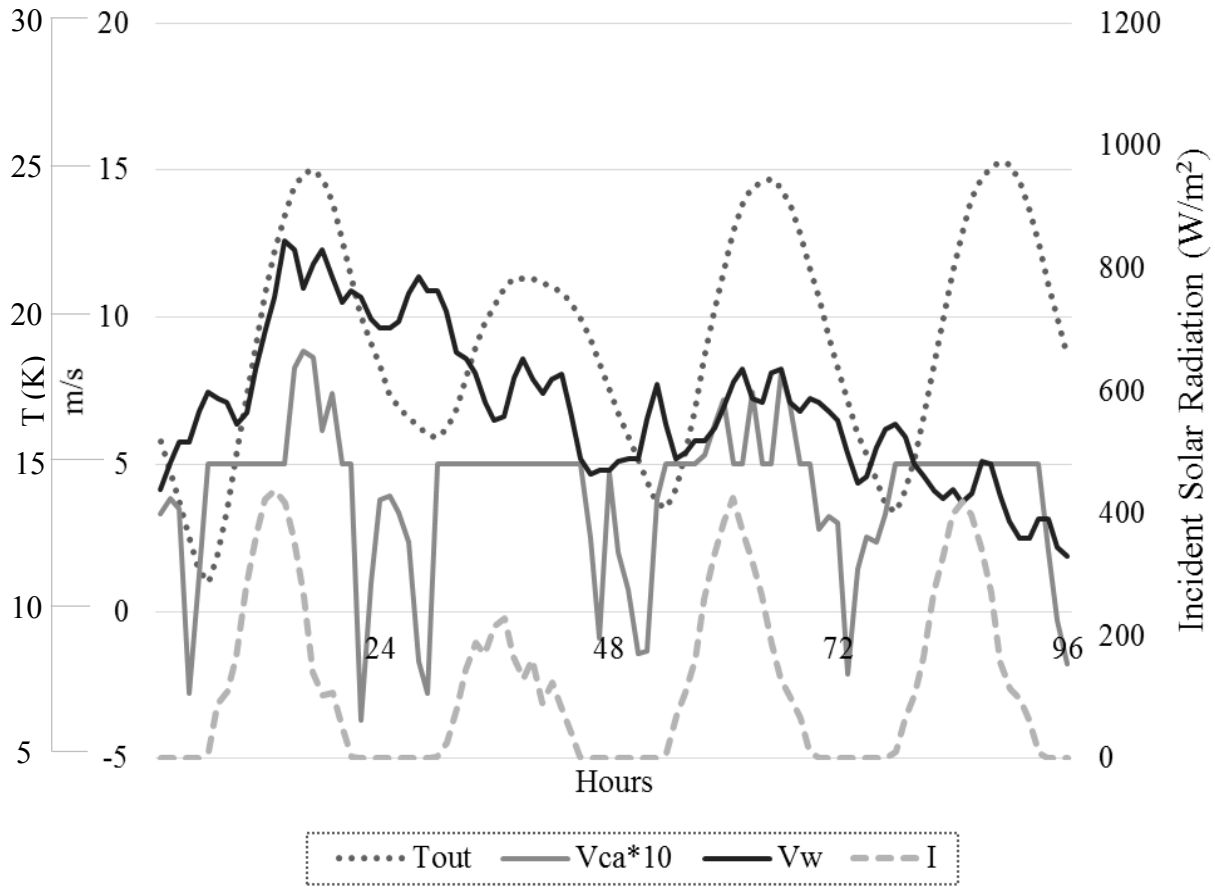


Figure 0.13: Wind and cavity velocities for four summer days for 0.50m cavity widths

Appendix C: Shading

Different shading configurations provide different shading on the interior skin. This shading is presented in this appendix

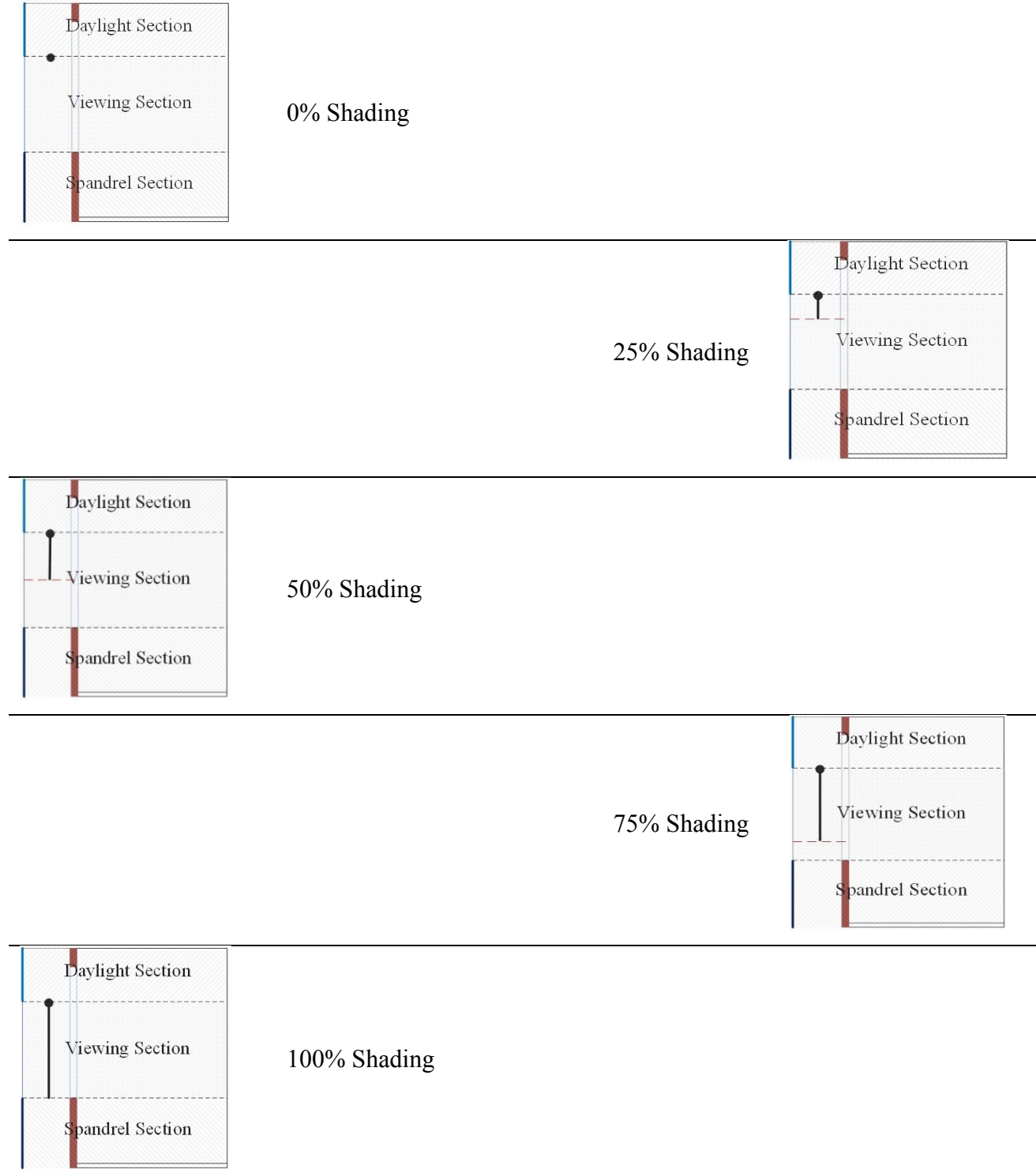


Figure 0.1: Different shading configurations examined

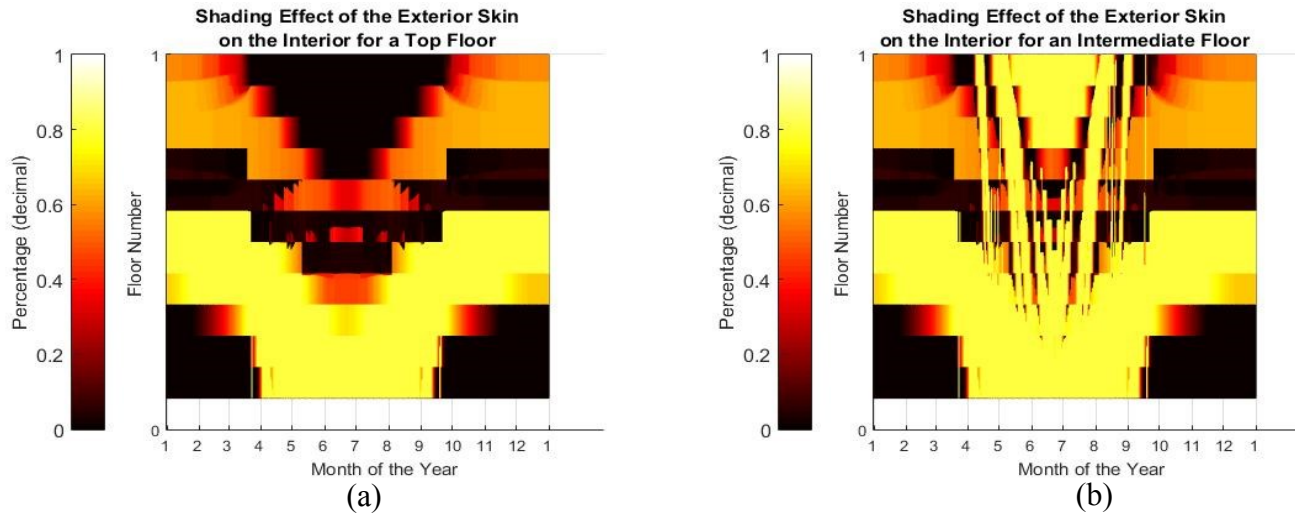


Figure 0.2: Shading of the exterior skin on the interior for a top (a) and a middle floor (b) 25%

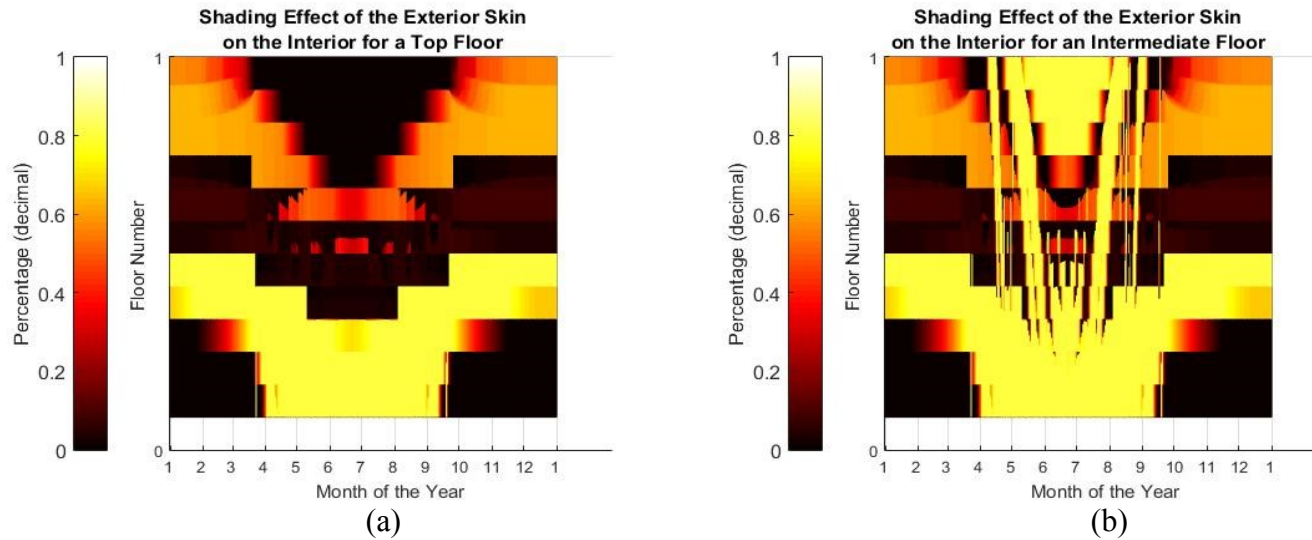


Figure 0.3: Shading of the exterior skin on the interior for a top (a) and a middle floor (b) 50%

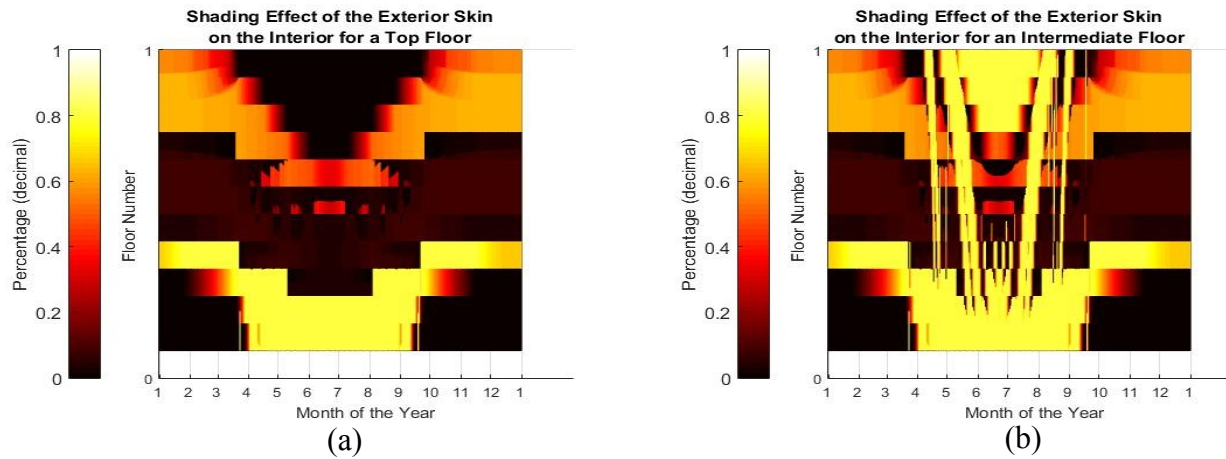


Figure 0.4: Shading of the exterior skin on the interior for a top (a) and a middle floor (b) 75%

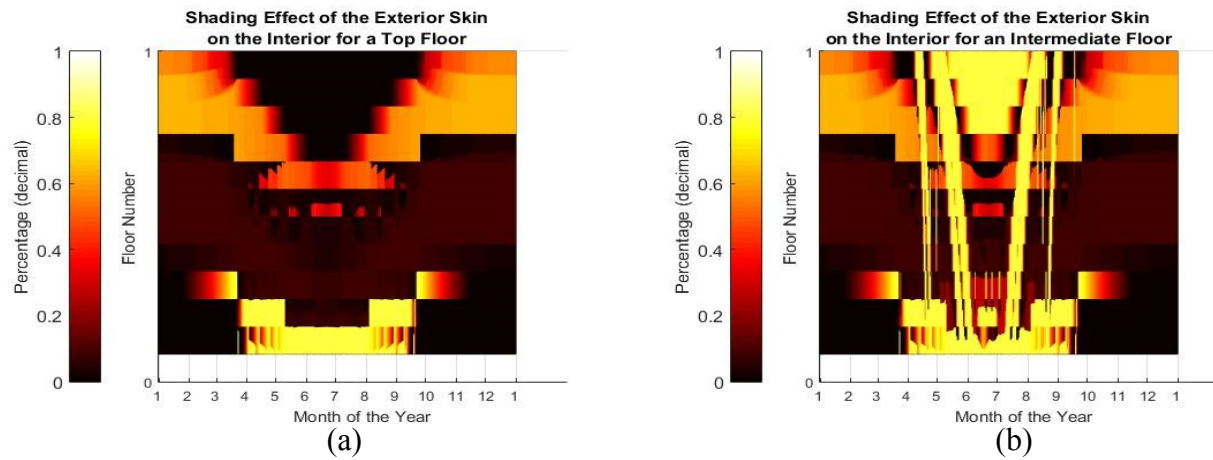


Figure 0.5: Shading of the exterior skin on the interior for a top (a) and a middle floor (b) 100%

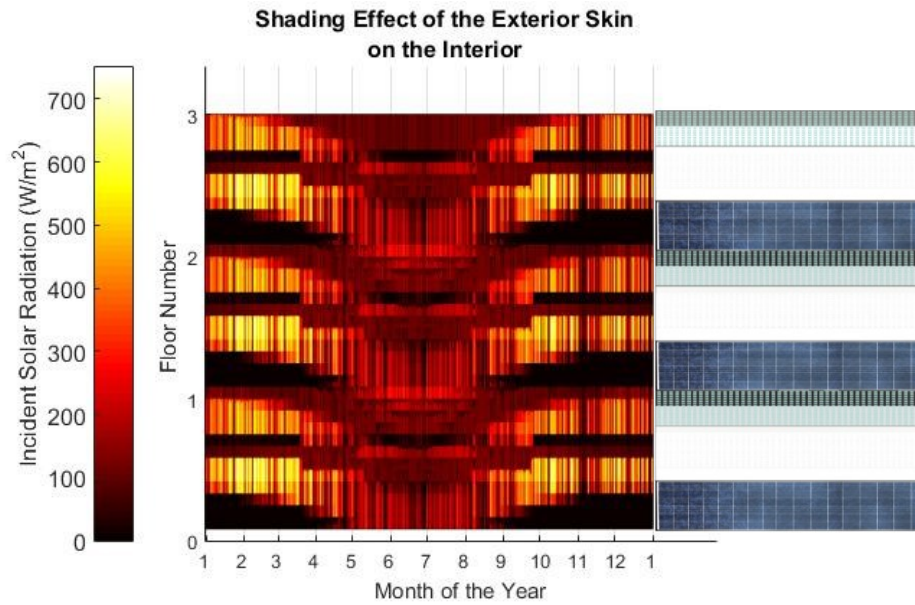


Figure 0.6: Incident solar radiation on the interior skin for 25% shading

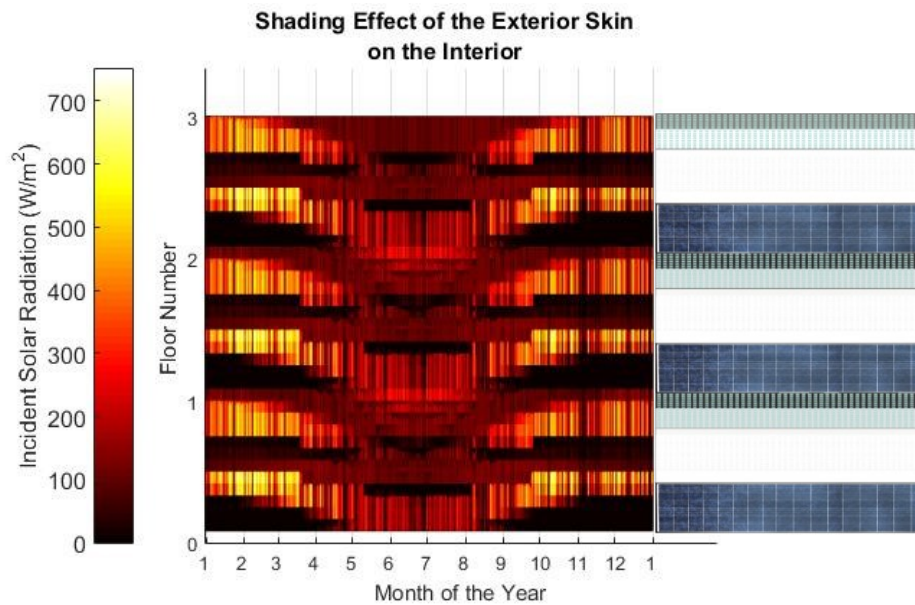


Figure 0.7: Incident solar radiation on the interior skin for 50% shading

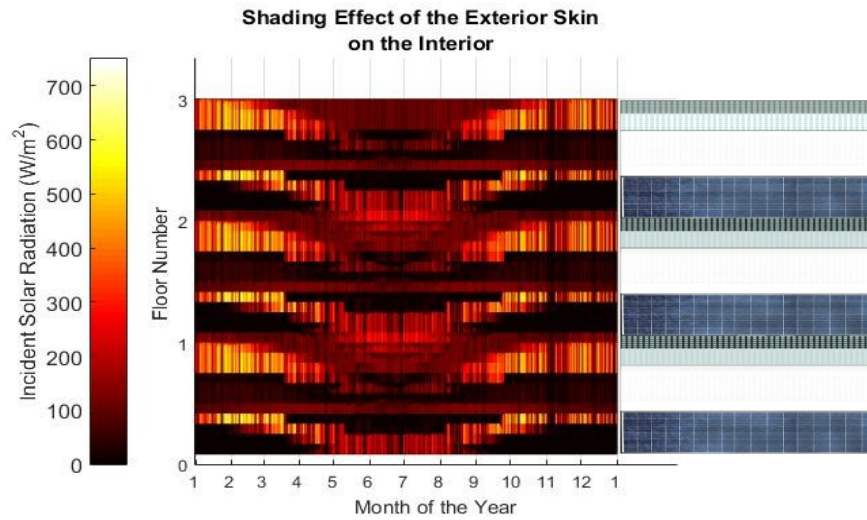


Figure 0.8: Incident solar radiation on the interior skin for 75% shading

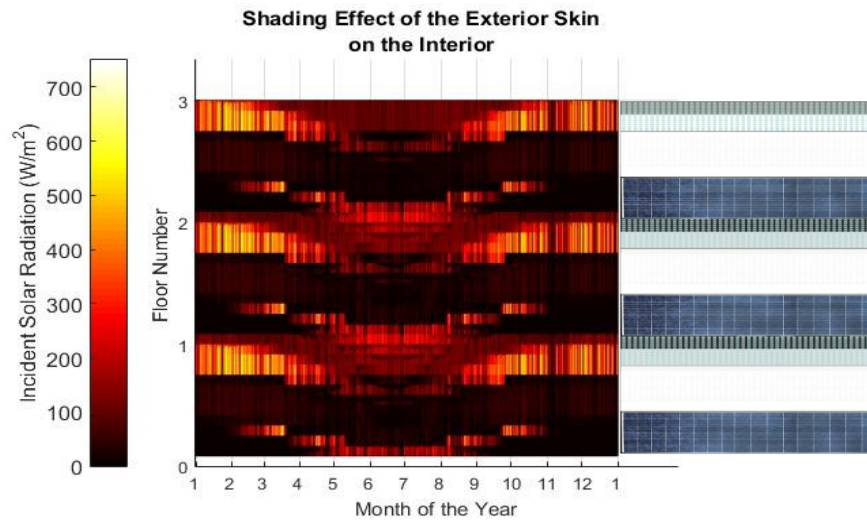


Figure 0.9: Incident solar radiation on the interior skin for 100% shading

Appendix D: Annual pressure difference and velocity within the cavity

Mechanical, Thermal and Wind pressure difference and the velocity of the air for different velocity set-points within the cavity for one year in Montreal are presented.

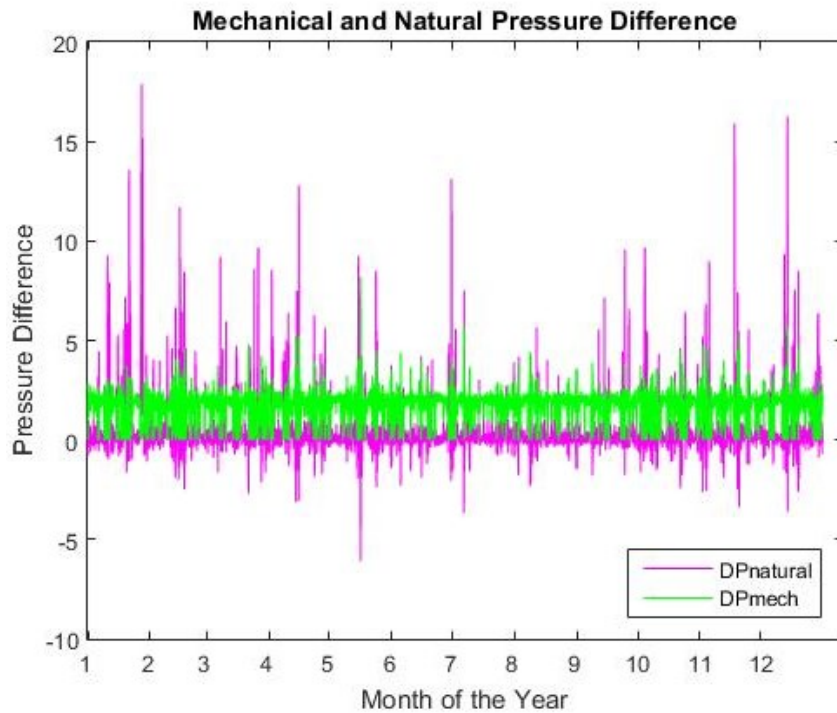


Figure 0.1: Pressure difference inside the cavity caused by mechanical and natural means for constant velocity of 0.5m/s

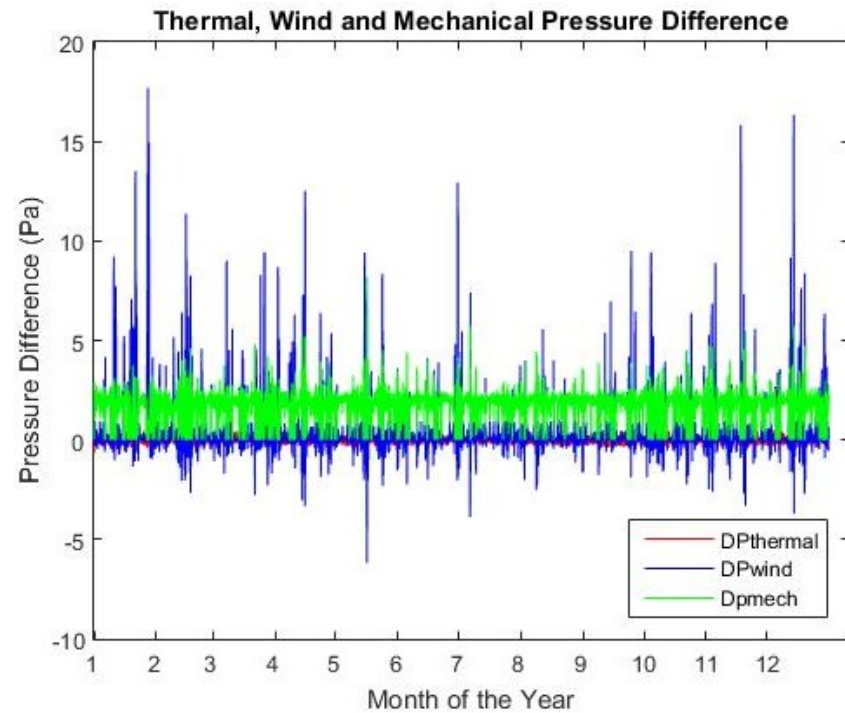


Figure 0.2: Pressure difference inside the cavity caused by thermal, wind and mechanical means for constant velocity of 0.5m/s

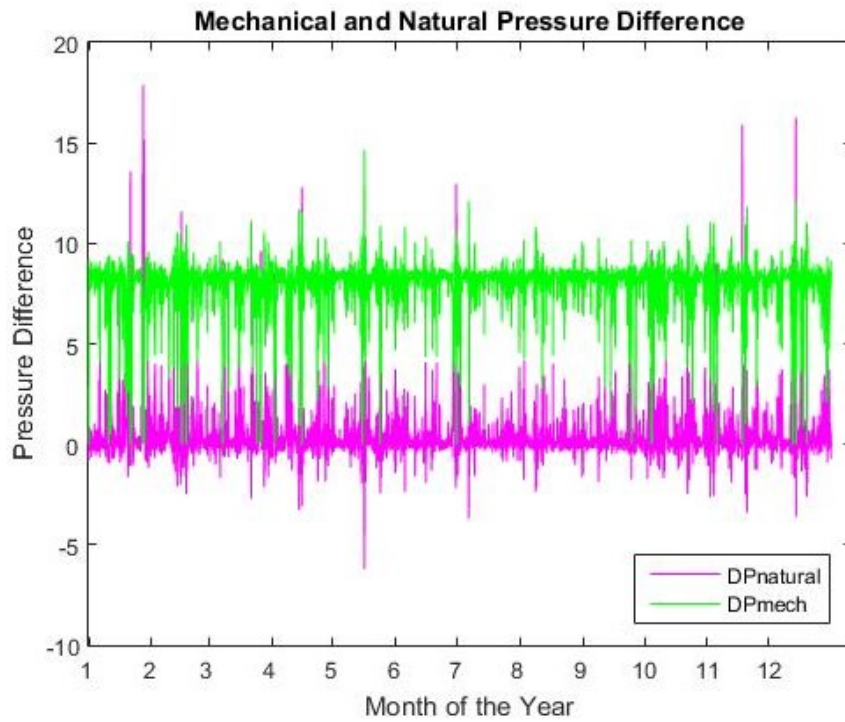


Figure 0.3: Pressure difference inside the cavity caused by mechanical and natural means for constant velocity of 1.0m/s

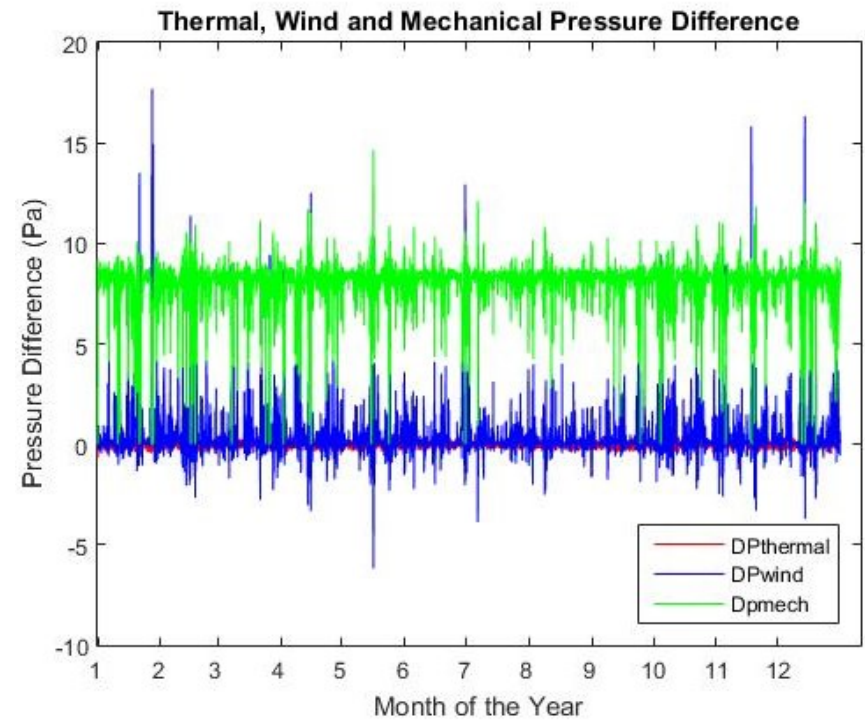


Figure 0.4: Pressure difference inside the cavity caused by thermal, wind and mechanical means for constant velocity of 1.0m/s

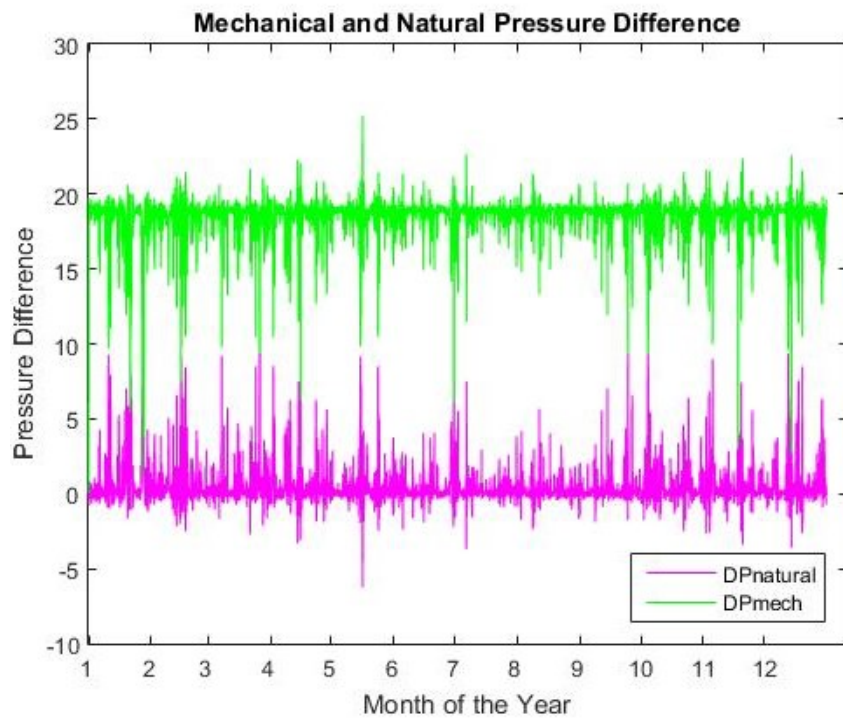


Figure 0.5: Pressure difference inside the cavity caused by mechanical and natural means for constant velocity of 1.5m/s

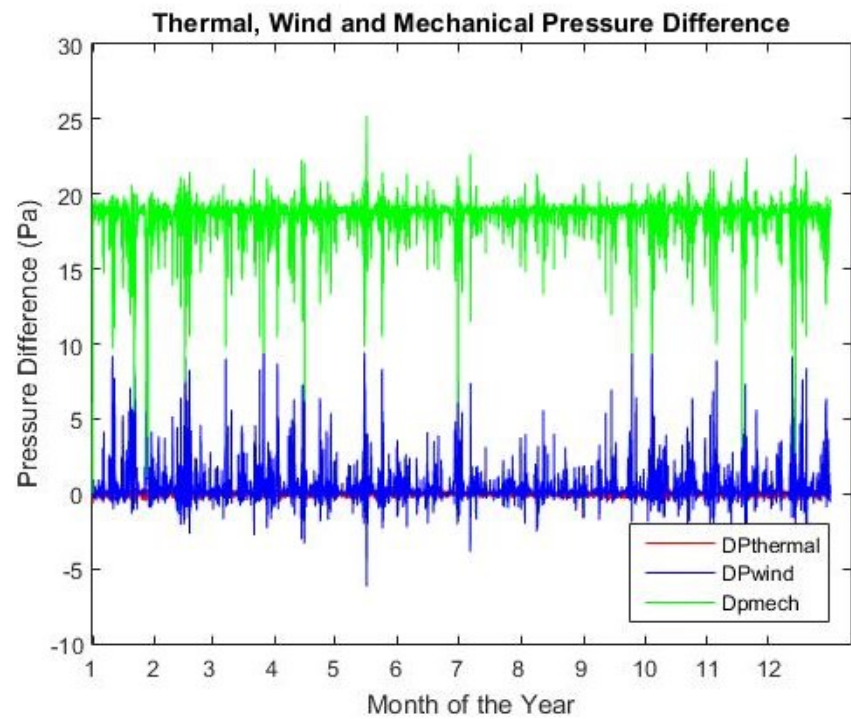


Figure 0.6: Pressure difference inside the cavity caused by thermal, wind and mechanical means for constant velocity of 1.5m/s

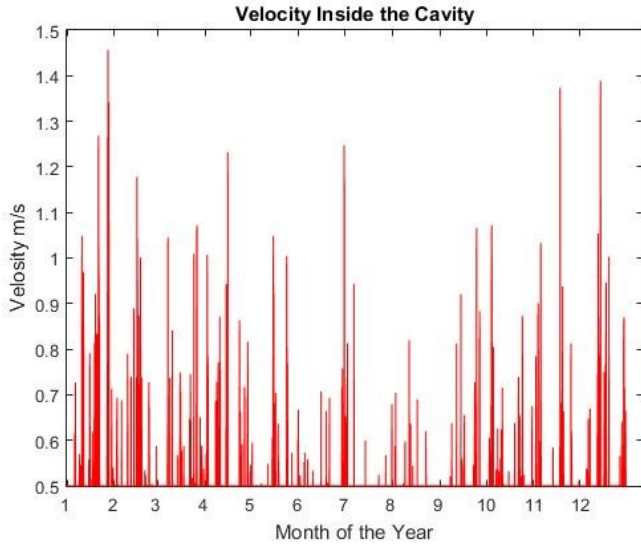


Figure 0.7: Velocity of the air inside the cavity set to be 0.5m/s (Strategy#1)

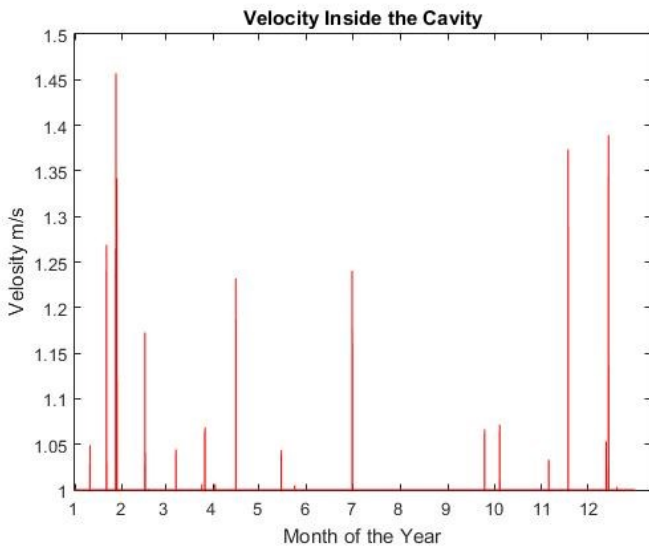


Figure 0.8: Velocity of the air inside the cavity set to be 1.0m/s (Strategy#1)

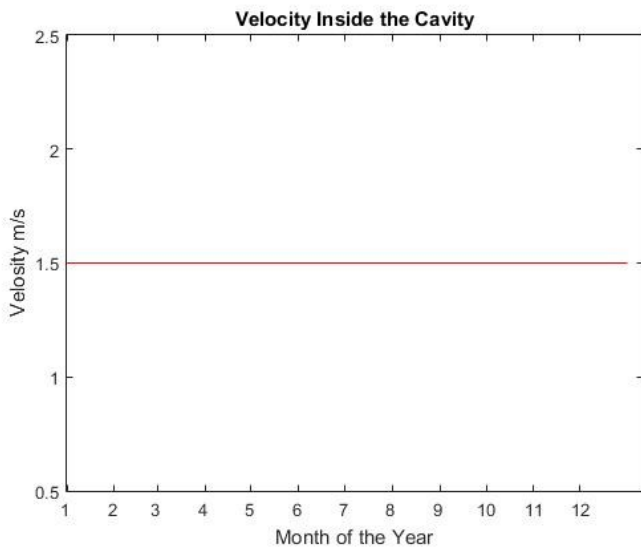


Figure 0.9: Velocity of the air inside the cavity set to be 1.0m/s (Strategy#1)

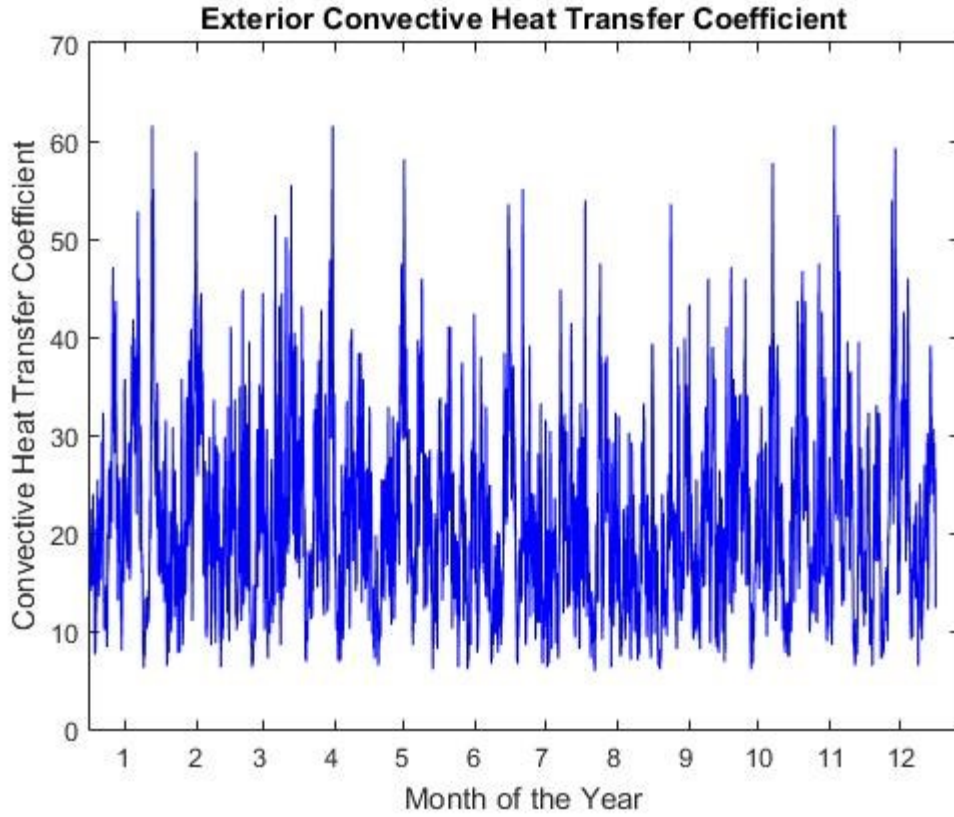


Figure 0.10: Exterior convective heat transfer coefficient

Table 0.1: Interior and exterior pressure coefficients for different wind direction

Angle	C _{pin}	C _{pout}	ΔCP
0	0.842236	0.997844	0.155608
30	0.667081	0.795349	0.128268
60	0.003727	0.147282	0.143555
90	-0.88323	-0.93739	-0.05416
120	-0.85342	-0.84287	0.010545
150	-0.85714	-0.81666	0.04048
180	-0.99503	-0.97757	0.01746
210	-0.8646	-0.87415	-0.00955
240	-0.81615	-0.80635	0.009799
270	-0.86832	-0.91082	-0.0425
300	0.055901	0.113391	0.05749
330	0.722981	0.834639	0.111658

Appendix E: Daylight

Daylight within the room for one year in Montreal for different shading cases is presented. View factors are also presented.

Roller blind at 25% shading position

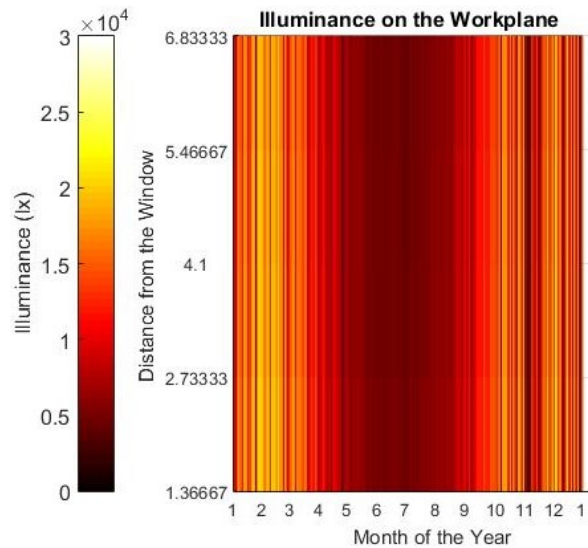


Figure 0.1: Illuminance levels on the workplane throughout the year (25% shading)

Roller blind at 50% shading position

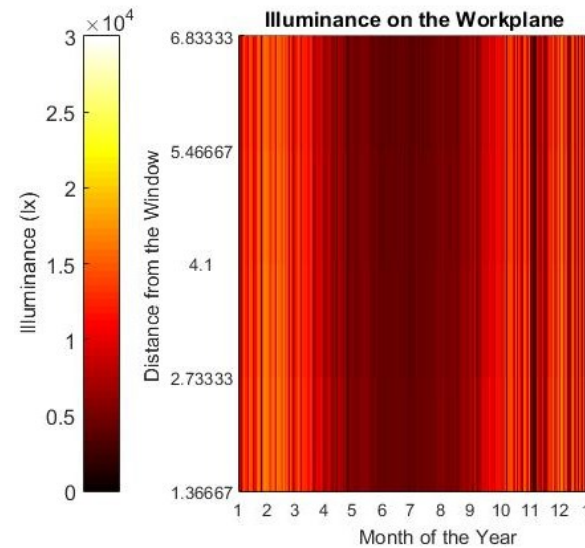


Figure 0.2: Illuminance levels on the workplane throughout the year (50% shading)

Roller blind at 75% shading position

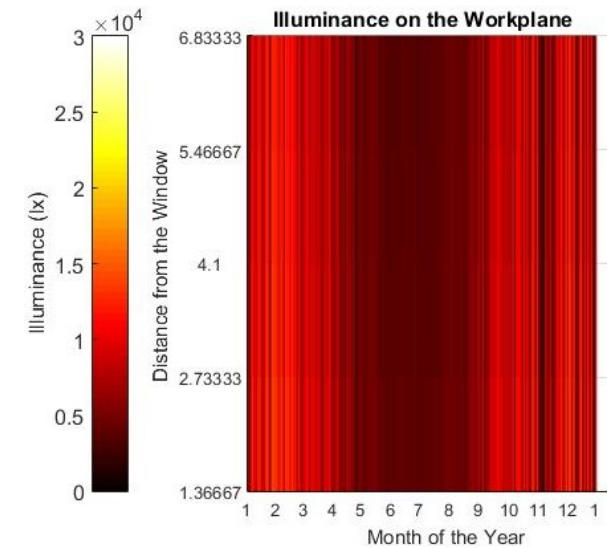


Figure 0.3: Illuminance levels on the workplane throughout the year (75% shading)

Average Monthly Illuminance without Shade 0%

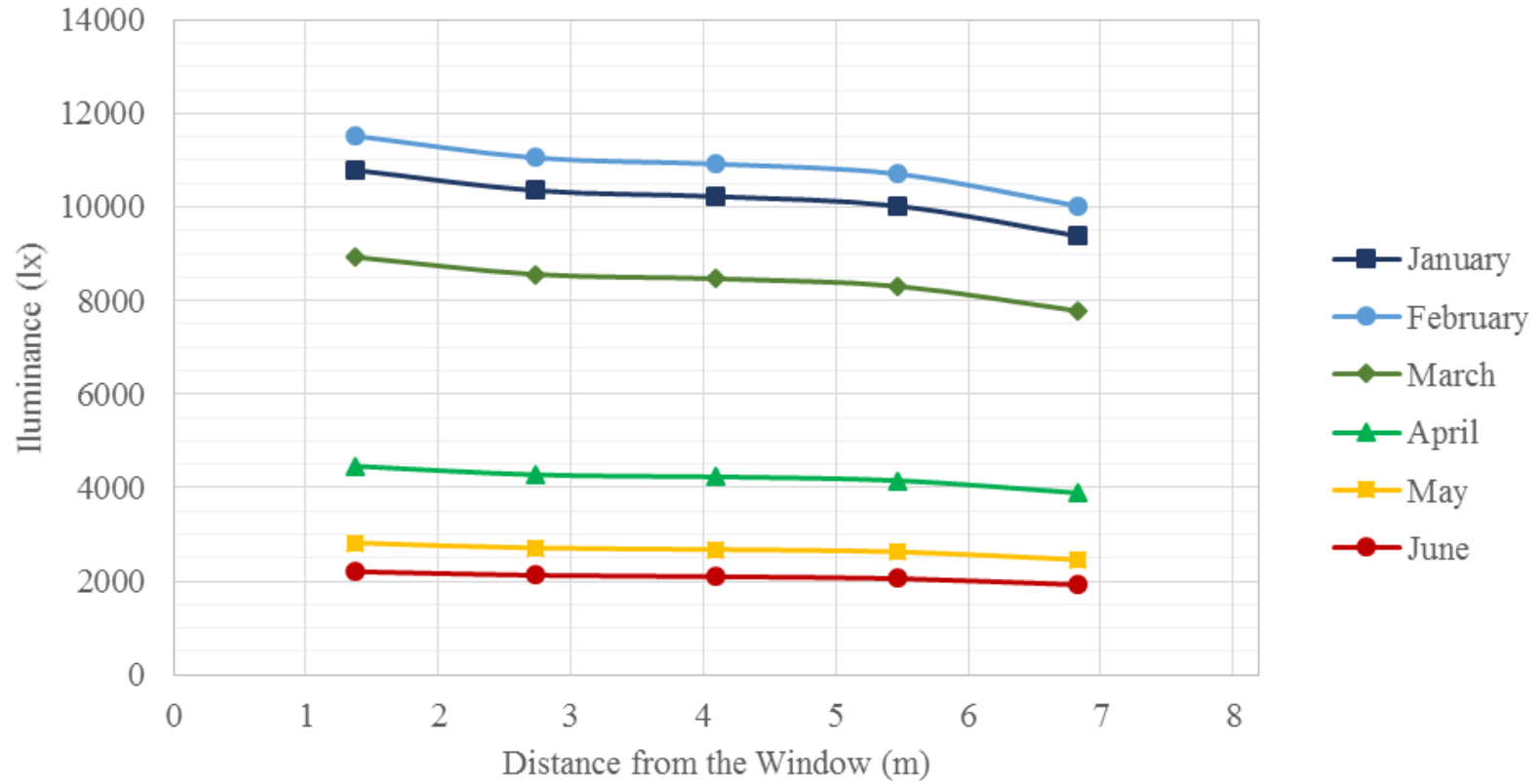


Figure 0.4: Monthly illuminance as a function of the distance from the window (0% shading)

Levels of Daylight Autonomy without Shading 0%

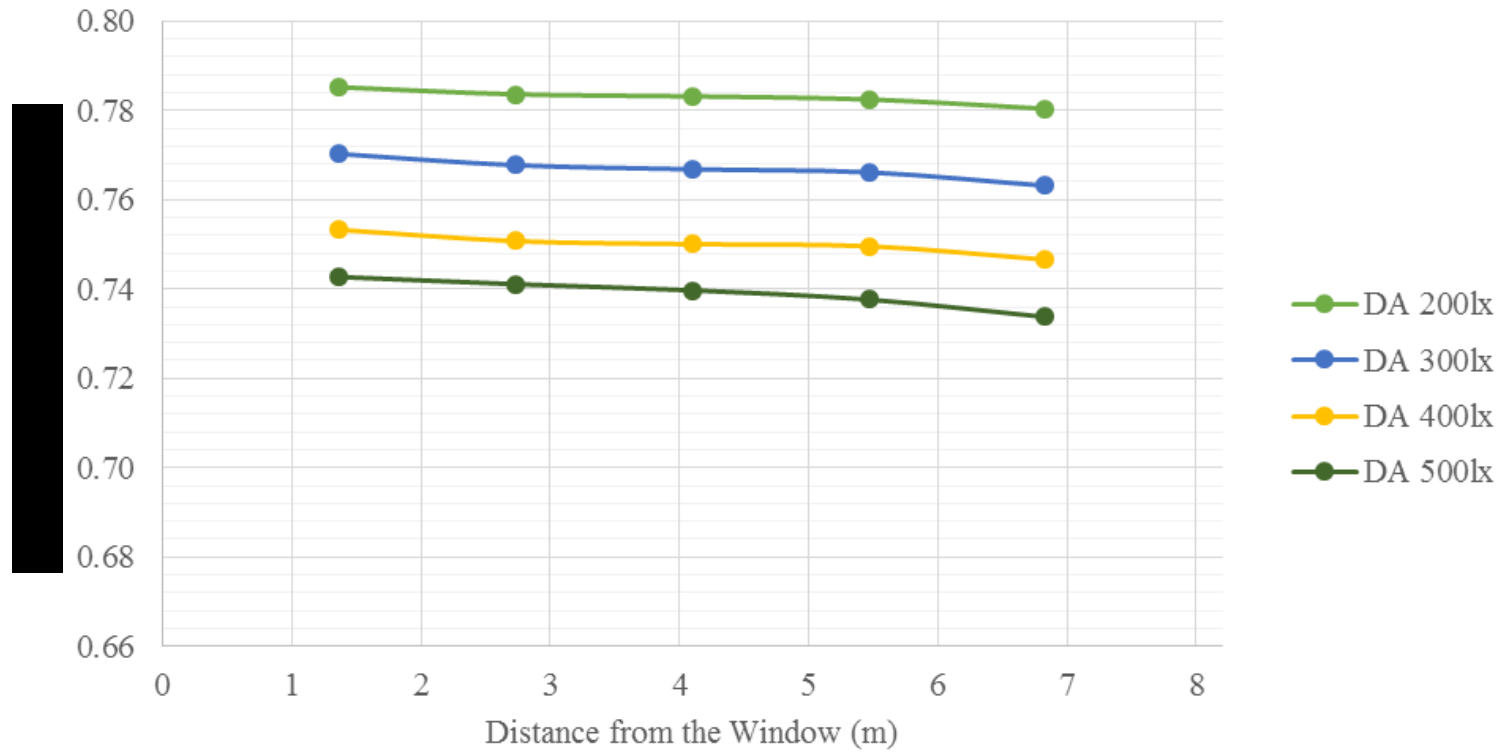


Figure 0.5: Different levels of daylight autonomy inside the room (25% shading)

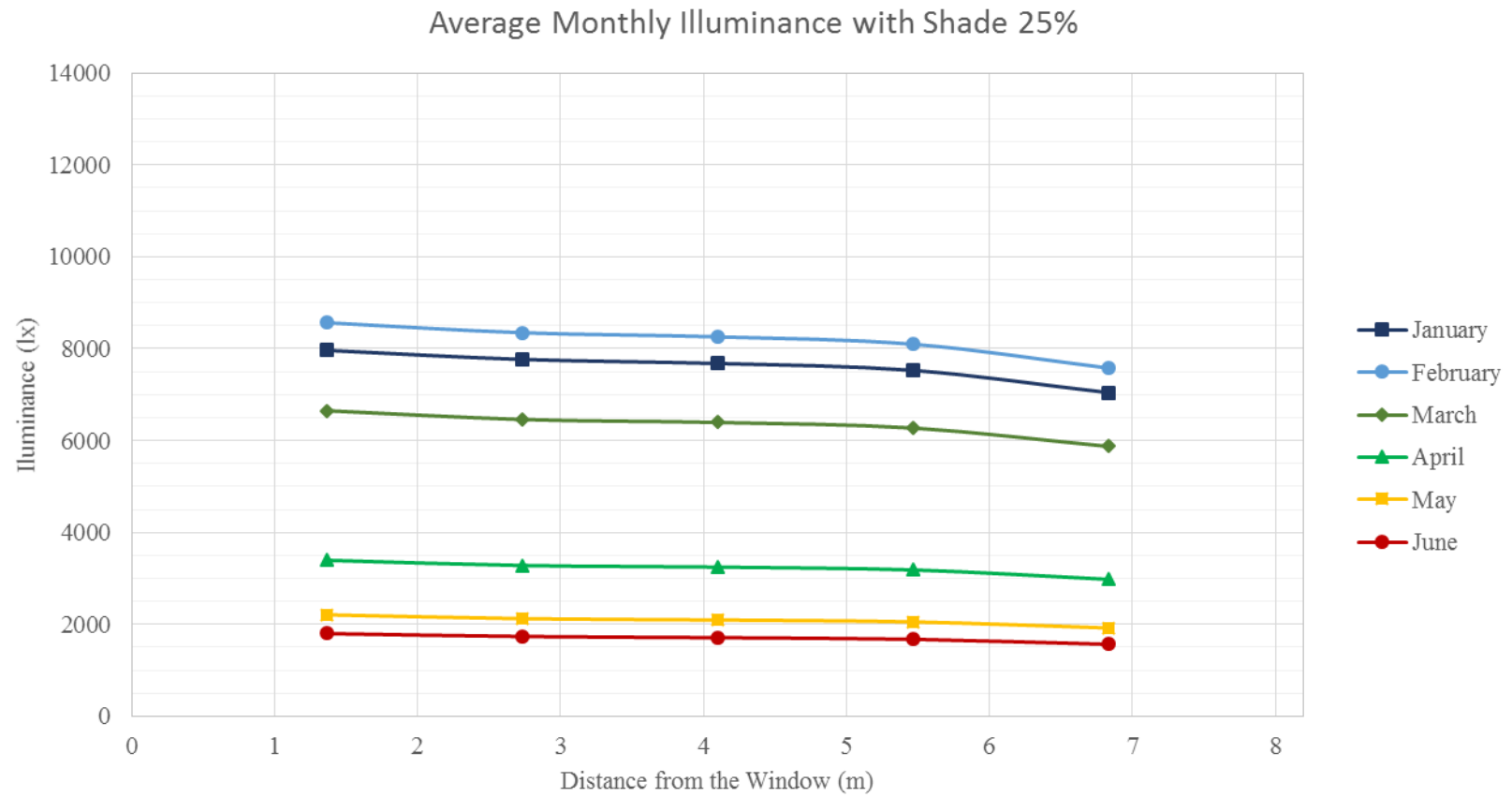


Figure 0.6: Monthly illuminance as a function of the distance from the window (25% shading)

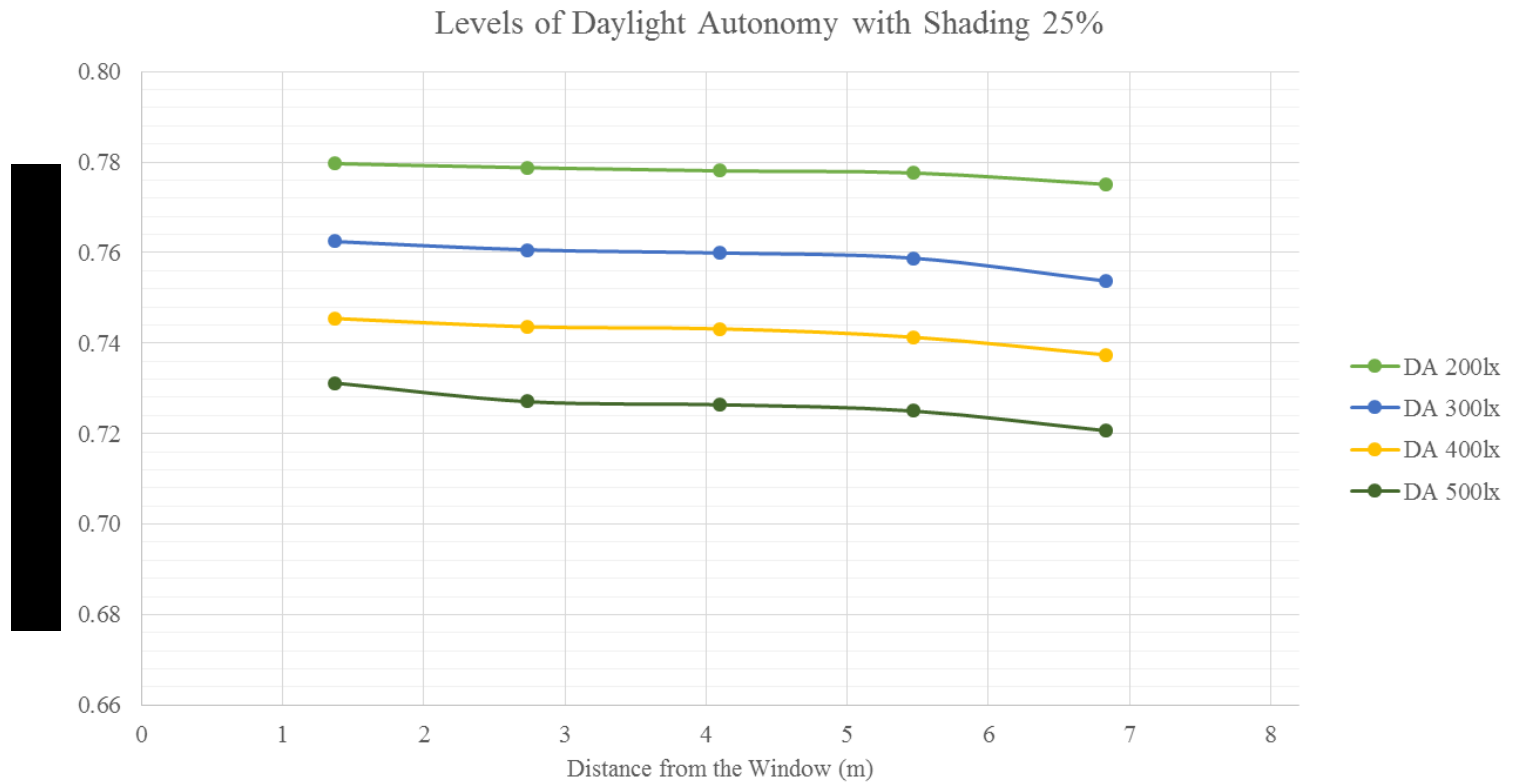


Figure 0.7: Different levels of daylight autonomy inside the room (25% shading)

Average Monthly Illuminance with Shade 50%

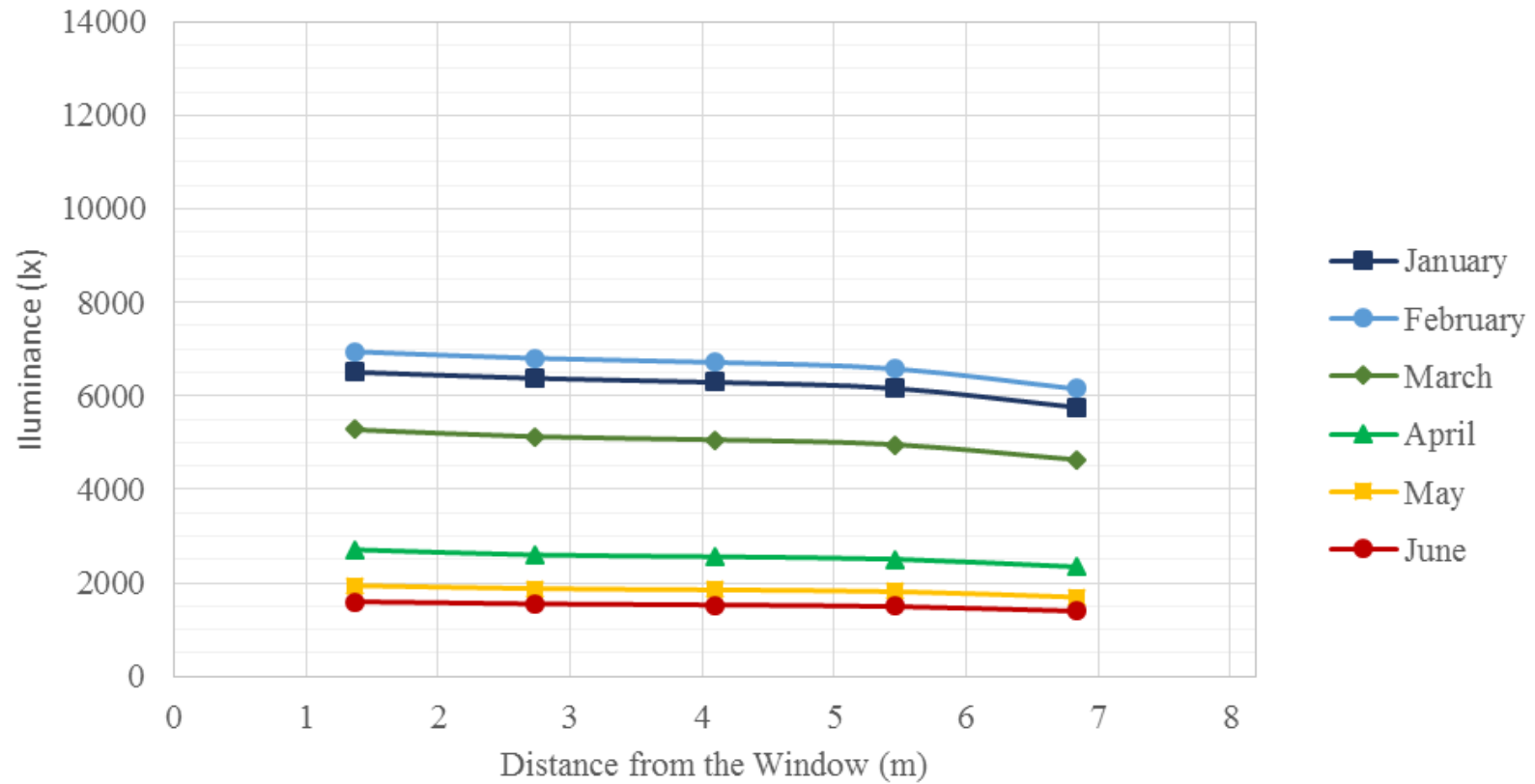


Figure 0.8: Monthly illuminance as a function of the distance from the window (50% shading)

Levels of Daylight Autonomy with Shading 50%

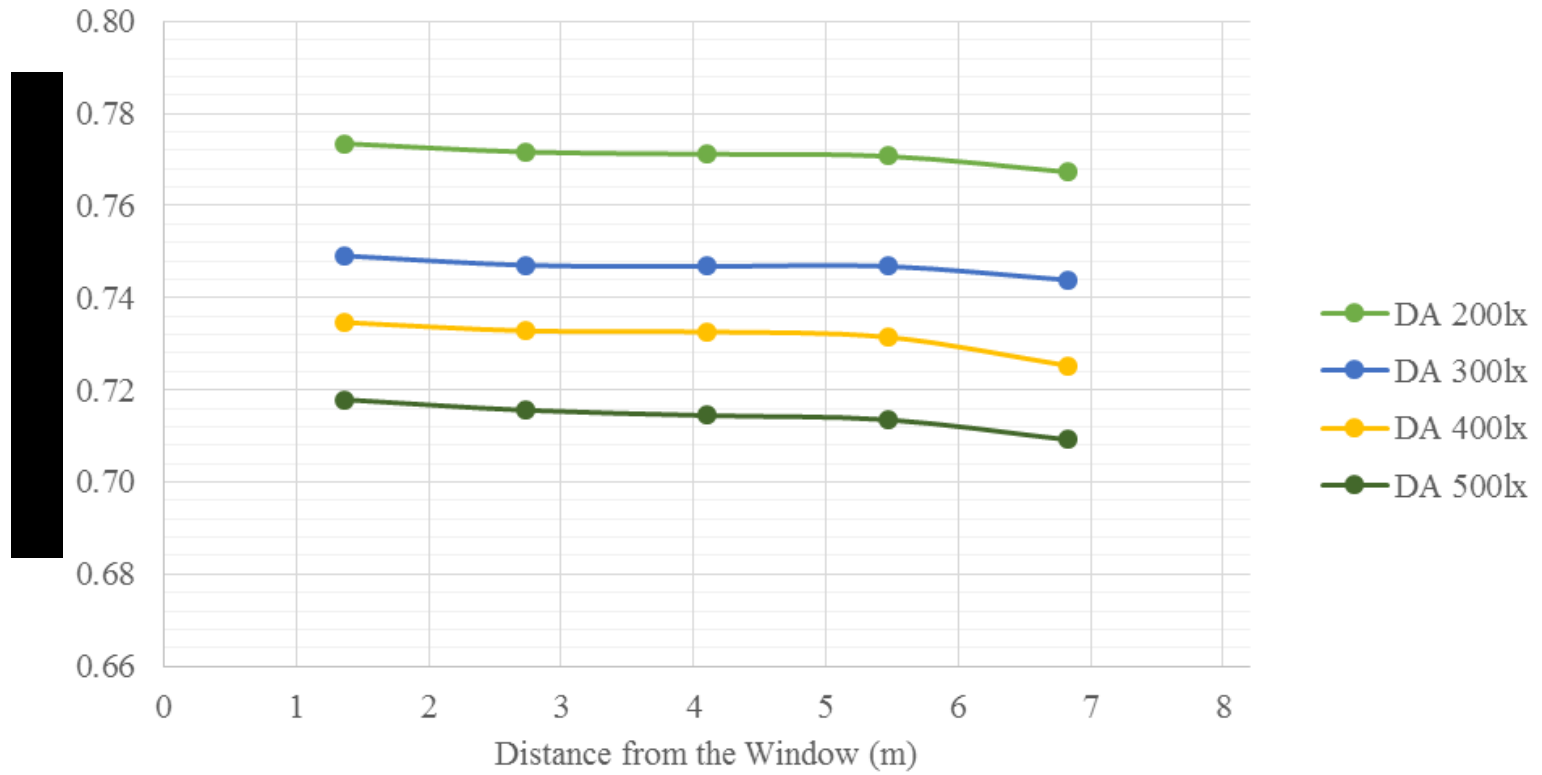


Figure 0.9: Different levels of daylight autonomy inside the room (50% shading)

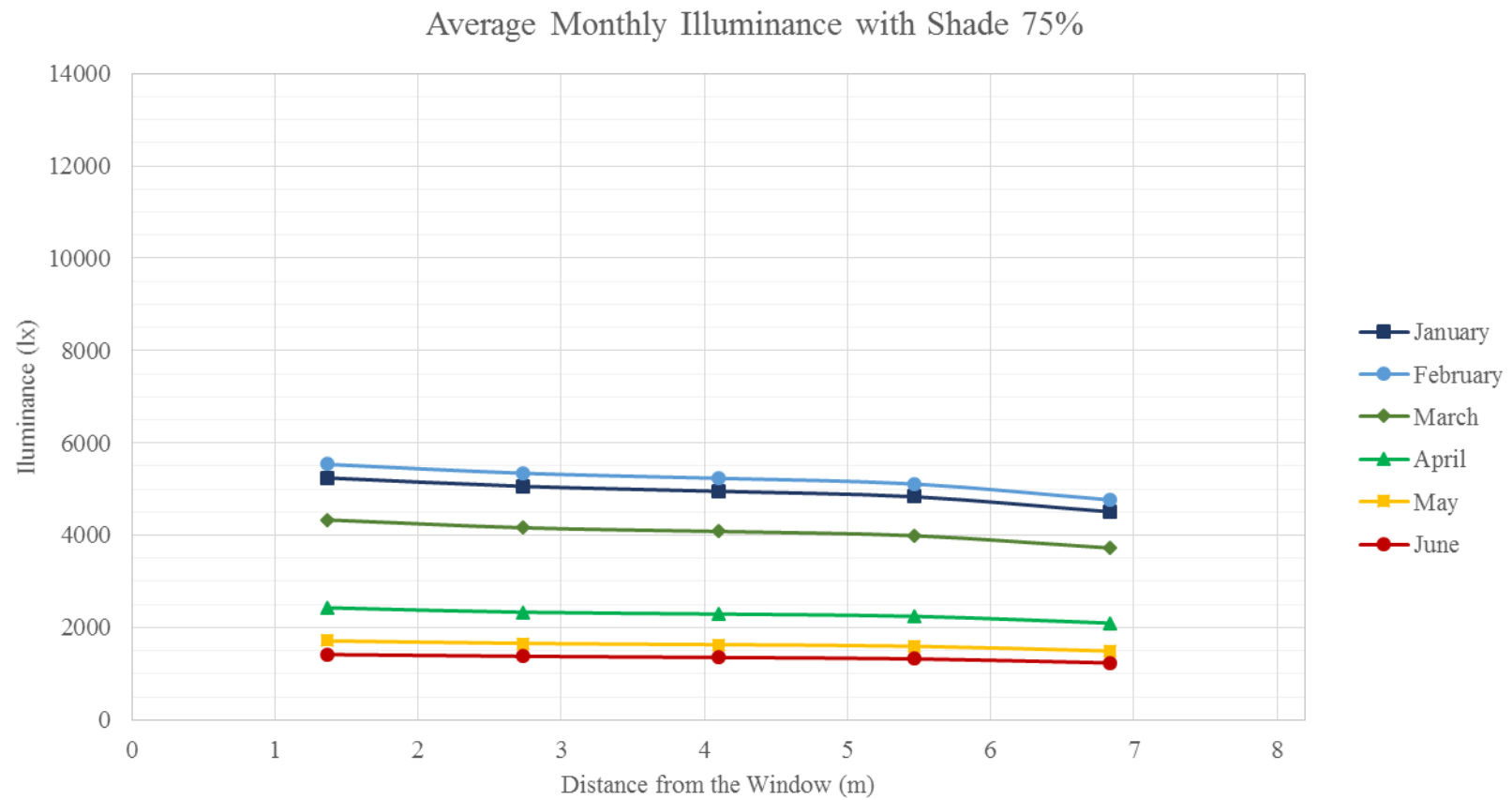


Figure 0.10: Monthly illuminance as a function of the distance from the window (75% shading)

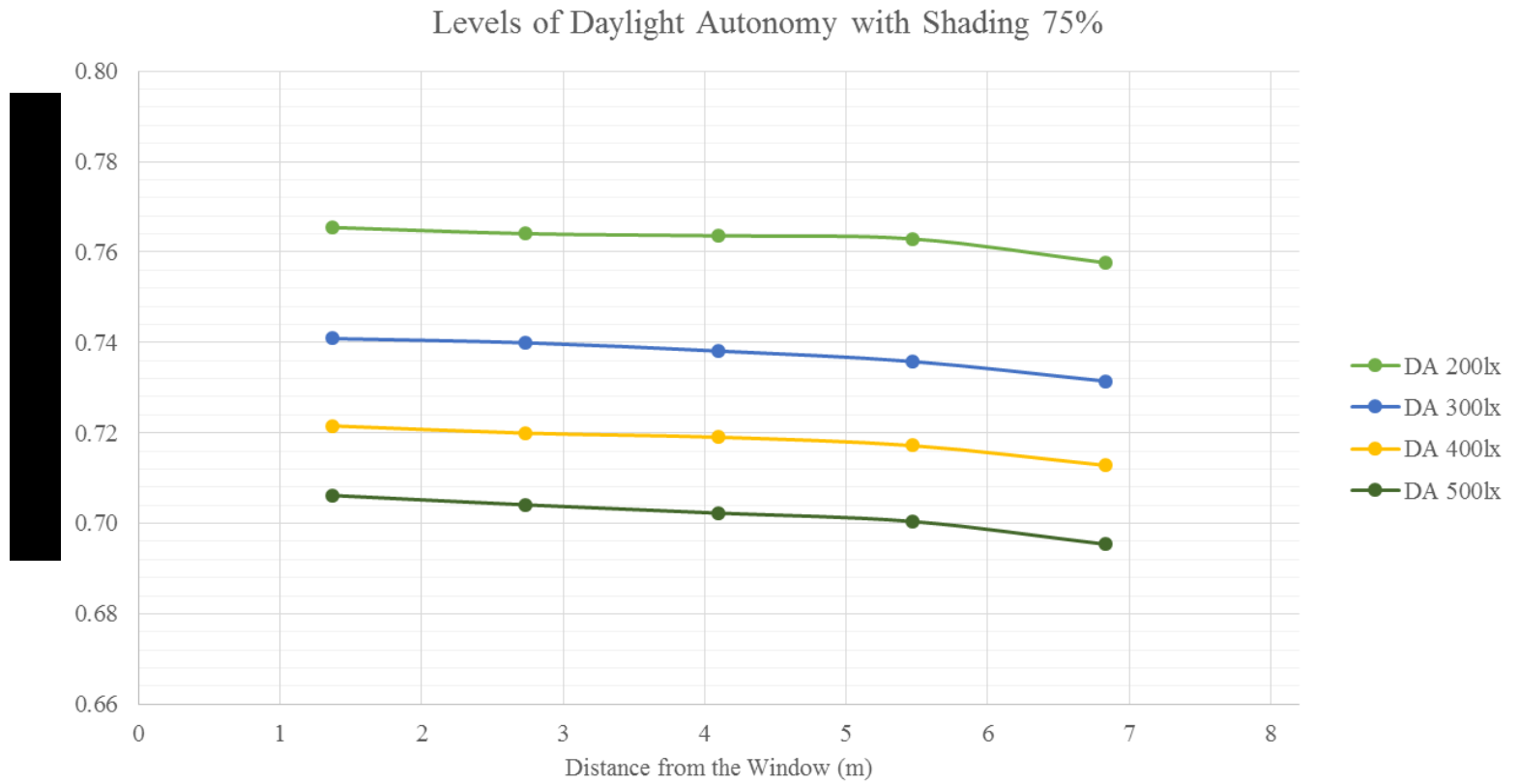


Figure 0.11: Different levels of daylight autonomy inside the room (75% shading)

Average Monthly Illuminance with Shade 100%

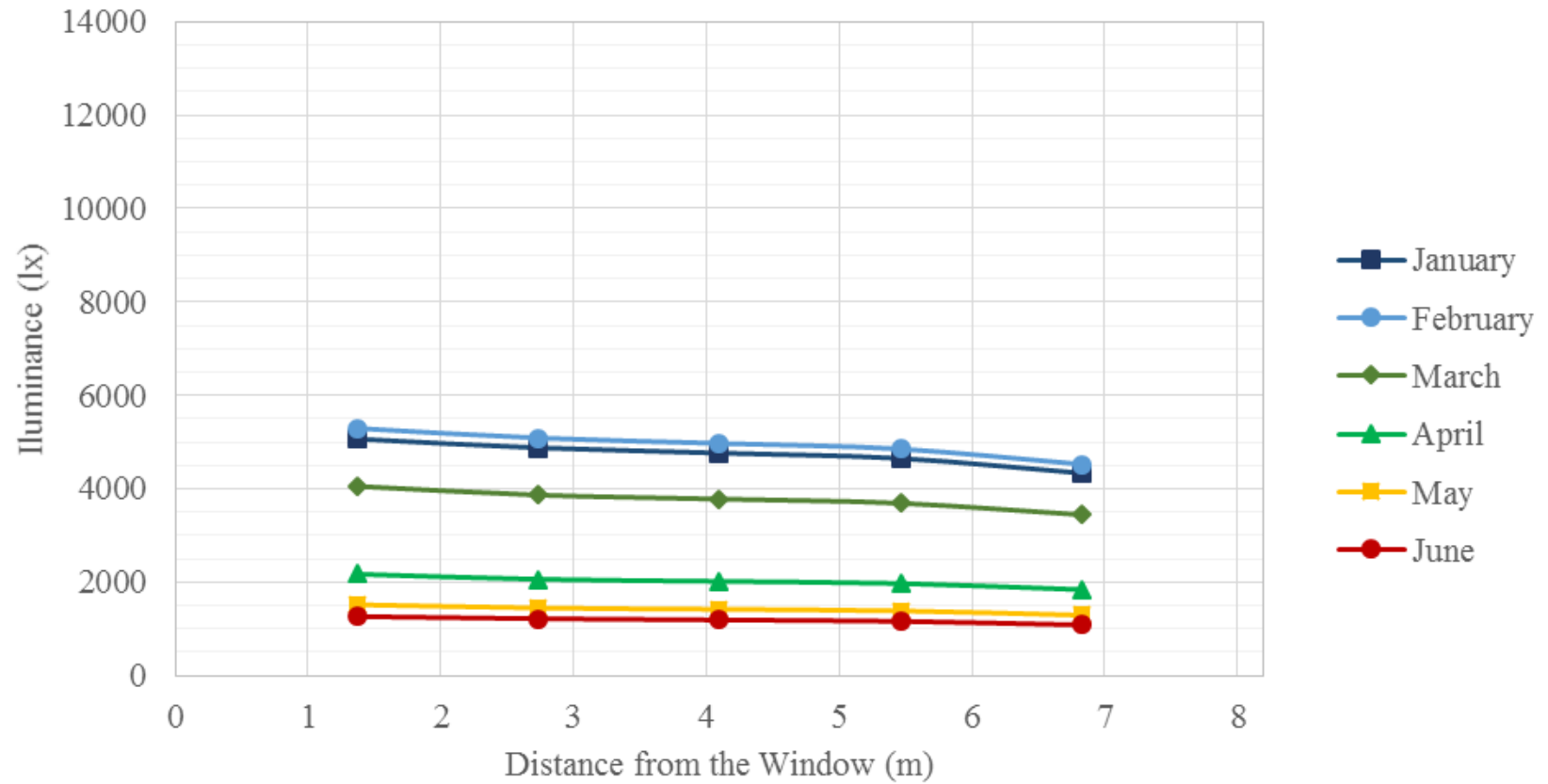


Figure 0.12: Monthly illuminance as a function of the distance from the window (100% shading)

Levels of Daylight Autonomy with Shading 100%

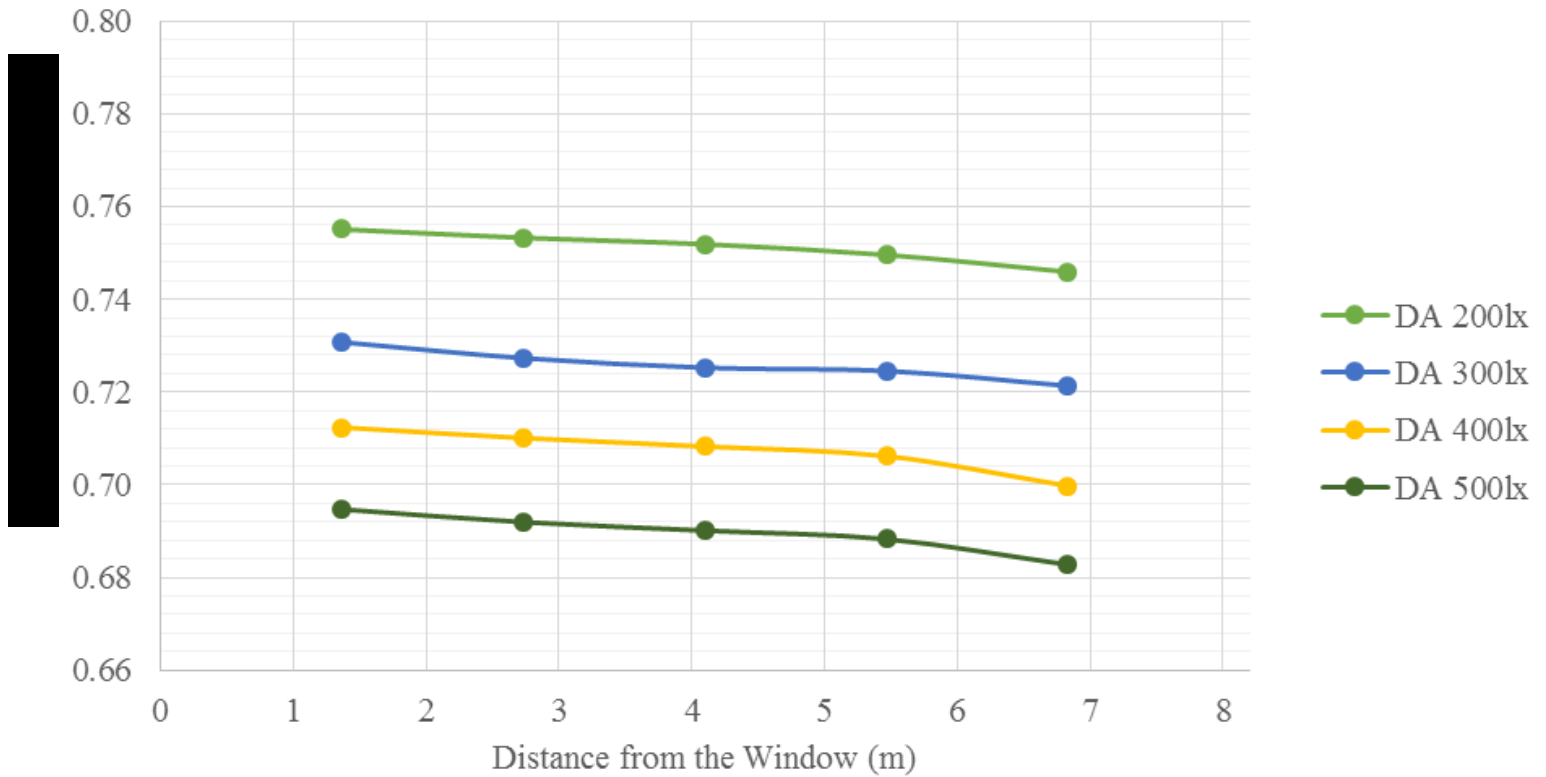


Figure 0.13: Different levels of daylight autonomy inside the room (100% shading)

Table 0.1: The View Factor matrix for the room for a case of 8 control volumes

		Wall								Floor	Ceiling	Left side	Right Side	Back wall
		1	2	3	4	5	6	7	8					
Wall	1	0	0	0	0	0	0	0	0	0.439268	0.157048	0.180651	0.180651	0.042382
	2	0	0	0	0	0	0	0	0	0.360575	0.177143	0.20953	0.20953	0.043223
	3	0	0	0	0	0	0	0	0	0.30579	0.200829	0.224793	0.224793	0.043796
	4	0	0	0	0	0	0	0	0	0.263327	0.229084	0.231751	0.231751	0.044087
	5	0	0	0	0	0	0	0	0	0.229084	0.263327	0.231751	0.231751	0.044087
	6	0	0	0	0	0	0	0	0	0.200829	0.30579	0.224793	0.224793	0.043796
	7	0	0	0	0	0	0	0	0	0.177143	0.360575	0.20953	0.20953	0.043223
	8	0	0	0	0	0	0	0	0	0.157048	0.439268	0.180651	0.180651	0.042382
Floor		0.018749	0.01539	0.013052	0.01124	0.009778	0.008572	0.007561	0.006703	0	0.378799	0.219555	0.219555	0.091045
Ceiling		0.006703	0.007561	0.008572	0.009778	0.01124	0.013052	0.01539	0.018749	0.378799	0	0.219555	0.219555	0.091045
Left side		0.009914	0.011499	0.012336	0.012718	0.012718	0.012336	0.011499	0.009914	0.282285	0.282285	0	0.249563	0.092933
Right Side		0.009914	0.011499	0.012336	0.012718	0.012718	0.012336	0.011499	0.009914	0.282285	0.282285	0.249563	0	0.092933
Back wall		0.005298	0.005403	0.005475	0.005511	0.005511	0.005475	0.005403	0.005298	0.266633	0.266633	0.211681	0.211681	0

Table 0.2: Configuration factors for the case of 5 points on the work-plane and 12 strips on the façade. 8 of the strips are above the work-plane level

	Front wall								Back wall	Right wall	Left Wall	Ceil wall
	1	2	3	4	5	6	7	8				
Point 1	0.00636	0.01743	0.02457	0.02745	0.02713	0.02497	0.02204	0.019	0.00558	0.00558	0.12531	0.57484
Point 2	0.0012	0.00351	0.00556	0.00722	0.00845	0.00923	0.00961	0.00966	0.01026	0.01026	0.14241	0.65047
Point 3	0.0004	0.00119	0.00194	0.00262	0.00321	0.00371	0.0041	0.00439	0.02156	0.02156	0.14586	0.66517
Point 4	0.00018	0.00053	0.00087	0.0012	0.0015	0.00177	0.00201	0.00221	0.05444	0.05444	0.14241	0.65047
Point 5	9.34E-05	0.00028	0.00046	0.00064	0.0008	0.00096	0.00111	0.00124	0.16896	0.16896	0.12531	0.57484

Appendix F: Electricity consumption for the heating and cooling

Electricity consumption for the heating and cooling for different shading configurations are presented for different floors and for different shading configurations.

Table 0.1: Electricity consumption for the heating of the adjacent zone for every floor

	Heating kWh/year			Heating kWh/m ² /year		
	1st	2nd	3rd	1st	2nd	3rd
V=0.5m/s 0%shading	347.08	344.40	341.64	11.76	11.67	11.57
V=0.5m/s 100%shading	360.91	358.46	355.87	12.23	12.14	12.06
V=1.0m/s 0%shading	352.43	351.04	349.42	11.94	11.89	11.84
V=1.0m/s 100%shading	365.96	364.70	363.21	12.40	12.35	12.30
V=1.5m/s 0%shading	354.36	353.46	352.37	12.00	11.97	11.94
V=1.5m/s 1%shading	367.77	366.96	365.91	12.46	12.43	12.40

Table 0.2: Electricity consumption for the cooling of the adjacent zone for every floor

	Cooling kWh/year			Cooling kWh/m ² /year		
	1st	2nd	3rd	1st	2nd	3rd
V=0.5m/s 0%shading	94.06	95.22	96.21	3.19	3.23	3.26
V=0.5m/s 100%shading	90.49	91.48	92.29	3.07	3.10	3.13
V=1.0m/s 0%shading	92.88	93.50	94.03	3.15	3.17	3.19
V=1.0m/s 100%shading	89.63	90.16	90.60	3.04	3.05	3.07
V=1.5m/s 0%shading	92.45	92.87	93.21	3.13	3.15	3.16
V=1.5m/s 1%shading	89.33	89.69	89.98	3.03	3.04	3.05

Table 0.3: Electricity consumption for the heating of the adjacent zone per month

	Heating kWh/month						Heating kWh/m ² /month					
	October	November	December	January	February	March	October	November	December	January	February	March
V=0.5m/s 0%shading	5.35	22.47	73.42	109.96	85.62	35.85	0.18	0.76	2.49	3.72	2.90	1.21
V=0.5m/s 100%shading	5.45	23.05	75.52	113.55	90.44	38.58	0.18	0.78	2.56	3.85	3.06	1.31
V=1.0m/s 0%shading	5.53	22.96	74.52	111.54	87.34	36.95	0.19	0.78	2.52	3.78	2.96	1.25
V=1.0m/s 100%shading	5.63	23.55	76.58	115.02	91.99	39.60	0.19	0.80	2.59	3.90	3.12	1.34
V=1.5m/s 0%shading	5.59	23.14	74.90	112.12	87.97	37.36	0.19	0.78	2.54	3.80	2.98	1.27
V=1.5m/s 1%shading	5.70	23.73	76.96	115.56	92.56	39.97	0.19	0.80	2.61	3.91	3.14	1.35

Table 0.4: Electricity consumption for the cooling of the adjacent zone per month

	Cooling kWh/month						Cooling kWh/m ² /month					
	April	May	June	July	August	September	April	May	June	July	August	September
V=0.5m/s 0%shading	3.64	10.70	16.90	22.81	20.35	12.47	0.12	0.36	0.57	0.77	0.69	0.42
V=0.5m/s 100%shading	3.25	10.42	16.70	22.52	19.86	11.68	0.11	0.35	0.57	0.76	0.67	0.40
V=1.0m/s 0%shading	3.45	10.49	16.70	22.60	20.11	12.20	0.12	0.36	0.57	0.77	0.68	0.41
V=1.0m/s 100%shading	3.10	10.25	16.52	22.35	19.68	11.48	0.11	0.35	0.56	0.76	0.67	0.39
V=1.5m/s 0%shading	3.38	10.41	16.61	22.52	20.03	12.10	0.11	0.35	0.56	0.76	0.68	0.41
V=1.5m/s 1%shading	3.05	10.19	16.47	22.29	19.62	11.41	0.10	0.35	0.56	0.76	0.66	0.39

Table 0.5: Difference between the electricity consumed for the heating of the adjacent zone for the different cases examined (%)

Differences between:	October	November	December	January	February	March
100% and 0% for 0.5m/s	1.96	2.57	2.85	3.26	5.62	7.61
100% and 0% for 1.5m/s	1.89	2.54	2.74	3.07	5.21	6.99
1.5m/s and 0.5m/s for 0%	4.61	2.98	2.02	1.97	2.75	4.22
1.5m/s and 0.5m/s for 100%	4.54	2.95	1.91	1.78	2.35	3.62

Differences between:	April	May	June	July	August	September
100% and 0% for 0.5m/s	-10.66	-2.61	-1.17	-1.25	-2.38	-6.34
100% and 0% for 1.5m/s	-9.73	-2.15	-0.88	-1.01	-2.05	-5.71
1.5m/s and 0.5m/s for 0%	-7.15	-2.69	-1.66	-1.28	-1.59	-2.92
1.5m/s and 0.5m/s for 100%	-6.19	-2.23	-1.38	-1.04	-1.25	-2.26

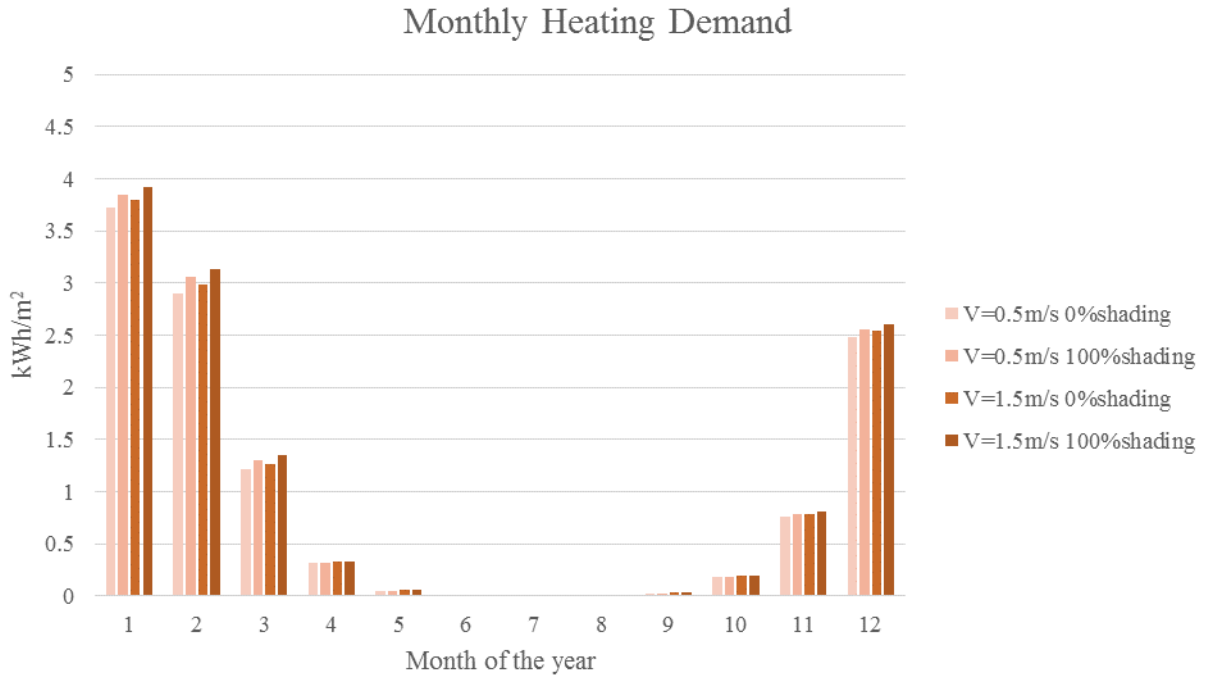


Figure 0.1: Heating demand per month for different velocities and shading configurations

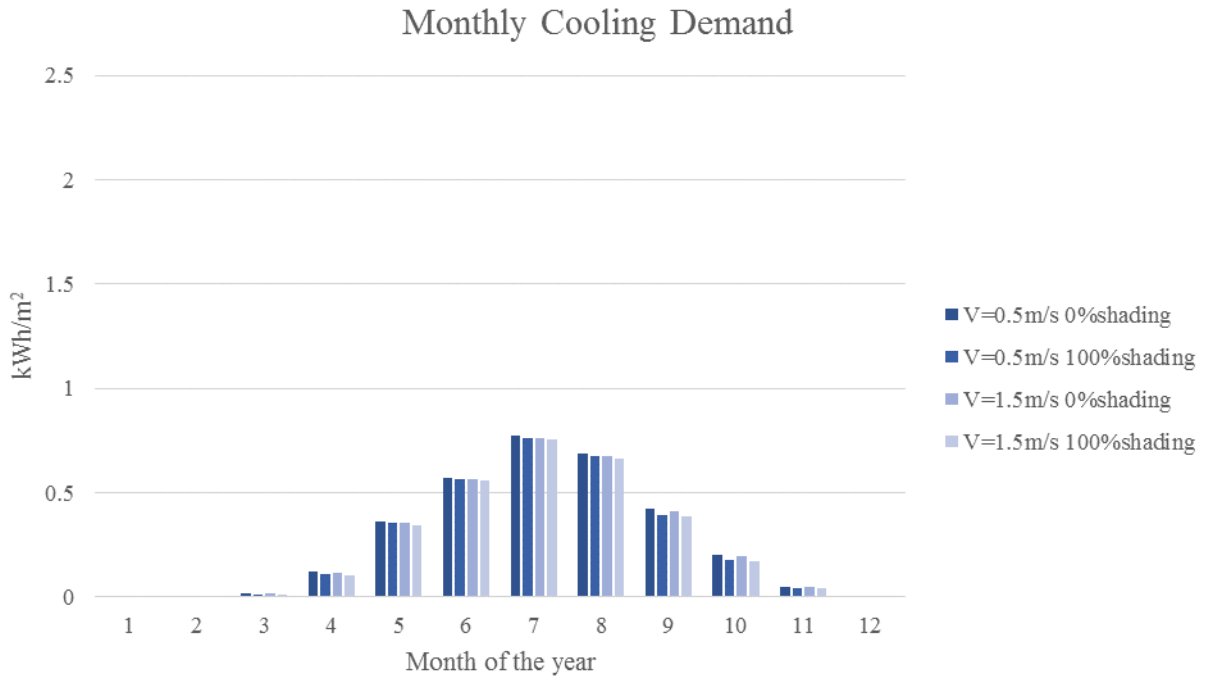


Figure 0.2: Heating demand per month for different velocities and shading configurations